STRUCTURE-PROCESSING-PROPERTY RELATIONSHIPS AND THERMOELECTRICITY IN STRONGLY CORRELATED $\mathrm{CePd_3}$ AND RELATED COMPOUNDS

By

Stephen Richard Boona

A DISSERTATION

Submitted to
Michigan State University
in partial fulfillment of the requirements
for the degree of

Materials Science and Engineering – Doctor of Philosophy

2013

ABSTRACT

STRUCTURE-PROCESSING-PROPERTY RELATIONSHIPS AND THERMOELECTRICITY IN STRONGLY CORRELATED $\mathrm{CePd_3}$ AND RELATED COMPOUNDS

By

Stephen Richard Boona

The discovery of high performance thermoelectric materials would enable the development of a wide range of new thermal and electrical energy management technologies, including the possibility of solid state cryogenic coolers. Such discoveries have been sharply inhibited to date, however, by the contraindicated nature of the material properties that comprise the thermoelectric figure of merit ZT. Enhancement of ZT generally requires overcoming significant materials science and engineering challenges that become even more restrictive at low temperatures. One possible approach for overcoming these challenges is to shift away from conventional semiconductors and toward strongly correlated electron materials, as these systems often display unusual combinations of electronic and thermal properties that may be exploited to achieve high ZT in the cryogenic temperature regime.

This perspective has motivated the current work, in which the thermoelectric properties of strongly correlated $\mathrm{CePd_3}$ and related compounds are explored. This work presents a comprehensive and systematic study of the ways in which composition and processing modifications affect the electronic, thermal, magnetic, and structural properties of these materials. The insights gained from this study have led to the highest ZT value reported to date of all p-type bulk polycrystalline materials at low temperatures. A detailed review of these developments is provided along with a discussion of how they may be applied to achieve further enhancements in ZT.

I dedicate this work to my friends and family who have provided me with invaluable guidance and inspiration in all areas of my life. I am extremely grateful to those who have sacrificed their time, energy, and resources to support me intellectually, emotionally, and financially over the last nine years as I have navigated the winding road of my higher education.

Especially, to Dad – who told me many years ago that the grand challenge of my generation would be finding new ways to produce and use energy. I took those words to heart.

ACKNOWLEDGMENTS

I would like to thank the current and former members of Professor Morelli's group who have directly or indirectly contributed to this work, including Dr. Vijay Ponnabalam, Dr. Kevin Zhou, Dr. Eric Skoug, Dr. Chang Liu, Hui Sun, Gloria Lehr, Winston Carr, and Minyoung Jeong. I would especially like to thank Xu Lu for his enthusiastic assistance with SEM/EDS experiments, as well as Dr. Reza Loloee, Travis Thompson, Karl Dersch, and the many other students and staff at MSU who have helped in various ways with this project.

I am also indebted to my former colleagues and professors in the Physics Department at Northern Illinois University, especially my master's thesis advisor Professor Bogdan Dabrowski. The strong foundation with which they provided me in the theory and practice of solid state physics has been essential in the derivation of these results.

I would also like to thank some of the many professors and mentors I have had at MSU who have contributed to my development as a scientist, especially my Guidance Committee members Dr. Jeff Sakamoto, Dr. Martin Crimp, and Dr. Viktor Poltavets.

I am of course also grateful to Professor Morelli for his invaluable guidance throughout my doctoral work, especially his encouragement to pursue my research down whatever path it may lead; the countless hours spent sharing with me his many stories, insights, and wisdom; the several opportunities he has provided me with to publish and present my results; and his expert advice on how to aim for and hit my goals that only a true bocce ball champion can provide.

Finally, I would like to acknowledge that the funding for this research was provided by the U.S. Air Force Office of Scientific Research as part of the Multidisciplinary University Research Initiative for Cryogenic Peltier Cooling, contract number FA9550-10-1-0533.

TABLE OF CONTENTS

LIST OF FIGURES

Chapter 1

Introduction

1.1 Thermoelectric effects

Ever since mankind's earliest use of tools, the fundamental purpose of most engineering technologies has been to facilitate the efficient, reliable, and targeted transfer of energy among its various forms. The discovery of three related thermodynamic phenomena by Thomas Seebeck in 1821 [1], Jean-Charles Peltier in 1834 [2], and William Thomson (Lord Kelvin) in 1854 [3] established the thermoelectric effect as a solid-state mechanism through which energy could be reversibly transferred between heat and electricity, thus providing mankind with yet another tool for harnessing the power of nature.

The simplest of these phenomena is the Thomson effect, wherein the coexistence of an electric current and a parallel temperature gradient in a single conducting material results in a reversible flow of heat. Thomson showed that the direction of this heat flow is dependent on the polarity of the charge carriers, thus distinguishing this effect from resistive Joule heating [3]. Related to this is the Seebeck effect, in which a voltage arises between the junctions of two dissimilar metals when those junctions are held at different temperatures [1]. Although Seebeck's original experiments were performed on circuits of two distinct materials, it is possible and convenient to describe the Seebeck coefficient, or thermopower, of a single material. This quantity is defined as the thermally induced voltage per unit temperature that arises within a material when subjected to a thermal gradient. Conversely, the Peltier effect describes how the insertion of a current source into a circuit composed of two distinct metals will result in a net absorption or liberation of thermal energy at the metal junctions. This occurs due to differences in the amount of heat transported by the charge carriers in the two materials; in order to maintain a constant flow of current in accordance with Kirchoff's Law, a net transfer of heat with the local environment at the junction must occur for the charges to flow smoothly and continuously from one material to the other [2].

These effects can be utilized for a variety of power generation and temperature control applications. This requires the combination of at least two types of materials: one where the dominant charge carriers are electrons (n-type) and one where they are holes (p-type). Thermoelectric devices can be built from alternating legs of these materials connected electrically in series and thermally in parallel. Applying a temperature gradient across the legs of such a device results in an open circuit potential that can be utilized as a power source. In principle, this can be done actively or passively to generate electrical energy from the temperature gradient created by any primary heat source. Conversely, connecting a similar thermoelectric module to a power supply allows for precise temperature control of the hot and/or cold sides of the module by controlling the direction and magnitude of the current supplied to the device [4].

1.2 Applications of thermoelectric devices

The two most common uses of thermoelectric devices are for power generation via thermoelectric generators and temperature control via Peltier coolers.

The appeal of using thermoelectric devices for power generation lies in their versatility and reliability, both of which stem from the solid-state nature of the thermoelectric effect.

These devices can be tailored for use within a wide range of geometries and length scales, and their lack of moving parts largely eliminates any design problems related to vibrations, maintenance, and mechanical failure. These positive aspects are generally negated by the relatively poor thermal-to-electrical energy conversion efficiency of most thermoelectric materials, thus limiting the use of these devices to niche applications such as power generation on NASA deep space probes and planetary science missions. These limited applications have nonetheless served as excellent demonstrations of the strong potential this technology holds for more widespread use, as indicated by the uninterrupted operation of these thermoelectric generators over multiple decades in the vacuum of space [5].

Many potential terrestrial applications also exist if materials and devices can be engineered to match the cost, reliability, and performance metrics required for deployment in commercial, industrial, and military arenas. Among these possible uses are waste heat recovery from automobiles and power plants as well as improved home energy efficiency and remote power generation for recreational and survival situations. [6, 7, 8, 9]

Thermoelectric devices for temperature control are already a relatively common application of the thermoelectric effect. This can be seen in a variety of products, including localized heaters and coolers in automobile seats and cup holders, thermoelectric "refrigerators" operating on low voltages and/or offering precise temperature control of wine and other consumer goods, and coolers designed for delicate electronic equipment such as observational telescope cameras and other types of sensors. Although these thermoelectric modules are not generally useful for applications requiring high power cooling, their flexible form factors, precision control, and lack of moving or vibrating components again offer important advantages over alternative technologies such as vapor compression. [7, 8, 9]

One particularly appealing potential arena for applying the thermoelectric effect is in the cryogenic temperature regime, wherein a number of possible uses exist for cooling various types of electronic and laboratory equipment in conjunction with traditional vapor compression systems and/or as standalone devices. The reliable and solid-state nature of thermoelectric technology once more makes these devices attractive candidates for applications such as cooling superconducting transmission cables, precision temperature control of laboratory characterization equipment, and thermal noise reduction in space-based infrared and gamma ray detectors.

Before any of these uses can be realized, however, significant improvements are necessary in the properties of the available materials. This is especially true at low temperatures, where a dearth of useful compounds has forced cryogenic thermoelectric cooling to remain a purely theoretical application. This has largely motivated the current work, which focuses on the exploration of new approaches for developing high performance thermoelectric materials in this temperature range. To properly consider these new approaches, it is useful to first establish a suitable context for the origins of favorable thermoelectric performance.

1.3 Thermoelectric performance

The thermoelectric performance of any material can be quantified through the dimensionless figure of merit ZT, which is defined as

$$ZT = \frac{\alpha^2 T}{\rho\kappa} = \frac{\sigma\alpha^2 T}{\kappa}, \tag{1.1}$$

where α is the Seebeck coefficient, ρ (σ) is the electrical resistivity (conductivity), κ is the total thermal conductivity, and T is the average absolute temperature [10].

ZT values for state-of-the-art bulk materials are on the order of unity. Values as high as two have been reported in PbTe-based compounds at temperatures near 900 K [11]. Below room temperature, however, the maximum values reported generally remain well below unity for both n-type and p-type materials. The minimum ZT necessary for a thermoelectric cooler to operate will vary with the absolute temperature of the device as well as the temperature gradient across it, but ZT values of at least 0.3 or larger are generally necessary for such a device to establish a useful temperature gradient [4].

The essential challenge in developing high ZT materials at any temperature stems from the competing nature of the relevant material properties. Since the Seebeck coefficient is a measure of the charge separation that occurs when a material is exposed to a temperature gradient, this charge separation will generally be smaller in materials within which charge flows easily. Thus as ρ decreases, α tends to decrease as well. Similarly, modifying a material to lower its thermal conductivity is also likely to affect the electrical conductivity, since the mechanisms useful for impeding heat flow also tend to affect charge flow as well.

The path to increasing ZT therefore lies in finding ways of decoupling and separately optimizing these properties. The most direct way to accomplish this is by considering that the total thermal conductivity of most materials is comprised of two main contributions, the first from quantized vibrations of the atomic lattice known as phonons (κ_l), and the second from the polar thermal diffusion of charge carriers (κ_e). Since the lattice contribution to the thermal conductivity in most semiconductors tends to be orders of magnitude larger than the electronic contribution, this has led to a common paradigm in thermoelectricity over the last several decades wherein the numerator of ZT is considered entirely dependent on a given material's electronic properties, while the denominator is a function of only the lattice thermal conductivity. This interpretation of the ZT equation allows for a relatively straightforward description of the transport properties, and intuitively leads into the conclusion of Slack that an ideal thermoelectric material should behave as a “phonon-glass, electron-crystal” (PGEC); that is, the heat conduction should be minimal and similar to that of an amorphous solid, while the electronic properties should mimic those of a highly ordered crystalline material [12]. It is from this perspective that a basic understanding of thermoelectric optimization strategies can be developed.

1.4 ZT optimization strategies

Although practical limitations have been asserted for the maximum ZT of a semiconductor based on realistic values of the relevant properties, there is no theoretical upper limit on the maximum possible ZT of a material in general [13]. In order to explore the ways through which increases in ZT can be achieved, particularly at low temperatures, it is useful to consider the current paradigm of semiconductor-like materials that has largely governed the field of thermoelectricity since its inception. Critical evaluation of this paradigm shows that although it is not generally a useful approach for achieving high ZT at cryogenic temperatures, it can still nonetheless be utilized as a basis for developing a more suitable perspective.

1.4.1 Semiconductors and the PGEC paradigm

Seebeck’s original experiments on elemental and binary p-block semiconductors laid the initial framework for the field of thermoelectricity. This has traditionally led to a strong emphasis on various chalcogenide compounds [1]. Seebeck’s work has been expanded upon over the last century through notable contributions from many different researchers, including Eucken's early studies of thermal conductivity in alloys and compounds [14], Ioffe's development of the ZT equation and work on heavily doped semiconductors [15], Goldsmid's detailed analysis of desirable electronic band structure properties and invention of functional thermoelectric coolers [16], Slack's development of the minimum lattice thermal conductivity and PGEC concepts [12], and several others. These contributions have led to significant advances in the fields of solid state physics and materials science at large.

1.4.1.1 Thermal properties

Thermal conductivity is a complex transport phenomenon that arises from the interaction of many different processes inside of a material. The electronic and lattice contributions to the thermal conductivity of a solid are nominally linearly independent of each other. The electronic contribution can be estimated through the Wiedemann-Franz (W-F) law [17], which is defined as

$$\kappa_e = \frac{TL}{\rho} = \sigma TL, \tag{1.2}$$

where L is a material property known as the Lorenz number. The Lorenz number can be calculated from first principles for a Fermi gas, and the result of this calculation is commonly known as the Sommerfeld value L_0, which is given by

$$L_0 = \frac{\pi}{3}\left(\frac{k_B}{e}\right)^2 = 2.44x10^{-8}\ \Omega m K^{-2}, \tag{1.3}$$

where k_B is the Boltzmann constant and e is the elementary charge.

The primary assumption in the derivation of W-F is that the electron mean free path is the same under an electric field as it is under a temperature gradient, i.e. that inelastic electron-phonon scattering events are rare. This assumption is generally reasonable, particularly for conventional metals, and strong empirical support for this relationship can be found in experiments that show $L \approx L_0$ for many different types materials over a broad range of temperatures [18]. The Sommerfeld value can therefore be applied to provide at least an estimate of the electronic thermal conductivity of any material, in turn enabling a reasonably accurate and self-consistent determination of the lattice contribution as well.

The magnitude and temperature dependence of a material's lattice thermal conductivity are both functions of mostly physical parameters such as temperature, density, stiffness, structure type, strain, defects, and other properties of the crystal lattice. These parameters are nominally independent of a material's electronic properties, although the nature of the chemical bonds can be important for both, and direct electron-phonon scattering as well as electron-phonon coupling (so-called "phonon drag") can occur. In addition to these phenomena, the electronic and thermal properties are often indirectly related through a shared dependence on various scattering mechanisms that affect both the phonon and electron mean free paths, such as impurities and interfaces [18].

A simple quantitative model of lattice thermal conductivity can be described by

$$\kappa_l = \frac{1}{3} C_v v l, \tag{1.4}$$

where C_v is the lattice heat capacity, v is the phonon group velocity, and l is the phonon mean free path [19]. The minimum possible thermal conductivity of a material corresponds with the so-called "amorphous limit" where the average distance between phonon scattering events is on the order of the interatomic spacing. This minimum value can be estimated from Equation 1.4 by measuring C_v, setting the mean free path l equal to the average interatomic spacing, and solving for the speed of sound $v = \sqrt{\Lambda/\delta}$, where Λ is the elastic modulus and δ

is the density. For typical crystalline materials, this minimum lattice thermal conductivity is on the order of 0.1 W/m-K [12].

A more complete version of this analysis can be performed by incorporating the dependence of these parameters on the frequency of the atomic vibration modes. This is particularly important below a material's Debye temperature Θ_D, where not all of the possible phonon modes are active. The Debye-Callaway model provides the necessary framework for this. Ignoring the small correction that arises for non-resistive phonon-phonon interactions, this model is described by the integral

$$\kappa_l = \frac{1}{3}\int_0^{\omega_0} C(\omega)v(\omega)^2\tau(\omega)d\omega, \tag{1.5}$$

where $\tau = l/v$ is the frequency-dependent relaxation time between phonon scattering events and ω_0 is the frequency of the highest active phonon mode [18]. Based on this equation, the basic and obvious strategy that emerges for achieving low lattice thermal conductivity is to engineer materials such that they have low lattice heat capacity, low sound velocity, and/or a short phonon scattering relaxation time. The complexity of the factors that contribute to these properties, particularly their dependence on phonon frequency and temperature, makes it difficult to predict *a priori* the exact ways in which changes in composition and processing will affect the absolute magnitude of a material's thermal conductivity. Several common strategies have nonetheless emerged for engineering the thermal properties of materials.

In regards to minimizing the group velocity of the phonons, for example, a common approach is to seek out dense compounds with relatively soft bonds in order to make $\sqrt{\Lambda/\delta}$ small. Another common approach is to search for materials with large primitive unit cells, as this structural complexity suppresses the group velocity of the heat-conducting acoustic modes while it simultaneously introduces a number of optical phonon modes that have small group velocities and therefore do not typically contribute to thermal conductivity [19]. The effects of large unit cells and complex structures have been credited as the source of low thermal conductivity in materials such as $Y_3Al_5O_{12}$ garnet [20], β-Boron, and YB_{68} [21]. The major drawback to these group velocity reduction approaches, however, is that they make no guarantee that the electronic properties of the material will simultaneously be within the useful range for thermoelectric applications, although they do least provide insight into what types of systems may be of interest.

A more common and more robust approach to achieving low lattice thermal conductivity is to first select materials with desirable electronic properties and then modify them through processing and composition adjustments in order to decrease the phonon mean free path l. This can be thought of qualitatively as maximizing the structural disorder of the material in order to limit the propagation of coherent lattice vibrations. There are many different ways that this can be accomplished, and although thermal resistivities are not strictly additive, the effects of multiple phonon scattering mechanisms on the relaxation time can generally be added as $\tau^{-1} = \sum \tau_i^{-1}$ [18]. This allows for the simultaneous utilization of multiple mechanisms to achieve a maximum reduction in thermal conductivity.

Effective phonon scattering mechanisms include lattice strain, atomic mass mismatches, vacancies, interstitial atoms, mobile dislocations, grain boundaries, resonant rattling modes of loosely bound filler atoms [22], and any other phenomena that increase the structural disorder of the material [18]. When considering which of these mechanisms to employ for thermal conductivity reduction in a specific compound, it is useful to consider the temperature range within which the material is being designed to operate.

At relatively high temperatures ($T > \Theta_D$), the thermal conductivity is typically dominated by inelastic phonon-phonon scattering. The heat capacity is approximately constant and equal for all materials to the Dulong-Petit value of $3R$, where R is the ideal gas constant [18]. The phonon mean free path decreases with temperature due to the increased frequency of phonon-phonon interactions, and this behavior dominates the overall temperature dependence of the thermal conductivity in this range.

At the opposite extreme of $T < \Theta_D$, not all phonon modes are active, and longer wavelength vibrations with relatively long mean free paths tend to dominate the thermal conductivity. This means that lattice vibrations will generally propagate unhindered until scattered by grain boundaries. The magnitude of Θ_D typically scales with $\sim T_m/4$, where T_m is the melting point, so no change in grain size or morphology is expected within the range of $T < \Theta_D$ [23, 24]. This implies that the phonon mean free path is constant, and therefore the overall temperature dependence of the thermal conductivity is dominated in this range by the temperature variation of the lattice heat capacity, which rises as T^3 [18]. Thus for low temperature applications, l can be effectively reduced through grain size reduction and/or the introduction of nano-scale features such as precipitates. Although this approach is still useful at higher temperature as well, it is particularly well suited for cryogenic applications due to limited concerns over nucleation and growth of the nano-scale features.

In between these two extremes, where $T \approx \Theta_D$, the two opposing trends in κ_l vs T meet and a peak is observed. It is within this range, where the phonon mean free paths are smaller than the grain size but phonon-phonon interactions are not yet dominant, that other scattering mechanisms such as point defects and solid solution mixing can be utilized to substantially suppress the thermal conductivity.

The inherent difficulty of thermal conductivity reduction within the context of thermoelectricity is finding ways of introducing structural disorder without negatively impacting the material's electronic properties. This can be extremely challenging in some instances, as electrons are also scattered by many of the same mechanisms that scatter phonons. In addition to this, the presence of vacancies, interstitial atoms, and/or substitutional atoms can be expected to alter the bonding environment and doping level of the material due to differences in electronegativity and valence configuration between these atoms and the original matrix.

One way of addressing these challenges is to seek out substitutional elements that have similar electronic properties to the element they are replacing. For example, the relaxation time for mass mismatch phonon scattering scales as $\tau \propto \left(\frac{M}{\Delta M}\right)^2$ [18], where M is the mass of the host matrix element and ΔM is the mass difference between the substitutional element and the host. It is thus often effective to substitute in an isoelectronic element that has a much different mass from the original matrix atoms in order to minimize τ. This idea has been successfully implemented to enhance the ZT of a wide range of materials [4, 19].

In spite of the varying effectiveness of these thermal conductivity reduction approaches in different temperature ranges, each can still have an important effect on the thermal conductivity at all temperatures. It is therefore useful to take a broad-based approach regardless of a material's desired temperature range of operation.

1.4.1.2 Electronic properties

A consideration of electronic band structure phenomena is necessary in order to determine the types of materials that may be of interest for thermoelectric applications, as well as how these materials may be successfully modified to improve their properties. The dependence of ZT on both the Seebeck coefficient and electrical conductivity requires a careful balance of these contraindicated properties, and such a balance can often be found in highly doped semiconductors. If the doping level is sufficiently high, the real space separation of the dopant atoms can become small enough that their electronic states overlap and form an impurity band in the density of states. This generally leads to a mixture of metallic and semiconductor-like electronic properties, and such materials are known as degenerate semiconductors. It can be shown from first principles that within the simple direct gap parabolic electronic band model, a degenerate semiconductor will have a Seebeck coefficient of the form

$$\alpha \propto m^* T(n)^{-2/3}, \tag{1.6}$$

where m^* is the carrier effective mass, T is the absolute temperature, and n is the carrier density [25]. Similarly, the electrical conductivity of such a material is of the form

$$\sigma = \frac{1}{\rho} \propto n\mu \propto \frac{n\tau}{m^*}, \tag{1.7}$$

where μ is the carrier mobility and τ is the relaxation time between charge carrier scattering events. It is convenient to combine these properties together in the way that they appear in the ZT equation, and the resulting term is known as the "power factor" $\alpha^2\sigma$. For a degenerate semiconductor, this term is of the form

$$\alpha^2\sigma \propto T^2 \left[\frac{m^{*2}\mu}{\sqrt[3]{n}}\right] = T^2 \left[\frac{m^*\tau}{\sqrt[3]{n}}\right]. \tag{1.8}$$

Writing the power factor this way makes it apparent why research into thermoelectricity has traditionally focused on the relationships among n, μ, and m^*, as the power factor can be optimized through carefully tuning these parameters. Furthermore, although n, μ, and m^* can each vary with temperature, the explicit T^2 dependence of the power factor provides some explanation for why high ZT values are more commonly observed at high temperatures. The results of these analyses show that the best thermoelectric materials tend to be degenerate semiconductors with carrier densities on the order of 10^{19} cm^{-3} [4].

Embedded within n, μ, and m^* are strong dependencies on the crystal chemistry of a given material. The carrier effective mass as well as the density and strength of charge carrier scattering mechanisms can be strongly affected by tunable parameters such as composition, electronegativity, and valence configuration [12, 25]. A rigorous analysis of these parameters through first-principles considerations allows for additional convenient combinations and descriptions of the properties of a semiconductor, from which further optimization strategies can be derived. Among these is the thermoelectric "quality factor" developed by Goldsmid [16] that emphasizes the need for high carrier mobility and effective mass in conjunction with low lattice thermal conductivity, as well as Mott's formalism describing the dependence of the Seebeck coefficient on the logarithmic derivative of the electrical conductivity [26].

It is possible through some of these more complex derivations to arrive occasionally at conclusions that provide guidance counter to that of Equation 1.8. For example, consideration of electron-phonon interactions and the corresponding deformation potential they introduce can be used to show that materials with lower carrier effective mass may in some instances actually be more likely to display high ZT [27]. Thus it is apparent that the traditional guiding principles for engineering high performance thermoelectric materials are necessarily flexible depending on the type of material and temperature range being considered. The relationship described by Equation 1.8 therefore is most useful as a basic framework for anticipating which parameters may at least be relevant when attempting to optimize the electronic properties of any material for thermoelectric applications.

The necessity of this flexibility in design principles becomes most apparent at room temperature and below, where the physics of semiconductors makes high ZT values increasingly difficult to obtain. One of the more thorough treatments of this is provided by Slack, who has proposed that ZT values as large as four may be possible at room temperature in appropriately doped narrow-gap binary semiconductors that approximate the ideal PGEC conditions [12]. The results of his derivation indicate that once a semiconductor-like material has been engineered to reach the amorphous limit of lattice thermal conductivity, ZT then depends nearly exclusively on the weighted mobility of the carriers, which is defined as $U = \mu \left(\frac{m^*}{m_o}\right)^{1.5}$, where m_o is the free electron mass.

Slack shows that this parameter must be at least 150 $\frac{cm^2}{Vs}$ in order to reach ZT values of unity at room temperature. The need for such large mobility values emphasizes why the development of high ZT p-type compounds is especially difficult, as the weighted mobility of the carriers in such systems is often much lower than this.

Slack also acknowledges that very few binary systems appear to exist that actually possess this desirable combination of electronic band structure properties, although he does suggest that some suitable ternary semiconductor systems may be found [12]. In either case, it is necessary to carefully tune the composition so as to maximize U. Since this parameter is generally affected by the same scattering mechanisms that are useful for reducing κ_l, however, the threshold of 150 $\frac{cm^2}{Vs}$ is certainly a conservative estimate of the minimum value needed.

This conclusion suggests that the conventional semiconductor paradigm may be prohibitively narrow in its description of the relevant electronic properties at cryogenic temperatures. It is therefore worth considering alternative perspectives to determine if one of these may be more suitable for developing high ZT materials within this temperature range.

1.4.2 Need for an alternative approach

The limited usefulness of semiconductors for low temperature thermoelectric applications suggests that a broader perspective may be necessary if materials with sufficiently high ZT values are to be developed. It is therefore useful to reconsider the basic form of the ZT equation in order to more generally evaluate what material systems may be appropriate.

1.4.2.1 The case for metals

This analysis begins by inserting the W-F law of Equation 1.2 into the original form of ZT in Equation 1.1. After making the standard assumption that only the electronic and lattice contributions to the thermal conductivity are significant, it is possible to express ZT as

$$ZT = \frac{\alpha^2}{L(1+\kappa')}, \tag{1.9}$$

where $\kappa' = \kappa_l/\kappa_e$ is the ratio of the lattice and electronic thermal conductivities [4]. Writing ZT in this way parameterizes the thermoelectric efficiency of all material at all temperature into a function of only two variables, α and κ'. The relative uniformity of L among a wide variety of bulk materials establishes the basic criteria that high ZT values of unity or larger will only be observed in materials with Seebeck coefficients on the order of 150 μV/K or larger, regardless of the magnitude of κ'.

In the limiting case of $\kappa' >> 1$, which generally applies for semiconductor materials, it is convenient to use the conventional optimization strategy discussed above. That is, κ_e can be ignored and ZT can be expressed as $ZT \approx T(\alpha^2\sigma)/\kappa_l$. The optimization of ZT then focuses on finding materials with low lattice thermal conductivity and large power factors. The basic problem with semiconductors at low temperatures is that the electrical conductivity (and therefore the power factor) tends to become prohibitively small as T decreases. This trend, combined with the existence of a minimum possible value for the lattice thermal conductivity, makes large ZT very difficult to obtain using this approach.

Alternatively, the form of Equation 1.9 suggests that high ZT can also be found in materials with small κ'. In the limiting case of $\kappa' << 1$, ZT becomes a simple function of the Seebeck coefficient only and has the form $ZT \approx \alpha^2/L$. Based on the Sommerfeld value of L, the ZT of such a material can be estimated as $ZT \approx (\alpha/156)^2$. This broadens the focus of ZT optimization to include the less common idea of maximizing the electronic thermal conductivity in addition to the traditional emphasis on reducing the lattice contribution. Figure 1.1 has been included to demonstrate the importance of metallic resistivity for achieving high ZT at low temperatures. The plot shows the values of α necessary between 10 K and 1000 K to reach a ZT of unity for various fixed ρ, assuming $L = L_0$ and $\kappa_{lattice} = 0.1$ W/m-K.

These results are consistent with Slack's argument regarding the minimum U necessary for ZT of unity at room temperature. A semiconductor with a Hall mobility μ of 150 $\frac{cm^2}{Vs}$, a typical doping level n of 10^{19} cm^{-3}, and an effective mass $m^* \sim m_0$ would have a resistivity on the order of 10^{-5} Ω-m. Although Slack's calculation allows for some flexibility in regards to the range of suitable effective mass and doping level values appropriate for such a material, his result fits within the range of values plotted in Figure 1.1 [12]. The analysis presented here simply arrives at this conclusion from a more general set of criteria.

From Figure 1.1 it can be seen that even if a material is engineered to reach thermal conductivity values in the amorphous range of $\kappa_l = 0.1$ W/m-K, achieving $\kappa' \leq 1$ at 100 K requires the material to also display metallic electrical resistivity on the order of 10^{-5} Ω-m or less. Since achieving the minimum lattice thermal conductivity condition is not trivial, it is more reasonable to assume a value for κ_l of approximately 1 W/m-K or even larger,

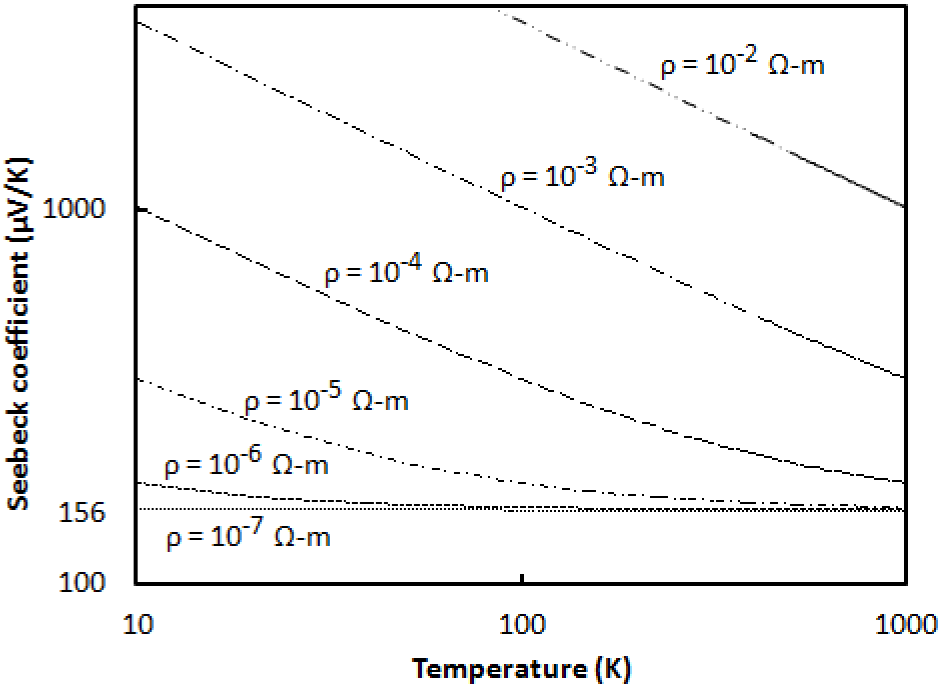

Figure 1.1: Plot of α necessary for $ZT = 1$ at various temperatures for the given values of ρ based on $L = L_0$ and $\kappa_{lattice} = 0.1$ W/m-K. Increasing $\kappa_{lattice}$ to a more reasonable 1 W/m-K shifts each line up one place.

which then requires a further reduction in resistivity to $\rho \leq 10^{-6}$ Ω-m to maintain $\kappa' \leq 1$, and $\rho \leq 10^{-7}$ Ω-m to improve this ratio to $\kappa' \leq 0.1$. Meanwhile, even if these low electrical resistivity and lattice thermal conductivity values are achieved, it is still necessary to have a Seebeck coefficient of at least 150 μV/K or larger to reach ZT values near unity.

This latter requirement is the problem that arises with conventional metals, which all have Seebeck coefficients on the order of only a few microvolts per kelvin [17]. This is two orders of magnitude lower than the range of values needed to achieve reasonably high ZT. For this reason, metals have traditionally been dismissed outright as candidate systems for thermoelectric applications [25]. Within this same temperature range, however, conventional semiconductors have resistivity values orders of magnitude too large to make high ZT possible. These trends together summarily explain why essentially no high ZT materials have yet been developed at cryogenic temperatures.

Based on this analysis, it becomes apparent that one or more of the traditional assumptions in thermoelectrics must give way if thermoelectric cryocoolers are to ever become a reality. This may be done by finding materials that violate the W-F law, display Lorenz numbers much smaller than the Sommerfeld value, and/or have lattice thermal conductivity values much lower than the "amorphous limit" of 0.1 W/m-K. Although each of these approaches may be theoretically possible, the few reported attempts at pursuing them suggest that they are most likely to be realized only in thin films, heterostructures, and/or through other extrinsic effects [28, 29]. The most likely path to achieving high ZT values in bulk materials at cryogenic temperatures therefore appears to be through the development of compounds with metallic $\rho \leq 10^{-6}$ Ω-m *and* semiconductor-like $\alpha\sim200$ μV/K. To explore how this unusual combination of properties may be possible, it is useful to consider the available mechanisms for introducing large Seebeck coefficients into otherwise metallic materials.

1.4.2.2 Increasing the Seebeck coefficient

The search for large α begins by considering a simple dimensional analysis, which shows that

$$\alpha \propto \frac{voltage}{temperature} \propto \frac{(charge)(voltage)}{(charge)(temperature)} \propto \frac{energy/temperature}{charge} \propto \frac{entropy}{charge}. \quad (1.10)$$

The Seebeck coefficient can thus be thought of as a measure of the entropy per charge carrier. This broad qualitative analysis can be extended by considering the fundamental postulate of statistical mechanics, which relates entropy S and degeneracy g through the relationship $S \propto \ln g$ [30]. Based on this relationship, it can be reasoned that α should be large when there are a large number of nearly energetically equivalent atomic states close to the average energy of the charge carriers.

This general notion is essentially equivalent to the argument developed by Mahan and Sofo, who more formally and more rigorously showed that α should be large in materials with sharp peaks in the electronic density of states (DOS) near the Fermi level [31]. This theory suggests that the closer these sharp features are to a pure delta function, the larger α should be. Since this theory makes no direct restrictions on the nature of the electrical resistivity, it may be used as a general guide to engineering materials with simultaneously large α and metallic ρ.

The validity of this paradigm can be demonstrated by considering the origin of favorable thermoelectric properties in many different materials. The simplest example of this is in materials with highly symmetric crystal structures, as a more symmetric real-space arrangement of atomic potentials can be used to create a more symmetric and therefore degenerate Fermi surface in momentum space. This particular argument has been invoked to explain, for example, how “valence band convergence” contributes to favorable thermoelectric properties in PbTe, which forms in the cubically symmetric rocksalt structure [32].

Other more complex mechanisms for increasing charge carrier degeneracy have also been developed. Among these is the manipulation of configurational and spin-orbital degeneracy in compounds such as transition metal oxides that rely on hopping mechanisms for conduction [33]. Other viable approaches include the introduction of electronic resonant states near the Fermi level (e.g. Tl-doped PbTe [34]) and the exploitation of strong electronic correlations in materials containing rare earth elements [35].

Of these possibilities, the two that appear most likely to result in bulk materials with metallic ρ and large α are resonant level effects in semi-metals and strongly correlated electron effects in rare earth intermetallic alloys. The work of Mahan and Sofo directly supports this conclusion, as they describe f electronic levels as “nature’s closest approximation to a delta function” in the DOS [31]. It is therefore of central importance to the development of cryogenic Peltier cooling technology to further explore these material systems and better understand how structure-processing-property relationships may be exploited in them to achieve enhancements in ZT.

1.5 CePd$_3$

Since strongly correlated rare-earth based compounds have been identified as perhaps the best way to achieve simultaneously metallic ρ and large α [31], it is appropriate to consider the origin of these effects in order to understand how they may be controlled and optimized.

An array of unusual electronic, structural, and magnetic properties are often observed in rare-earth compounds as a result of interactions among the f electronic states and the conduction band [36]. These interactions can sometimes result in a phenomenon known as intermediate valency, wherein the rare-earth atoms display a non-integer time averaged valence configuration. In simple terms, this is due to the oscillation of electrons between the nominally localized $4f$ states and the delocalized conduction band that causes the rare earth ions to vary in time between two valence configurations.

This effect is similar to mixed valency (MV), which is another commonly observed phenomenon in these materials. These effects are different, however, in that MV materials contain rare earth ions in distinct valence configurations that do not nominally change with time, while the rare earth ions in IV compounds are each continuously fluctuating between different configurations [36].

The fluctuating valence of rare earth ions in IV materials often corresponds with a large peak in the electronic density of states that often results in unusually high Seebeck coefficients of tens or even hundreds of microvolts per kelvin [37]. This effect tends to be especially pronounced in compounds containing cerium and ytterbium, wherein the presence of one $4f$ electron in cerium and one $4f$ hole in ytterbium often results in p-type and n-type behavior in these materials, respectively. Other rare earth elements, in particular europium and samarium, have also been known to display mixed and/or intermediate valence effects in certain compounds [38]. The abundance of both p-type and n-type materials displaying these correlated electron effects is encouraging in relation to their potential development for thermoelectric applications.

$CePd_3$ is one particularly well known p-type IV compound that has been extensively studied over the last several decades for various purposes. A clear indication of the IV effect in this material appears in the form of a significant deviation of the lattice parameter from the lanthanide contraction trend seen in the other RPd_3 compounds, where R is a trivalent rare-earth element [39]. This lattice parameter anomaly is common for both IV and MV compounds, and it arises from the significant size difference between the effective atomic radii of the R elements in their different valence states [39]. This property is also often accompanied by anomalies in the magnetic susceptibility, electronic specific heat, electrical resistivity, Mössbauer absorption spectra, and x-ray absorption near edge spectra, which can be used to distinguish between IV and MV effects [40].

$\mathrm{CePd_3}$ is an especially attractive candidate for cryogenic TE cooling due its desirable combination of $\rho \sim 10^{-6}$ Ω-m concurrent with $\alpha \sim 115\mu$V/K near 125 K. Both of these properties fall exactly within the range of values needed to achieve reasonably high ZT at low temperatures. In the limiting case of $\kappa' << 1$, $\mathrm{CePd_3}$ has a maximum potential $ZT \approx (115/156)^2 \approx 0.5$.

The main problem with this material is its relatively high lattice thermal conductivity that results in an unfavorably large κ' of approximately 5 near 100 K that drops to below unity above 200 K. These trends are summarized in Figure 1.2, which shows typical data for $\mathrm{CePd_3}$ available in the literature [41]. The combination of these properties results in ZT values for unmodified $\mathrm{CePd_3}$ of approximately 0.1 at 100 K and 0.2 at 300 K. The fundamental challenge that emerges is thus finding suitable mechanisms for reducing κ' and/or enhancing α in this material in order to increase ZT.

Several attempts have been made over the last several decades to improve this material's thermoelectric properties. With two lone exceptions, however, every reported attempt has shown a net decrease in ZT. Although the introduction of point defects through solid solution mixing and interstitial site filling appears to sharply reduce the thermal conductivity [42, 43], the IV state also tends to rapidly collapse when the physical and/or electronic structure of the material is perturbed. This reverts it back into a conventional metal, at which point it becomes a poor thermoelectric material.

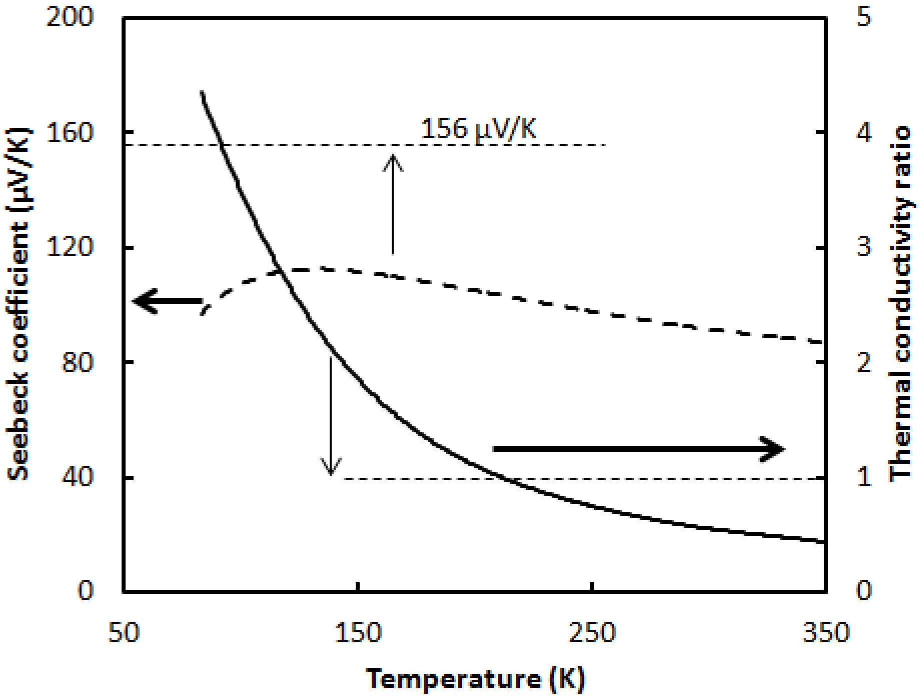

Figure 1.2: Seebeck coefficient α (dashed line) and thermal conductivity ratio κ' (solid line) of stoichiometric $CePd_3$ [41]. The semi-arbitrary target values of 156 μV/K for α and unity for κ' are indicated by the horizontal dashed lines connected to the left and right ordinates, respectively.

Since the basic goal of any thermal conductivity reduction strategy is to maximize the structural disorder of the material, the effects of these strategies tend to be inherently at odds with the sensitivity of the IV state to such perturbations. Finding solutions to this impasse requires the consideration of a broad range of structure/processing/property relationships that are not generally well understood in these materials. A comprehensive approach is thus needed in order to map the connections among the relevant material properties and then determine what mechanisms may be appropriate for enhancing ZT. Since $CePd_3$ is widely considered a good prototype IV compound, any insights gained concerning the relationships among its properties are likely to be useful in other similar materials as well.

In order to probe these relationships, several series of $CePd_3$-based compounds were synthesized, characterized, and analyzed for this study. The following is a brief and general review of the literature on this compound intended to provide an appropriate context for interpreting these results. Included in this review are several relevant structural, electronic, and magnetic property motifs that serve as useful reference points for comparing how the material's properties change in each of the series discussed subsequently.

1.5.1 Structural properties

$CePd_3$ is a relatively brittle compound that forms in the cubic Cu_3Au ($L1_2$) structure with cerium atoms occupying the corners of the cube and the palladium atoms occupying the faces, as illustrated in Figure 1.3. The simplicity of this compound's chemical formula and crystal structure allow for a robust variety of substitutions on both the cerium and palladium sites, including complete solid solutions with many different isostructural $R\mathrm{Pd}_3$ and $\mathrm{Ce}T_3$-type compounds, where R is a group III element and T is a transition metal or noble metal.

The effects of such substitutions on the electronic, magnetic, structural, and thermo-

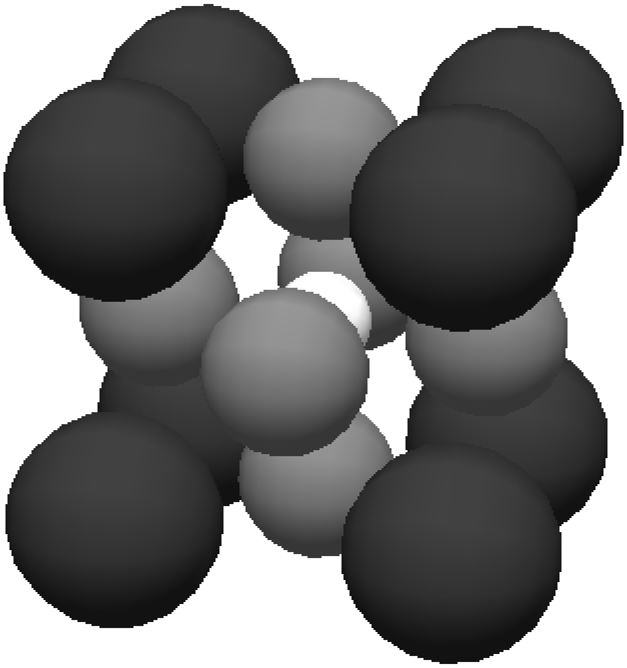

Figure 1.3: Diagram of the filled Cu_3Au crystal structure of $CePd_3$. The cerium atoms (dark gray) occupy the corners and the palladium atoms (medium gray) occupy the face centers. The central 1b interstitial site is identified here by the light gray sphere. This site is unoccupied in stoichiometric $CePd_3$, but it can be partially filled with various elements M to form $CePd_3M_x$.

electric properties of this compound have been studied extensively, with no reports of any structural ordering in any of the $Ce_{1-x}R_xPd_3$ or $Ce(Pd_{1-x}T_x)_3$ compounds for which data are available. This allows for a large phase space of possible substitutions on one or both of the lattice sites without concern over the secondary effects of structural ordering on the lattice dynamics and electronic structure of the material.

The central 1b octahedral interstitial site can also be partially filled with various elements, and much work on compounds such as $CePd_3B_x$ and $CePd_3Si_x$ with $0 < x < 1$ has been reported [39, 44, 45, 46, 47, 48, 49, 50, 51, 52]. This partial filling has the effect of locally transforming the filled unit cells into an analog of the perovskite ABO_3 structure. Extended structural ordering effects have been widely reported in some of these compounds [53, 54, 55, 56, 57], along with saturation limits for x that vary with the identity of M [44, 55]. In spite of this extensive study, the origins of these effects and their explicit impact on the thermoelectric properties of the material are generally not well understood.

Further details on the crystal structure and morphology of the material are presented below in the introductions to the relevant chapters.

1.5.2 Electronic and magnetic properties

A consequence of the IV effect in $CePd_3$ is that the cerium atoms fluctuate between the magnetically active Ce^{3+} and non-magnetic Ce^{4+} configurations at a frequency on the order of 10^{13} Hz [58]. This fluctuation between magnetic and non-magnetic states results in a random distribution of magnetic moments throughout the lattice that rapidly appear and disappear. Since the average valence of the cerium atoms is approximately +3.5 at room temperature [59, 58], roughly half of the unit cells contain a trivalent cerium atom at any given time. When a conduction electron encounters one of these atoms that has an electron in its $4f$ shell, the conduction electron can undergo spin-flip scattering with this $4f$ electron. This process is broadly known as the Kondo effect, and it is often apparent in the transport properties of such materials through a $\ln T$ contribution to the electrical resistivity [60]. The strength and nature of this interaction can vary significantly in different materials depending on things like the spatial distribution of the magnetic moments and the Fermi energy of the conduction band. In $CePd_3$, the high concentration of magnetic ions leads to the description of this material as a “Kondo lattice”, and the strength and nature of the Kondo interaction falls within the range referred to as a “lightly doped Kondo insulator” [61].

Every Kondo system has at least one important energy scale described by the Kondo temperature T_K; below T_K, various magnetic ordering effects can occur, while above T_K incoherent spin-flip scattering can have important consequences for the electronic properties [60]. Various theoretical models exist for describing how the Kondo effect can alter a material's electronic and magnetic properties [62]. In some cases, it can have an important impact on the electronic density of states in the form of a so-called “Kondo resonance” or “Kondo gap”, which can often result in a large Seebeck coefficient in these materials [35]. In this way, the value of T_K can be connected to the magnitude and temperature dependence of the Seebeck coefficient in Kondo-type systems [63, 64].

The Kondo effect is also explicitly important due to the direct connection it establishes between a material's magnetic properties and the temperature dependence of its electrical resistivity [60]. This connection allows for a broader perspective regarding how the electronic, magnetic, and structural properties of the material are related, including the ways that changes in these properties correlate with composition and processing modifications.

1.5.2.1 Electrical resistivity

The temperature dependence of the resistivity for a Kondo-type metal such as $\mathrm{CePd_3}$ can be very generally described as a sum of contributions from different terms [65]. Each of these terms is more or less prominent in different temperature regimes depending on the relative magnitudes of the Debye temperature Θ_D and the Kondo temperature T_K. This relationship is described by an extension of Matthiessen's rule [66], and is given by

$$\rho = \rho_0 + a_0 T + b_0 T^2 + c_0 T^5 + d_0 \ln T, \tag{1.11}$$

where ρ_0 is the residual resistivity at 0 K resulting from defects, a_0 is the coefficient of the linear contribution from lattice vibrations (electron-phonon scattering) for $T \sim \Theta_D$, b_0 is the coefficient of the Fermi liquid (electron-electron scattering) contribution typically relevant for very low temperatures only, c_0 is the coefficient of the higher order contribution from lattice vibrations (electron-phonon scattering) for $T << \Theta_D$, and d_0 is the coefficient of the Kondo term (spin-flip scattering).

The magnitude of d_0 in paramagnetic Kondo metals such as $\mathrm{CePd_3}$ can be described by the relationship

$$d_0 \propto J \left(\frac{m^*}{n}\right) \left(\frac{J}{E_F}\right)^2, \tag{1.12}$$

where J is the exchange energy between the localized and itinerant electrons and E_F is the Fermi energy [60]. One key aspect of this result is that the sign of J determines whether this additional contribution to the resistivity increases or decreases with temperature. In the case of $\mathrm{CePd_3}$, d is negative and large such that the resistivity decreases as $\ln{(1/T)}$ for $T_K < T \sim \Theta_D$.

This type of temperature dependence is one of the defining traits of a metallic Kondo system, as it is highly unusual for resistivity to decrease with increasing temperature in a normal metal [17]. One way of experimentally estimating T_K is to determine the lower limit of the temperature range within which the $\ln(1/T)$ description applies [60]. Since the nature of the interaction between the conduction electrons and the local $4f$ states changes below this temperature, it can be anticipated that other electronic and magnetic properties will show dramatic changes near T_K as well.

Generally speaking, the Kondo effect, the IV state, and large α should always be observed together in $\mathrm{CePd_3}$, since all three share similar origins. It is useful then to study how T_K changes with various modifications schemes, as information can be extrapolated from these trends regarding the limiting conditions within which large α will be observed. Since the peak values of ρ and α can both vary with T_K [42], this information may also allow the properties of the material to be tuned in such a way that they are optimized within a specific temperature range.

Based on Equation 1.12, variations in n and E_F introduced through different mechanisms may also have significant impacts on the strength of the Kondo effect. This can affect the relative magnitude of the coefficients in Equation 1.11, in turn changing the magnitude and temperature dependence of ρ. Both n and E_F play an important role in the magnitude and temperature dependence of the Seebeck coefficient as well, emphasizing the strong interdependence of all the electronic and magnetic properties of the material.

1.5.2.2 Hall coefficient

The Hall coefficient R_H is generally a reliable measure of the free carrier density n in most materials where electronic transport is dominated by one type of carrier. This relationship is given by

$$R_H = -\frac{V_H d}{IB} = \frac{1}{ne}, \tag{1.13}$$

where V_H is the Hall voltage, d_0 is the sample thickness perpendicular to the direction of the applied magnetic field B, I is the excitation current, and e is the elementary charge [17].

In strongly correlated systems, the combination of unusual electronic and magnetic effects has been shown to result in anomalous features in the Hall coefficient that can limit the effectiveness of this metric as a direct probe of the carrier density in these materials. For example, the sign of R_H changes from positive to negative in $CePd_3$ below approximately 50 K [67]. This type of sign change is usually indicative of a crossover in the majority carriers from holes to electrons [17]. In $CePd_3$, however, the sign of the Seebeck coefficient is positive for all $T > 0$, suggesting that holes remain the dominant carriers at all temperatures. This inconsistency can be resolved by quantum mechanical considerations that show the sign of R_H must be positive in this material for $T >> T_K$, but it can vary for $T \leq T_K$ [68]. This implies that R_H is not an appropriate measure of the carrier density for $T \sim T_K$, although it may be more useful for $T >> T_K$.

Even at higher temperatures, however, some reports exist that indicate the presence of an anomalous Hall effect in $CePd_3$ that is caused by skew scattering of the free carriers resulting from an asymmetric splitting of the Kondo resonance in a magnetic field [65]. For $T > 180$ K $\sim T_K$, R_H can be described by the relationship

$$R_H = R_0 + \frac{A}{T + \theta}, \tag{1.14}$$

where R_0 is a constant similar to the values measured in non-magnetic analog materials and A and θ are temperature independent material parameters [67]. Based on the combination of these observations of the Hall coefficient at both high and low temperatures, R_H can only loosely be utilized as a measure of the carrier density in this material.

Comparisons of n values determined by R_H measurements in $\mathrm{CePd_3}$ can be made with other measurements, such as optical reflectivity, that have been successfully used to determine a carrier density in $\mathrm{CePd_3}$ on the order of 10^{21} $\mathrm{cm^{-3}}$ [61, 69, 70] with a carrier effective mass of approximately 40 times the free electron value [69]. These experiments produce consistent results within the range $T \sim T_K$, suggesting that the high temperature correction does not significantly affect the utility of R_H for measuring n.

1.5.2.3 Magnetic susceptibility

$\mathrm{CePd_3}$ can generally be described as a paramagnetic material, as it displays a positive magnetic susceptibility χ without evidence of spontaneous ordering [44]. A Curie-Weiss description is therefore appropriate for fitting the temperature dependence of χ [21]. This description is given by

$$\chi = \chi_0 + \frac{C}{T - \theta}, \tag{1.15}$$

where χ_0 is a temperature independent term arising from Pauli paramagnetism, C is the Curie constant, and θ is the Neél temperature, below which antiferromagnetic ordering occurs.

The value of C is dependent on various magnetic properties, and for a two-state system it is proportional to the square of the total magnetic moment of the material [17]. Since trivalent cerium carries a magnetic moment while tetravalent cerium does not, C will change with the average valence of the cerium atoms, and can thus be utilized as a probe of the IV effect as the material is modified in various ways.

Direct determination of the effective moment of the cerium atoms in $\mathrm{CePd_3}$ is not trivial using this approach, as it requires at least a few assumptions regarding the nature of the magnetic properties. Equation 1.15 includes two unknown parameters (χ_0 and θ), and thus a measurement of χ as a function of T is insufficient to completely determine C. The value of χ_0 may nominally be calculated from first principles for a conventional metal, and it is usually small compared to χ [17]. This often leads to the assumption that this term can be neglected. However, given the close correlation in $\mathrm{CePd_3}$ between the behavior of the conduction electrons and valence of the cerium atoms, there are subtle relationships embedded among χ_0, θ, and C that can make it difficult to justify this assumption.

It is nonetheless useful to approximate Equation 1.15 as

$$\chi = \chi_0 + \frac{C}{T}, \tag{1.16}$$

which allows for the experimental determination of C from plots of χ versus $1/T$. When this fit function is applied over a relatively small range of temperatures, it often produces an approximately linear relationship among the variables. This allows for a self-consistent, semi-quantitative determination of C from which comparisons can be made regarding the magnetic moment of the cerium atoms in different $\mathrm{CePd_3}$-based compounds.

1.6 Thermal properties

One of the unique aspects of IV compounds in relation to thermal conductivity is the proposed existence of anomalous electron-phonon interactions that occur as the valence state and size of the R atoms concomitantly oscillate. Experimental evidence for these "breathing" effects have been reported in certain valence fluctuating compounds such as $Sm_{0.75}Y_{0.25}S$ [71] and SmS [72]. For this type of interaction to be possible, the characteristic "fluctuation temperature" T_f, which is proportional to the width of the $4f$ peak in the DOS and is associated with the frequency of valence oscillations, should be lower than the material's Debye temperature Θ_D [73].

These parameters in $CePd_3$ have been found to be 220 K [74] and 292 K [73], respectively, suggesting that it may be possible to observe the breathing effect in this compound. Some experimental evidence exists to support this possibility in the form of anomalous force constants in the <100> direction for $T \geq 140$ K observed in phonon dispersion data obtained through neutron diffraction experiments [75]. Optical absorption experiments indicate that this breathing term may correspond with an optical mode, which suggests that it does not have a significant impact on heat propagation in the material [76]. Although the impact of this breathing phenomenon on the thermal conductivity is not trivial to predict, it can be anticipated that this effect may be relevant when considering which possible solid solutions may be useful for thermal conductivity reduction.

In addition to this consideration, it has been shown that the Lorenz number of correlated metals is likely to be larger than the nominal Sommerfeld value L_0 derived for a free electron gas [65]. This deviation is estimated to be as large as a factor of two, which suggests that using L_0 to determine the electronic thermal conductivity of materials like $CePd_3$ provides only a conservative estimate of the lattice contribution. Since typically $\kappa_e \sim \kappa_l$ in these materials, it is important to keep this in mind when evaluating the effectiveness of any thermal conductivity reduction strategy, as the lattice contribution may be even smaller than the calculated values suggest.

Chapter 2

Experimental methods

The same general procedures were carried out for all of the series of materials examined in this study. Certain material systems required some deviation from these procedures, and these deviations have been specified in the appropriate sections. Characterization and measurement conditions were held constant in all cases to the extent possible in order to facilitate uniform comparison of material properties.

2.1 Materials synthesis

Samples were synthesized by combining pure elements together in the appropriate stoichiometric ratios and placing them onto a water-cooled copper hearth inside of a small arc furnace. The elements were obtained from commercial suppliers Sigma Aldrich and Alfa Aesar. The furnace chamber was evacuated by a rotary pump then refilled with flowing argon gas at a pressure of approximately 1 *atm*. Rare earth elements known to rapidly oxidize were mechanically polished immediately before use in an argon-filled glove box. A current of 50 A to 100 A was passed from the arc melter anode through the pieces to melt them together. The resulting ingots were flipped and remelted several times to promote homogeneity and ensure all starting pieces had been melted. Mass losses as a result of this process were generally on the order of 1% to 2% and assumed to be stoichiometric unless otherwise noted. The typical total mass of the samples was between 1.5 g and 5 g.

Additional synthesis steps were required for samples in the $\mathrm{CePd_3M}_x$ and the nanostructured series. These additional steps have been specified in the respective chapters below.

2.2 Materials characterization

X-ray diffractometry (XRD) was utilized on the samples after synthesis to examine their crystal structure, lattice parameters, and phase purity. Small pieces of each sample were crushed into powder with a mortar and pestle then placed on a glass slide and inserted into a Rigaku Miniflex II x-ray diffractometer with a Cu K-α x-ray source of $\lambda = 0.154$ nm in order to obtain diffraction patterns. The Jade 9.0 software package with the JCPDS XRD pattern database was used to characterize the phases present based on these patterns. Rietveld refinement [77] of the XRD patterns was performed using the open-source program General Structural Analysis System (GSAS) [78, 79] based on the appropriate structure type, atomic coordinates, and occupation numbers for each of the materials examined.

Scanning electron microscopy (SEM) in conjunction with energy dispersive x-ray spectroscopy (EDS) was also performed on several of the samples in order to examine their microstructure, homogeneity, and phase purity. This analysis was performed at the Michigan State University Center for Advanced Microscopy using a JEOL 64000V SEM. Powder samples were adhered to the aluminum sample holders with carbon tape, while larger pieces were secured to the holder with epoxy. Unless otherwise noted, all analyses were performed on fracture surfaces.

2.3 Transport property measurements

The thermoelectric properties of the samples were measured in a pair of Janis flow cryostats using a four probe technique. After the appropriate synthesis steps were completed, the samples were cut with a diamond tipped rotary saw into rectangular prismatic bars approximately 2 mm *x* 2 mm *x* 5 mm to 10 mm. One end of these bars was soldered directly to a rectangular copper bar with a small amount of phosphoric acid used as a flux to facilitate the wetting of the solder between the sample and the copper surface.

A small heater consisting of an 800 Ω resistor wrapped inside a sheath of copper foil was soldered onto the opposite end of the sample. The copper bar was attached to the cryostat and copper/constantan thermocouples were attached to the sample at two different points separated by distance l between the heater and the base. The entire apparatus was then evacuated to a pressure of approximately 10^{-7} torr. The temperature of the sample was controlled by a flow of liquid nitrogen outside of a primary copper radiation shield balanced by a block heater inside of the cryostat base. The entire apparatus was allowed to reach thermal equilibrium at each temperature point by waiting approximately 25 minutes before any data were collected. This experimental setup is illustrated in Figure 2.1.

The electrical resistivity was measured by applying a current I_ρ of approximately 0.1 A through the length of the samples and measuring the voltage V_ρ between the copper leads of the two thermocouples. The current was reversed and the voltage was measured again, and this value was averaged with the first measurement in order to minimize the effects of any contact resistance and Seebeck voltages arising between the sample and the contacts. The

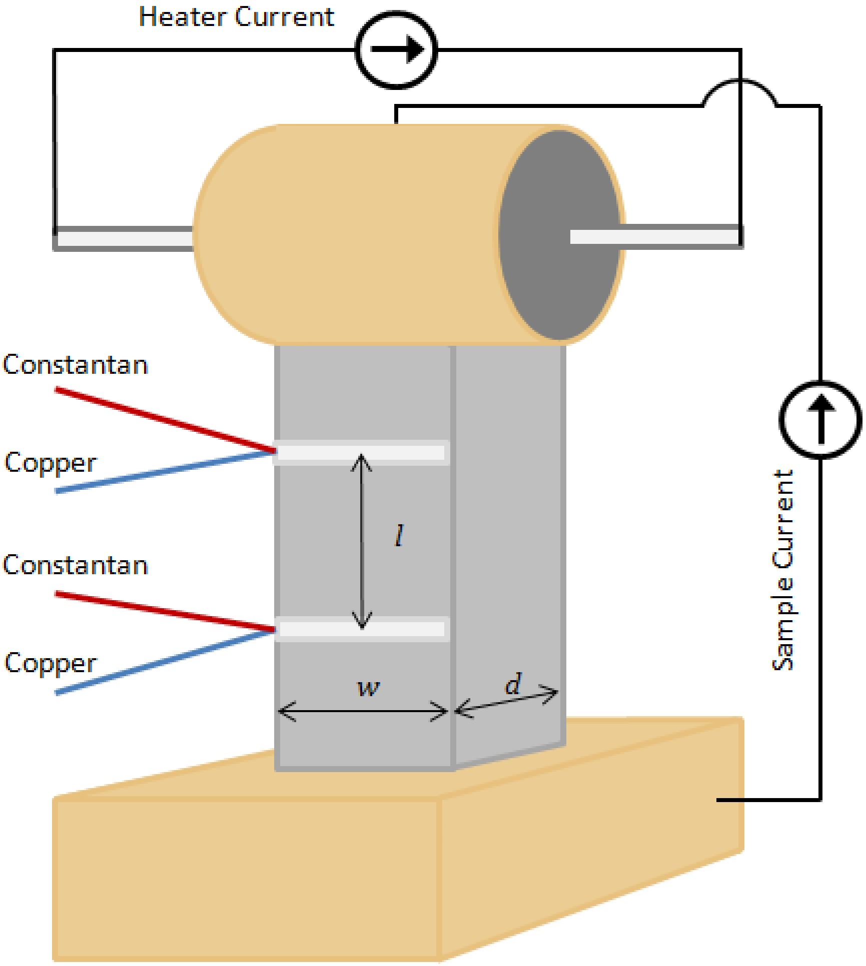

Figure 2.1: Schematic of the experimental setup used for transport property measurements. For interpretation of the references to color in this and all other figures, the reader is referred to the electronic version of this dissertation.

resistance ρ was then determined by the relationship

$$\rho = \left(\frac{V_\rho}{I_\rho}\right)\left(\frac{wd}{l}\right), \tag{2.1}$$

where w and d are the sample width and thickness, respectively. The total error in this measurement is estimated to be approximately 3%, resulting mostly from the limited precision of the sample dimension measurements.

After this measurement, the heater was activated by passing a current I_H of approximately 4 mA through the 800 Ω resistor. The system was allowed to reach a dynamic thermal equilibrium by sitting for five minutes before collecting any data. The Seebeck coefficient $S = (\Delta V_\alpha)/(\Delta T)$ was determined by measuring the voltage difference ΔV_α between the copper leads of the thermocouples then dividing this by the temperature difference ΔT between the leads. The error in this measurement is estimated to be approximately 3% based on the sensitivity of the thermocouple probes for determining the temperature gradient and the relative magnitude of the Seebeck voltages generated by the sample and the measurement apparatus.

The thermal conductance was then calculated based on the relationship

$$K_{measured} = \frac{I_H V_H}{\Delta T}, \tag{2.2}$$

where V_H is the voltage drop measured across the resistive heater. A radiation loss correction of

$$K_{sample} = K_{measured} - K_{radiation} \tag{2.3}$$

was applied, where K_{sample} is the true thermal conductance of the material and $K_{radiation}$

is determined by the relationship

$$K_{radiation} = (0.00146)\left(\frac{T}{300}\right)^3 \frac{W}{K}, \tag{2.4}$$

where T is the average absolute temperature of the sample. The value of 0.00146 W/K was determined by measuring a similarly sized sample of fused quartz at 300 K while the sample was disconnected from the copper base.

The total thermal conductivity κ of the sample was then determined by the relationship

$$\kappa = K_{sample}\left(\frac{l}{wd}\right). \tag{2.5}$$

Typical errors in the thermal conductivity data are estimated to be 10%, resulting from a combination of the limited precision of the sample geometry measurements, the radiation loss correction, and the accuracy of the thermal gradient measurements.

2.4 Magnetic property measurements

The magnetic susceptibility of some of the samples was measured in a Quantum Design superconducting quantum interference device (SQUID) magnetometer in the Physics and Astronomy Department at Michigan State University from 2 K to 300 K in a constant magnetic field of 5.5 T. The samples were prepared by placing them into a thin plastic pouch that was then rolled up and placed into a plastic straw. This straw was inserted into the SQUID, then the chamber was evacuated and the sample was cooled to 2 K. The samples were allowed to sit at each temperature point for approximately 15 minutes in order to reach thermal equilibrium before the susceptibility was measured.

The Hall coefficient R_H of several samples was measured from 80 K to 300 K using a standard five probe technique. A rectangular prismatic bar of each sample was prepared by cutting larger ingots with a diamond saw. These bars were then sanded to create sufficiently thin samples with dimensions of approximately 2 mm x 0.3 mm x 5 mm. The samples were placed on top of the copper base of a cryostat with two layers of insulating paper in between, with a non-conducting varnish used to adhere each layer to the next. Silver-based adhesive was used to connect silver wire to the samples in the appropriate arrangement, as indicated in Figure 2.2. A magnetic field was applied perpendicular to the slab and the resulting Hall voltage was measured. The field strength was varied from approximately -1.5 T to +1.5 T. A LakeShore 370 AC resistance bridge accurate to 10 nΩ was used to measure the Hall resistance while pulsing an excitation current of approximately 30 mA. The Hall coefficient was then extracted from plots of the measured Hall voltages versus applied field. The magnitude of the carrier density n was estimated by the relationship given by Equation 1.13.

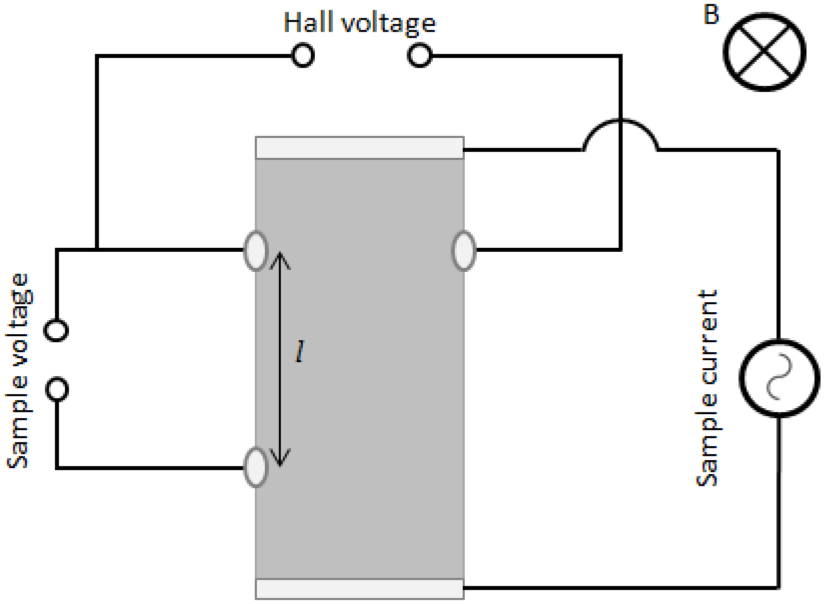

Figure 2.2: Schematic of the experimental setup used for Hall coefficient measurements.

Chapter 3

Cerium-site substitutions: $Ce_{1-x}Sc_xPd_3$

3.1 Background and motivation

Solid solutions of the type $Ce_{1-x}R_xPd_3$ have been reported to form for a wide variety of R elements, including gadolinium [80], yttrium [80, 81, 82, 83], neodymium [83, 84], lanthanum [83, 85], thorium [84], scandium [86], uranium [87], and manganese [88]. Available reports on the thermoelectric properties of these alloys typically show a substantial decrease in the Seebeck coefficient as x is increased for all R elements, although relatively large substitution levels near 20% can sometimes be obtained before any significant change in α occurs [83].

This relatively large substitution window suggests that it may be possible to reduce κ_l through solid solution mixing without substantially affectng α. It is not clear from these previous studies how effective cerium site substitutions are in reducing the thermal conductivity, as very few of them report such data.

Solid solution mixing has a maximum impact on κ_l when the substitutional element has a maximum mass and/or size mismatch with the host matrix [18]. Because of this, scandium appears to be an optimum choice for exploring the potency of cerium site substitutions as a means of thermal conductivity reduction due to its significantly smaller atomic size and mass relative to cerium.

Previous work by Gambke, et al. has demonstrated that the $Ce_{1-x}Sc_xPd_3$ solid solution forms for all x [86]. The lattice parameter generally decreases linearly with x, although this dependence appears to have two different slopes for $x < 0.3$ and $x > 0.3$. The decrease is relatively steep for $0 < x <0.3$ then becomes more gradual for $x > 0.3$. Gambke attributes this to a combination of Vegard's law superimposed on a change in the size of the cerium atoms resulting from a shift in the average valence toward the smaller 4+ state that saturates for $x \approx 0.3$. Since large α is not expected outside the range of x where the IV effect is observed, the range of compositions examined in this study was limited to $0 < x < 0.25$.

3.2 Experimental methods

Samples of $0 < x < 0.25$ were synthesized and measured in accordance with the procedures outlined in Chapter 2. No deviations from these procedures were necessary for any of the compositions in this series, and no heat treatments were applied to any of the samples after arc melting.

3.3 Results and discussion

3.3.1 Structural properties

XRD patterns obtained for each of the samples indicated single phase samples of the expected Cu_3Au structure type. No obvious signs of impurity phases or structural ordering were apparent in the diffraction patterns.

Included in Figure 3.1 are the lattice parameter values determined for each sample through Rietveld refinement of the corresponding XRD patterns. An approximately lin-

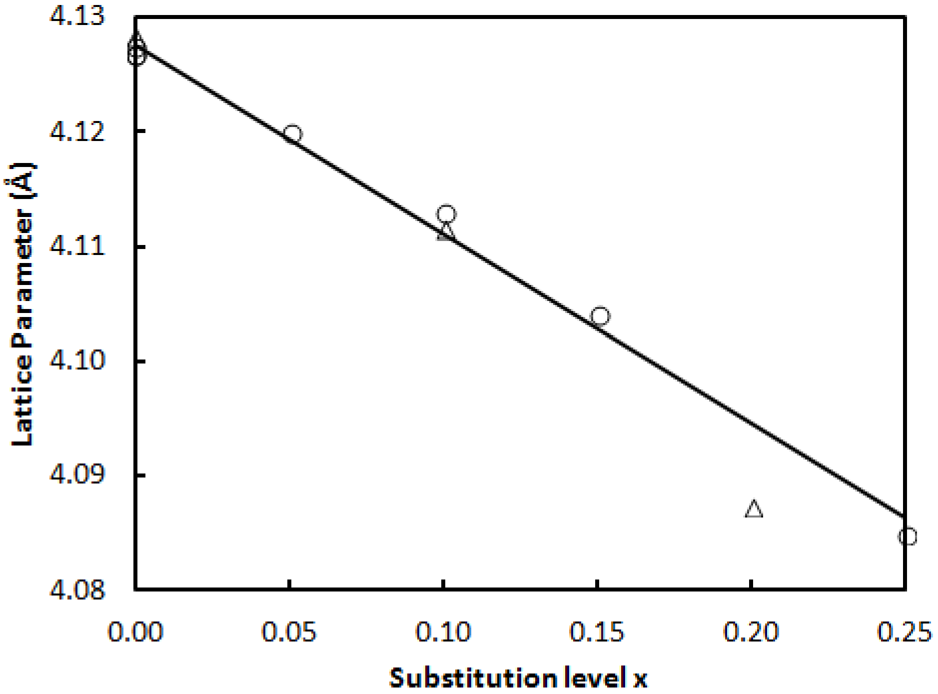

Figure 3.1: Lattice parameters of the $Ce_{1-x}Sc_xPd_3$ solid solution from Gambke (triangles) [86] and from this study (circles) as determined by Rietveld refinement of XRD patterns. The solid line is a linear fit to the data.

ear decrease is observed as x is increased, consistent with previous reports [86].

3.3.2 Electronic properties

The Seebeck coefficient data have been included in Figure 3.2. Consistent with the general trends widely reported for other $Ce_{1-x}R_xPd_3$ materials, a relatively large peak of approximately 100 μV/K is observed near 125 K for samples with $0 < x < 0.1$. Above this substitution level, the magnitude drops steadily and the peak flattens out.

This change in the magnitude and temperature dependence of the Seebeck coefficient correlates with the increased substitution of scandium atoms into the cerium sites. Although the nearest-neighbor environment of the cerium atoms is not directly affected by this type of substitution, the smaller size of the scandium atoms induces a contraction of the lattice

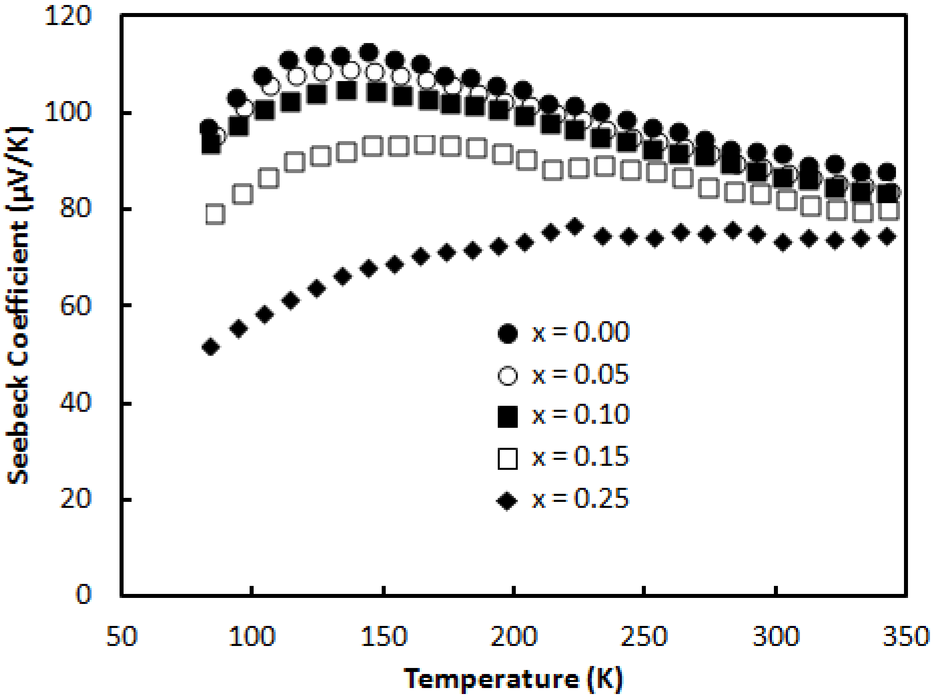

Figure 3.2: Seebeck coefficient of $Ce_{1-x}Sc_xPd_3$.

parameter that appears to create a chemical pressure on the cerium atoms, pushing them toward the smaller Ce^{4+} configuration. This alters the IV state and thus indirectly affects the Seebeck coefficient.

The electrical resistivity results have been included in Figure 3.3 and show no significant variation in magnitude for any of the compositions studied. The temperature variation appears to go through a maximum for $x = 0.10$ at 80 K before decreasing again. The magnitude of the Kondo temperature T_K appears to be shifting to temperatures below 80 K as x is increased. The temperature dependence of the $x = 0.25$ sample is distinctly flat compared to the others, indicating the beginning of a transition away from the $\rho \sim \ln(1/T)$ Kondo regime to conventional metallic behavior of $\rho \sim T$. The onset of this transition is consistent with the lattice parameter trends in Reference [86].

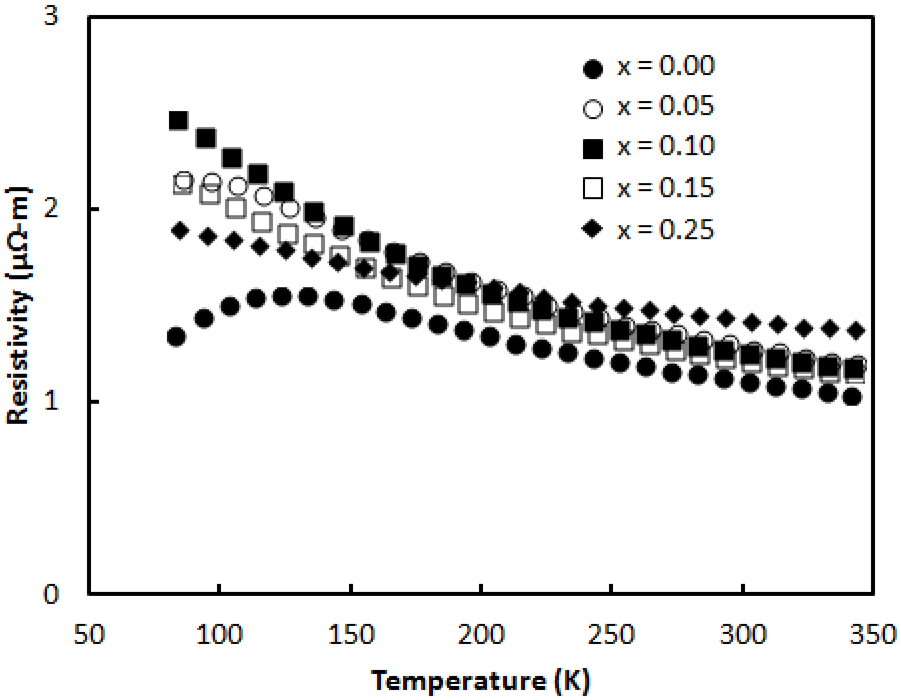

Figure 3.3: Electrical resistivity of the $Ce_{1-x}Sc_xPd_3$ solid solution.

3.3.3 Thermal properties

Figure 3.4 has been included to show the temperature dependence of the lattice thermal conductivity for each sample in this series. It is apparent from these data that scandium substitution has only a modest affect on the lattice thermal conductivity, as all compositions show values approximately 1 W/m-K to 1.5 W/m-K lower than those of the unmodified compound. These values correspond with reductions in magnitude of approximately 25%. No trend is apparent between the scandium content and the observed reductions, as all compositions with $0.05 < x < 0.25$ show nearly identical values within the error of the measurement throughout the entire temperature range examined.

The ineffectiveness of cerium site substitutions in reducing the lattice thermal conductivity may be explained by the so-called “breathing” of the cerium atoms discussed previously that occurs as these atoms rapidly change size at a time scale on the order of the atomic

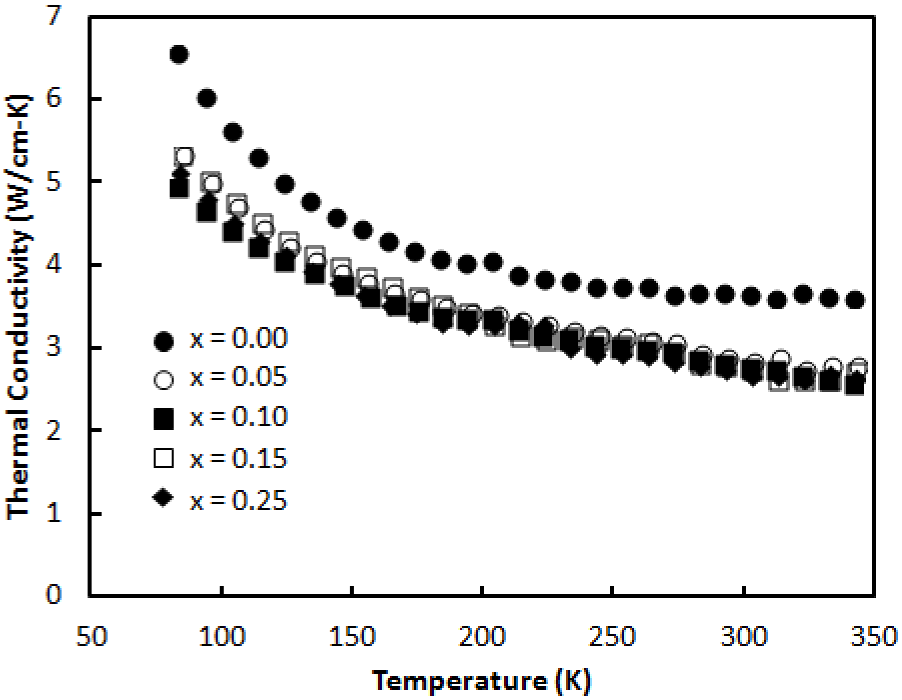

Figure 3.4: Lattice thermal conductivity of the $Ce_{1-x}Sc_xPd_3$ solid solution.

vibrations. Since scandium gives the maximum possible size and mass mismatch with the cerium atoms, any potential reduction in the lattice thermal conductivity resulting from substitutions on this site should be most easily observed in this system. Since no significant reduction has been observed, it appears that these lattice sites do not play a significant role in the net transport of thermal energy through the lattice, consistent with the idea that the "breathing" term corresponds with an optical phonon mode(s).

Although a modest reduction in the lattice thermal conductivity was observed in these samples, the corresponding increase in electrical resistivity produced a simultaneous decrease in the electronic thermal conductivity. As a result, the value of κ' is not improved for any of the compositions studied. The results of this analysis are included in Figure 3.5.

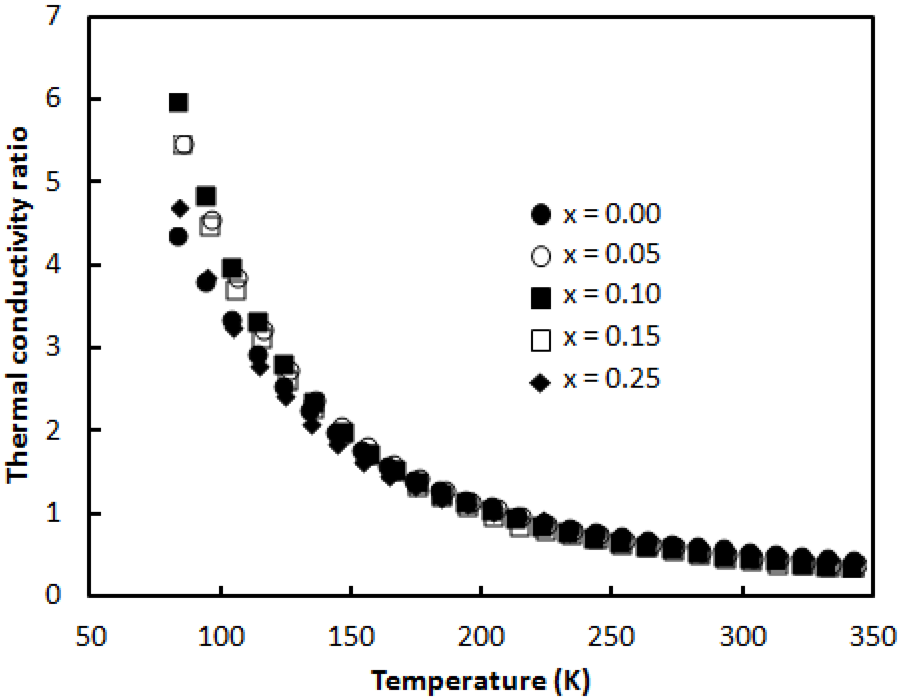

Figure 3.5: Thermal conductivity ratio of the $Ce_{1-x}Sc_xPd_3$ solid solution.

3.3.4 General conclusions and ZT

The combination of a decrease in the Seebeck coefficient and an increase in κ' resulted in no net enhancement in ZT for any of the samples in this series, as seen in Figure 3.6.

Based on the data presented here in conjunction with the available reports on similar $Ce_{1-x}R_xPd_3$ studies, it appears that cerium-site substitutions are an ineffectual approach for improving the thermoelectric properties of the material. Although the nearest-neighbor environment of the cerium atoms remains unchanged, the chemical pressure introduced by the substitution of the smaller scandium atoms pushes the cerium atoms toward the smaller tetravalent configuration. The thermal conductivity reduction reported here is relatively large compared to the results of other studies for cerium-site substitutions, but this improvement is insufficient to produce any enhancement in ZT. The proposed "breathing" effect of the cerium atoms as they fluctuate in size may be related to the limited efficacy of

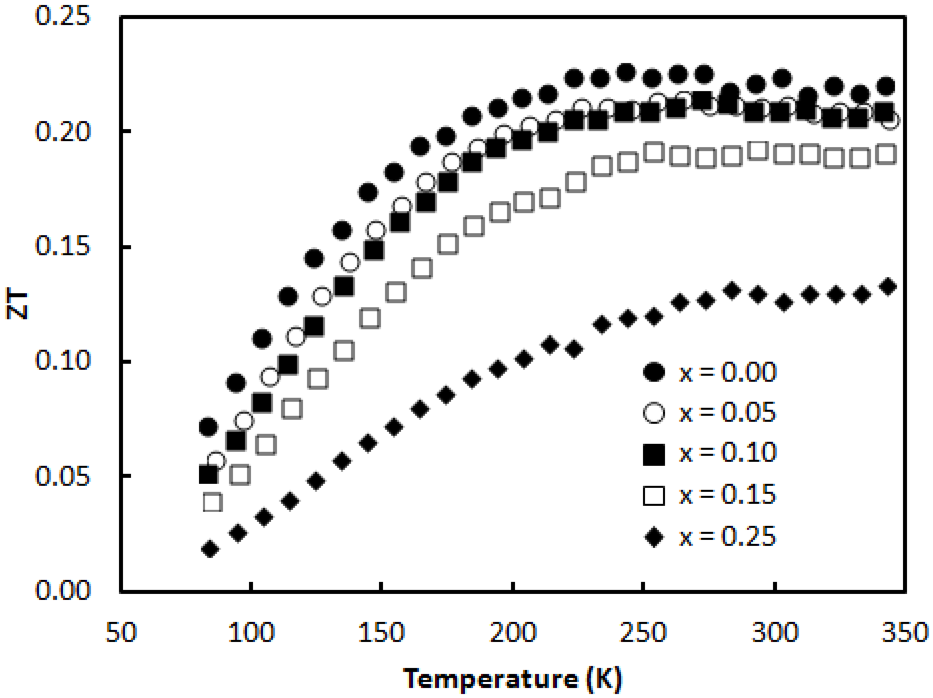

Figure 3.6: Thermoelectric figure of merit of the $Ce_{1-x}Sc_xPd_3$ solid solution.

cerium-site substitutions for reducing κ_l. The implication of these results is that substitution on the palladium site should have a substantial effect on the lattice thermal conductivity. Beyond $CePd_3$, these results suggest that substitutions on the R site in valence fluctuating compounds with $T_f < \Theta_D$ may not generally be effective for decreasing the thermal conductivity, depending on the type of phonon mode that correponds with the "breathing".

Chapter 4

Palladium site substitutions: $CePd_{3-x}Pt_x$

4.1 Background and motivation

The results of the $Ce_{1-x}Sc_xPd_3$ study in Chapter 3 suggest that the cerium site plays only a minor role in phonon propagation. This in turn implies that palladium site substitutions should be an especially effective approach for reducing the thermal conductivity. Reports on $CePd_{3-x}Rh_x$ and $CePd_{3-x}Ag_x$ solid solutions by Lackner [43] have shown that this is generally true, as that work has demonstrated a relatively substantial reduction in lattice thermal conductivity of approximately 50% for those systems as x is increased.

Those reports also indicated that these substitutions have a significant impact on the other properties of the material, including the Seebeck coefficient, electrical resistivity, and lattice parameter. Although these changes tend to be detrimental overall, Lackner does report a slight increase in ZT for one sample of $CePd_{2.7}Rh_{0.3}$. He shows that ZT values up to approximately 0.15 at 100 K and 0.25 at 300 K can be reached in this compound as a result of balancing the reductions in both κ_l and α. These ZT values correspond with increases of approximately 50% and 10%, respectively, over the base compound. A similar study by Sales [37] briefly mentions an increase in ZT up to approximately 0.15 at 100 K for $CePd_{2.655}Pt_{0.3}$, although no other transport data or compositions in the series were

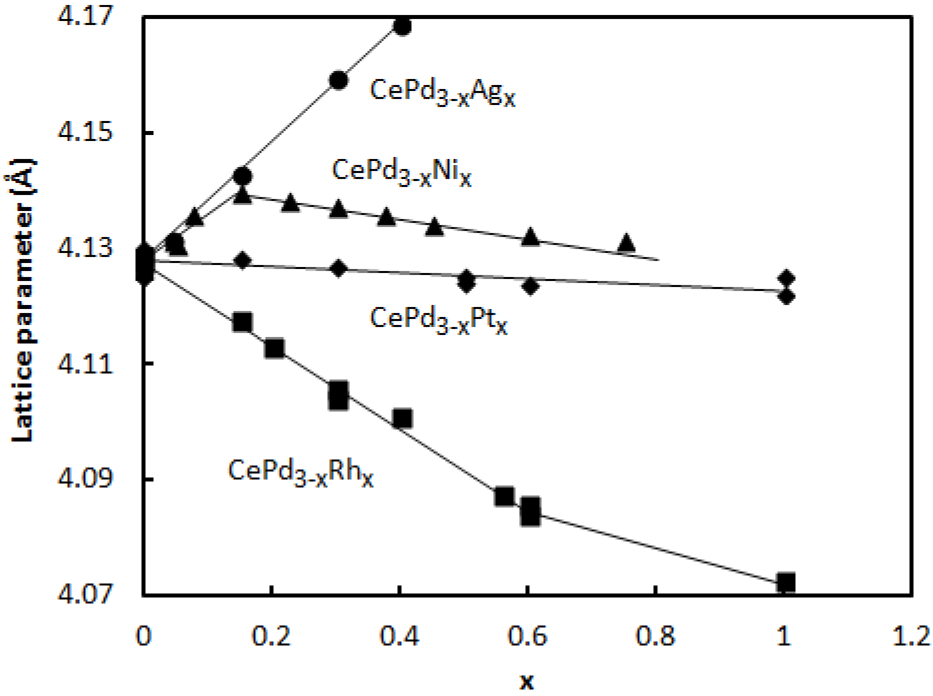

Figure 4.1: Reported lattice parameters for $CePd_{3-x}T_x$ (T = Ni [89], Ag [89], Rh [59], Pt [90]) series. Solid lines are a guide for the eye.

included in that report. It is worth noting that these are the only two reports that have ever indicated an increase in ZT relative to unmodified $CePd_3$, and both result from palladium site substitutions.

Based on these limited studies, it appears that there may be additional opportunities for improved thermoelectric performance within the $CePd_{3-x}T_x$ phase space. A simple way to filter through the possibilities for T is to consider the strong correlation between the IV state and the lattice parameter. This connection implies that any large change in the size of the unit cell is likely to correspond with substantial changes in the IV state and therefore the electronic properties. The available lattice parameter data for various solid solutions of T = Ni [89], Ag [89], Rh [59], and Pt [90] have been compiled in Figure 4.1.

The trends in Figure 4.1 for silver and rhodium substitution appear to be relatively straightforward, as these atoms are larger and smaller, respectively, than palladium, resulting in a corresponding increase and decrease in the unit cell size. An unusual result can be seen, however, for the nickel-substituted samples. In this series, the lattice parameter first increases with x up to approximately 0.05, then decreases for all x above 0.05. This initial increase coincides with a change in the cerium valence towards the larger trivalent state [89], which saturates at $x = 0.05$. The cerium atoms thus have a fixed size for all x above 0.05, and a simple Vegard's law behavior is observed in this range as the lattice parameter begings to decrease with increasing x [89]. A similar but more subtle trend can be seen in the samples containing rhodium, where a saturation of the cerium atoms in the smaller 4+ configuration occurs for $x \approx 0.6$ [59], corresponding with a kink in the trend.

In contrast to these trends, the lattice parameter of the platinum-substituted series does not appear to change much as x is increased. Platinum has a nearly identical valence configuration, size, and electronegativity relative to palladium [91], which suggests that the substitution of one for the other does not significantly change the nearest neighbor environment of the cerium atoms. The relative uniformity of the lattice parameter data supports this idea, as do data for χ and ρ in this series [90].

Although no Seebeck coefficient data for this system have been previously reported, it can be anticipated from these trends that α will also be close to the original values seen in $CePd_3$. In conjunction with this expected preservation of α, the substantial mass difference between platinum (195.08 amu) and palladium (106.42 amu) should sharply decrease the lattice thermal conductivity. This hypothesis, encouraged by the limited results of Sales on similar compounds [37], has provided strong motivation for further study.

4.2 Experimental methods

Samples of $CePd_{3-x}Pt_x$ with $0 < x < 1$ were synthesized and measured in accordance with the procedures outlined in Chapter 1. A maximum of $x = 1$ was chosen based on the work of Rambabu, et al. who reported this substitution level to be the solubility limit of platinum into the palladium sites of the Cu_3Au structure [92]. Due to the proximity of the compositions studied herein to the reported solubility limit, SEM and EDS experiments were performed to search for evidence of any secondary phases.

4.3 Results and discussion

4.3.1 Structural properties

Analysis of XRD patterns for each of the $CePd_{3-x}Pt_x$ samples indicated the presence of the expected Cu_3Au-type phase with no apparent secondary phases. A slight decrease in the lattice parameter was observed as x was increased, as seen in Figure 4.2 and consistent with previous reports for this solid solution.

Due to the limited solubility of platinum into $CePd_3$ [92], it is possible and perhaps likely that some ordering of the platinum occurs as the composition approaches the solubility limit. Although such ordering may have an impact on the transport properties of the material, no obvious signs of ordering were present in the XRD patterns, consistent with previous reports [90]. SEM analysis of the fracture surface of the $CePd_2Pt$ samples showed grains on the order of 10 microns. EDS results have been included in Figure 4.3 and indicate that cerium, palladium, and platinum were present a ratio of 1:2:1 to within 2% of the expected ratio as determined by averaging over several area and point spectra. The apparent homogeneity of

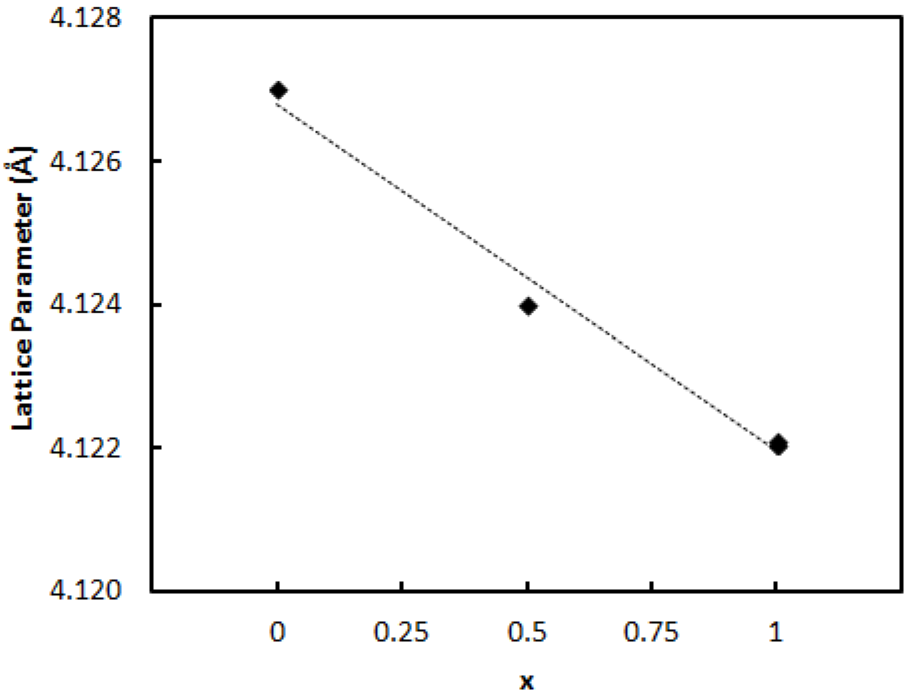

Figure 4.2: Lattice parameters of the $CePd_{3-x}Pt_x$ solid solution determined by Rietveld refinement. Dashed line is a guide for the eye.

the microstructure and composition support the XRD results that show no signs of impurity phases in the material.

4.3.2 Electronic properties

Measurements of the Seebeck coefficient have been included in Figure 4.4. Consistent with the initial hypothesis, large α is observed for all x. This result sharply contrasts with the trends of nearly every other study of chemically modified $CePd_3$ series for which Seebeck coefficient data are available, which all show dramatic changes in α as the composition is changed.

A slight enhancement in α occurs as x is increased that coincides with a more gradual slope of the α versus T dependence above $T \approx 150$ K. Since the substitution of platinum

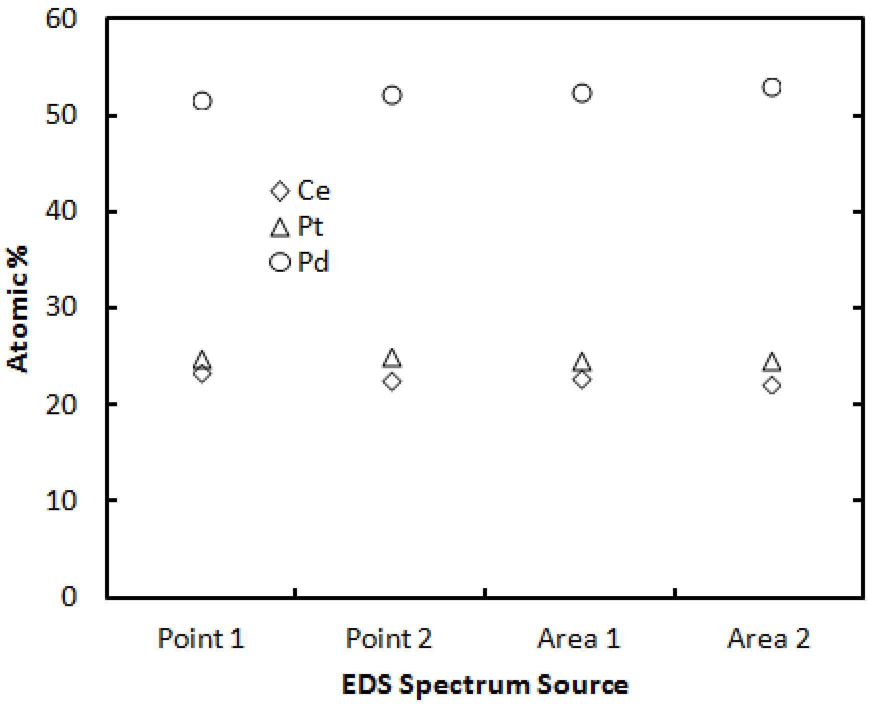

Figure 4.3: EDS analysis results for $CePd_2Pt$ indicating the presence of cerium, palladium, and platinum in a ratio of 1:2:1 within 2%

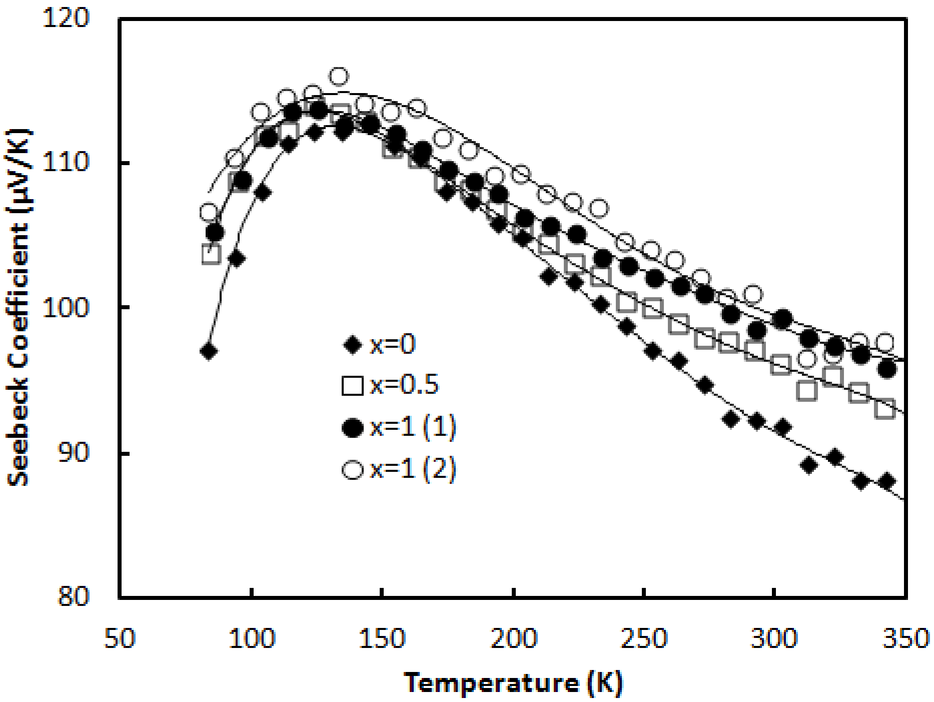

Figure 4.4: Seebeck coefficient of the $CePd_{3-x}Pt_x$ solid solution. Solid lines are a guide for the eye.

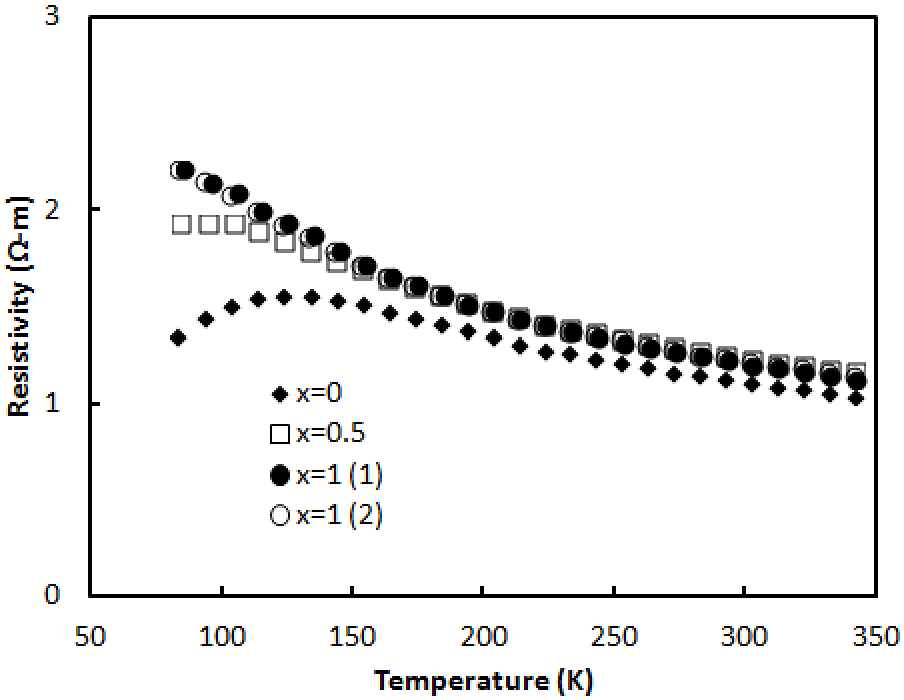

Figure 4.5: Electrical resistivity of the $CePd_{3-x}Pt_x$ solid solution.

is not expected to significantly alter the electronic structure, this modest increase in α can best be explained as a result of the chemical pressure introduced by the slightly smaller platinum atoms constricting the size of the unit cell. This appears to affect α in a way similar to mechanical pressure, as the latter has been shown to reduce the lattice parameter [93] and produce relatively substantial increases in α on the order of 30% when the material is subjected to several GPa of external pressure [94, 95].

The electrical resistivity data are included in Figure 4.5 and show that a slight increase in magnitude as well as a change in temperature dependence occur as the platinum content is increased. These trends are consistent with the available reports in the literature [90] and indicate a slight decrease in T_K. The lack of any large change in ρ implies that the magnitude of κ_e is nearly constant as a function of x.

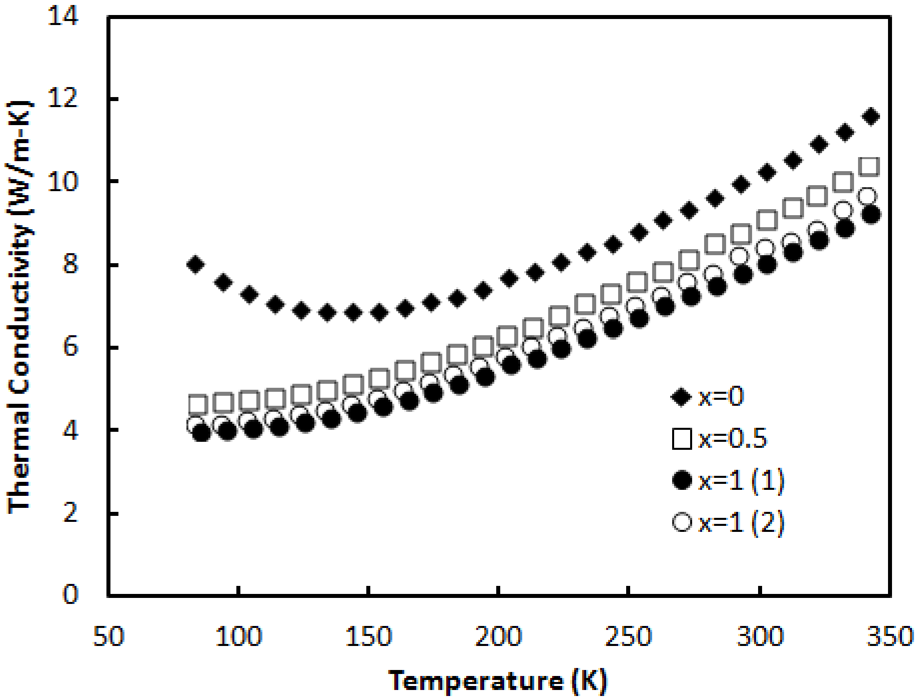

Figure 4.6: Total thermal conductivity of the $\mathrm{CePd}_{3-x}\mathrm{Pt}_x$ solid solution.

4.3.3 Thermal properties

The total thermal conductivity of the $\mathrm{CePd}_{3-x}\mathrm{Pt}_x$ series is included in Figure 4.6. The effects of platinum substitution on the thermal conductivity are dramatic, especially in comparison to the relatively small changes observed in the Seebeck coefficient and resistivity described above.

As seen in Figure 4.7, the reduction in the total thermal conductivity can be attributed almost entirely to a large reduction in the lattice contribution. Since platinum substitution introduces only a slight change in the lattice parameter, this reduction in κ_l can be explained as a result of the large mass mismatch between the platinum and palladium atoms and not from strain effects. This result also emphasizes the potency of palladium-site substitutions in scattering phonons, in contrast to the minimal effects seen for $\mathrm{Ce}_{1-x}\mathrm{Sc}_x\mathrm{Pd}_3$.

In order to consider the net effects of the changes in the lattice thermal conductivity and

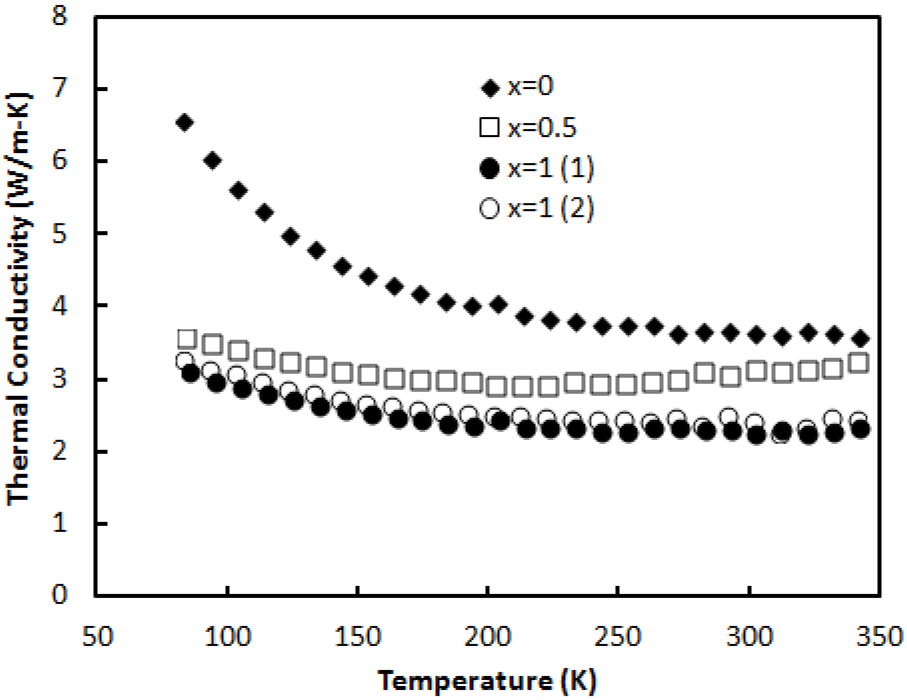

Figure 4.7: Lattice thermal conductivity of the $CePd_{3-x}Pt_x$ solid solution.

electrical resistivity, Figure 4.8 has been included to show how κ' changes with platinum content.

Overall, the substitution of platinum into the palladium sites results in a favorable decrease in κ' at all temperatures. When combined with the improvement in Seebeck coefficient seen in Figure 4.4, these samples show an overall improvement in thermoelectric performance for all x and T.

4.3.4 Magnetic properties

It is useful to examine the magnetic properties of this material in order to better demonstrate the subtle ways that the platinum substitution affects the cerium valence. It has been previously shown that the substitution of platinum into $CePd_3$ results in a slight change in the cerium valence toward the 4+ state [90, 92]. In order to confirm this in the compounds

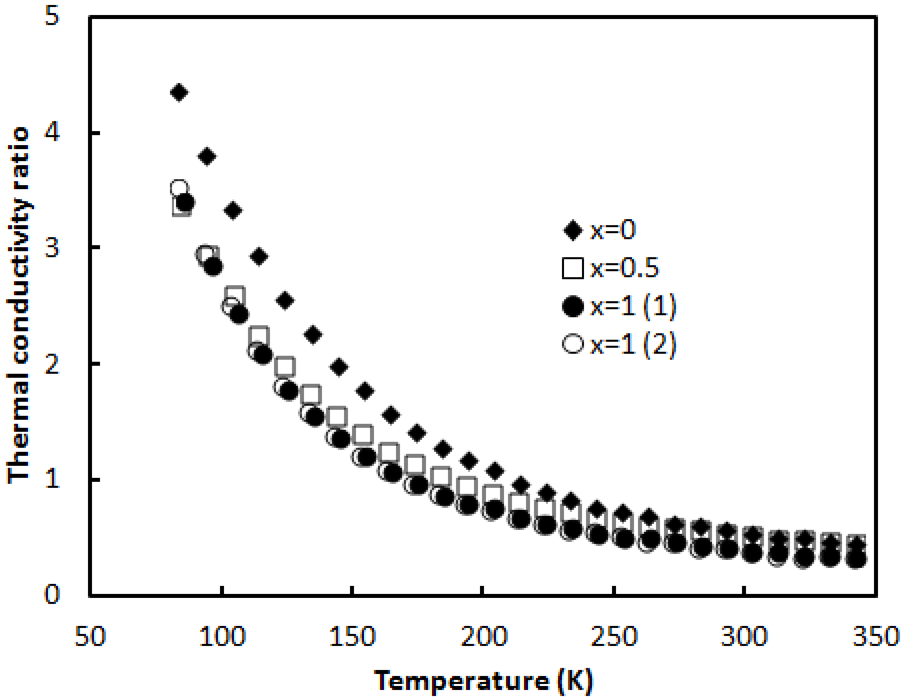

Figure 4.8: Thermal conductivity ratio of the $\mathrm{CePd}_{3-x}\mathrm{Pt}_x$ solid solution.

studied here, magnetic susceptibility measurements were performed on samples of CePd_3, $\mathrm{CePd}_{2.5}\mathrm{Pt}_{0.5}$, and $\mathrm{CePd}_2\mathrm{Pt}$. The results of these experiments are included in Figure 4.9.

The changes in the susceptibility are relatively minor and consistent with those reported in the literature. An examination of the high temperature (200 K to 300 K) dependence of χ versus $1/T$ was used to determine the Curie constant. This analysis is included in Figure 4.10 with the resulting values of C labeled on the plot. The decreasing values of C with increasing platinum content support the hypothesis that the cerium valence is shifting towards the tetravalent state as x is increased.

4.3.5 General conclusions and ZT

The combination of large α and reduced κ' in these materials results in increases in ZT for all x at all T. The ZT of both $\mathrm{CePd}_2\mathrm{Pt}$ samples studied here match each other exceptionally

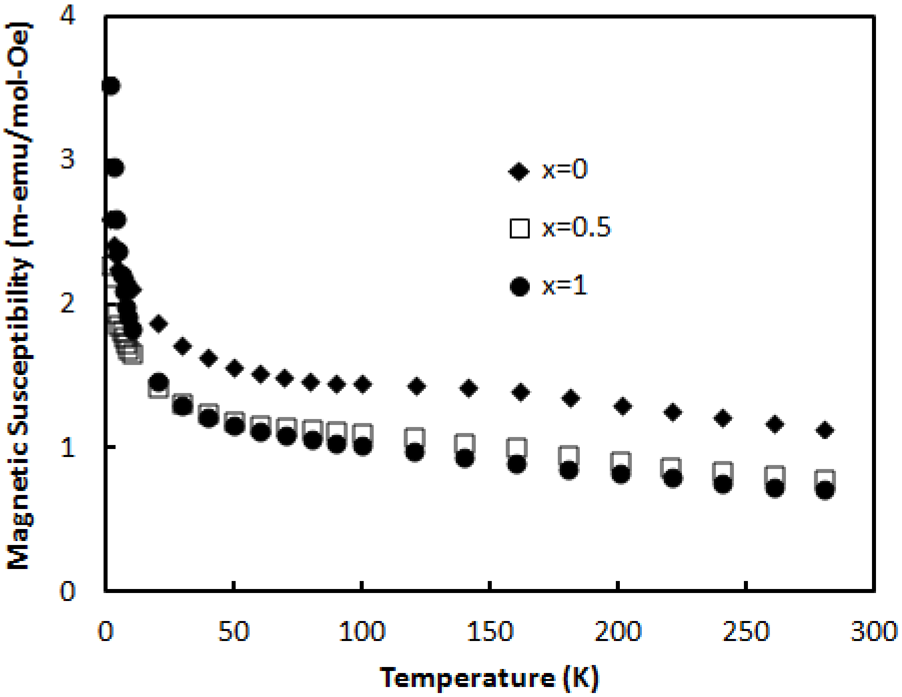

Figure 4.9: Magnetic susceptibility of the CePd$_{3-x}$Pt$_x$ solid solution.

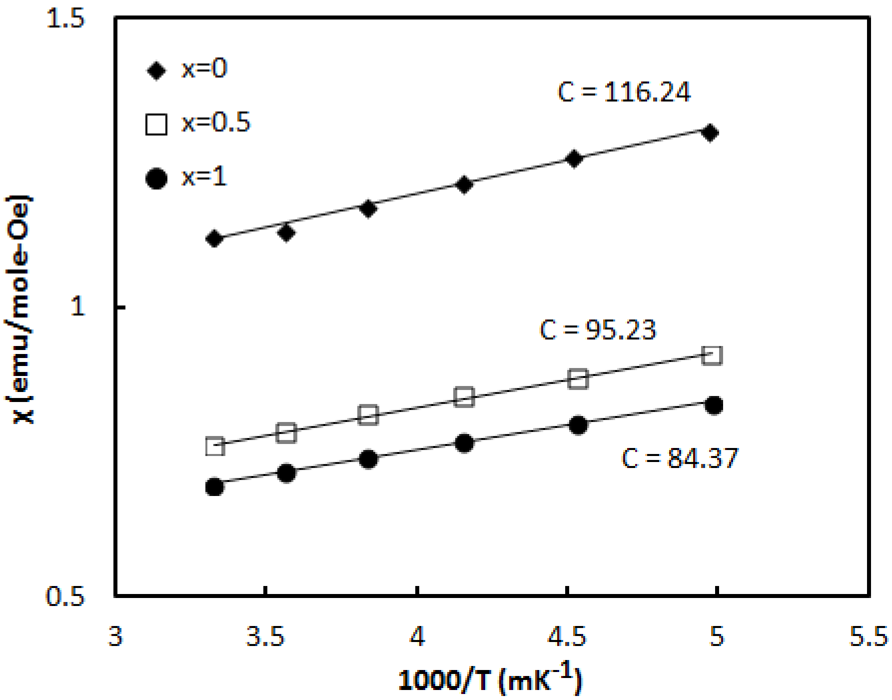

Figure 4.10: High temperature susceptibility of the CePd$_{3-x}$Pt$_x$ solid solution plotted against 1000/T. Solid lines are linear fits of the form $\chi = \chi_0 + C/T$. The values of C were extracted from these fits and are indicated on the figure in units of emu-K/mole-Oe.

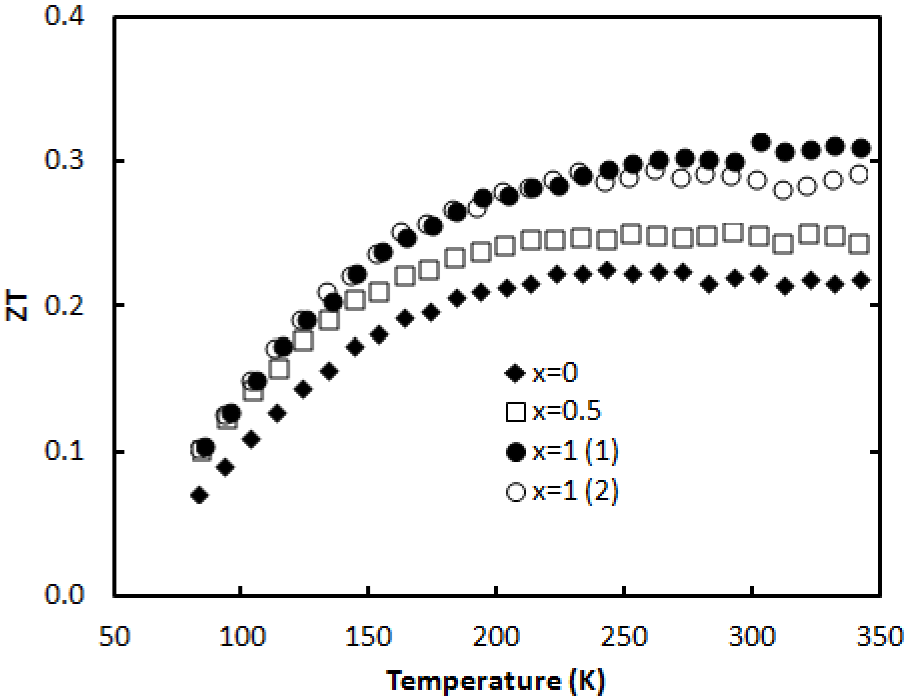

Figure 4.11: ZT of the $CePd_{3-x}Pt_x$ solid solution.

well. A maximum value of approximately 0.3 occurs above 250 K that corresponds with an improvement of approximately 35% over the control sample. This value is the highest ever reported for any $CePd_3$-based material.

Three main conclusions emerge from this study. The first is support for the idea that palladium site substitutions are generally more effective for reducing the lattice thermal conductivity relative to cerium-site substitutions. The second conclusion is that careful selection of substitution elements based on factors such as their size, electronegativity, and valence configuration can allow for a minimal perturbation of the local cerium bonding environment, which can enable substitutions on the order of 30% without having any significant impact on the IV state. The third important conclusion is that chemical pressure introduced by the substitution of smaller elements into the lattice can mimic the effects of applied mechanical pressure. This idea is not new, but the important distinction demonstrated here is that the substitution element should be carefully selected to match the chemical properties of the host matrix if the effect is to be properly isolated. The importance of this is readily demonstrated by considering the studies involving silver, nickel, and rhodium substitution mentioned above, in which dramatic changes in the lattice parameter and electronic properties were observed as the palladium content was decreased. Although these elements do introduce chemical pressure, they also cause changes in the local cerium environment and the electronic structure, making it essentially impossible to differentiate the impact of each mechanism separately.

Since platinum appears to be the optimal T element available for substitution onto the palladium site, this approach may already be exhausted as a way of improving the thermoelectric properties of the material. Additional study of this approach may be possible by doubly substituting onto the palladium site with platinum and a small amount of another element such as rhodium. Given the minimal improvement in the thermal conductivity that was gained in Figure 4.7 by increasing the platinum content from $x = 0.5$ to $x = 1$, however, it does not seem likely that any further reduction can be achieved through this route.

Chapter 5

Interstitial site filling: $\mathrm{CePd_3M}_x$

5.1 Background and motivation

Work by Lackner, et al. [42] has shown that partially filling the central interstitial site of the cubic Cu_3Au structure with boron is an effective way of lowering the thermal conductivity of the material through the introduction of point defect phonon scattering. The problem with this approach, however, is that the electrical resistivity and Seebeck coefficient are also sharply affected by the presence of the boron atoms. The combination of these factors led to no net enhancement in ZT for any of the $\mathrm{CePd_3B}_x$ compounds reported in Lackner's study. It is therefore important to better understand the specific ways in which these filler atoms affect the electronic properties of the material in order to fully assess the potential of this approach for increasing ZT.

These changes in the electronic properties can be attributed to the rapid change in cerium valence toward the Ce^{3+} state that occurs in materials like $\mathrm{CePd_3B}_x$ and $\mathrm{CePd_3Si}_x$ as x is increased. This valence change has been observed through lattice parameter, magnetic susceptibility, neutron diffraction, and specific heat data for these compounds [39, 44, 45, 46, 47, 48, 49, 50, 51, 52]. Additional reports by other groups on the electrical resistivity and magnetic susceptibility of samples filled with varying amounts of beryllium [96], aluminum [55, 97], gallium [55], and germanium [55] show similar shifts in the cerium valence toward the trivalent state as the filling fraction is increased, suggesting that a general trend may exist for all M.

In addition to these studies of partially filled samples, work by multiple research groups has shown that an ordered $Ce_8Pd_{24}M$ phase forms for certain M elements such as gallium [53, 54], indium [53, 54], tin [53, 54], antimony [53], lead [53, 54], bismuth [53], germanium [54, 55, 56], aluminum [54, 55, 97], and manganese [57], as well as possibly zinc and tellurium [54]. The formation of this superstructure is driven by a slight displacement of the palladium atoms from the face centers of the filled unit cells in response to the presence of the M atoms in the central interstitial sites. When these displacements are large enough, it is no longer possible to have M atoms in adjacent unit cells, and the ordered phase emerges. This corresponds with an effective unit cell that can be described by shifting the origin to (0.5, 0.5, 0.5) and placing each M atom at the shared corner of eight simple $CePd_3$ unit cells.

It is interesting to note that certain elements such as aluminum, gallium, and germanium have been reported to have both continuous solubility for $0 < x < 0.125$ *and* form the ordered phase for $x = 0.125$. This can most likely be explained by differences in the heat treatment conditions applied to the samples in the different studies. Those that reported the formation of the ordered phase were working with samples that were annealed for approximately three weeks at 900°C [53, 54, 56], while those that reported continuous solubility did not provide details regarding any heat treatments applied to the samples after arc melting, which suggests that no annealing was performed [55, 97].

It is also worth noting that although some M elements may be present in both the disordered and ordered phases, certain other M elements such as boron and silicon do not appear to order regardless of any heat treatment applied [54]. Thus a range of structural ordering behavior can be observed as a function of the identity of the M element as well as the processing conditions used to prepare the material. Given the important effects that such structural ordering can have on transport properties, variations in composition and processing of CePd_3M_x are both important to consider.

The lattice thermal conductivity may be particularly sensitive to the formation of these ordered phases. If the interstitial atoms are no longer randomly dispersed, their presence in the structure may simply introduce additional coherent vibration modes. This suggests that the ordered phases are not likely to display the same thermal conductivity reduction that would be expected in disordered materials.

This ordering is also likely to have an important impact on the electronic structure of the material, and limited studies of the thermoelectric properties of some ordered $\mathrm{Ce}_8\mathrm{Pd}_{24}M$ samples reveal trends consistent with this idea. Although decreases in the Seebeck coefficient and increases in the electrical resistivity are observed in these materials that are similar to those reported by Lackner for disordered boron-filled samples [42], these effects appear to have at least some dependence on the nominal size of the M elements. This suggests that within the ordered phases, the extent to which the palladium atoms are displaced from the unit cell faces can be correlated with changes in the electronic properties [54].

Based on these reports, there are clearly many complex relationships among the size of the unit cell, the cerium valence, and the properties of these filler atoms. There does not appear to be a consensus, however, regarding what mechanisms are ultimately driving the changes observed in the electronic, magnetic, and structural properties. For example, some reports exist suggesting that these changes are driven entirely by chemical pressure and therefore depend primarily on the size of the filler elements, while others suggest that factors such as the electron count of M may be equally or more important than the atomic radii [44, 54, 96].

The current study has thus been motivated by the effectiveness of interstitial site filling for lowering the thermal conductivity of $CePd_3$ in conjunction with the ambiguity surrounding how these filler atoms affect the electronic transport properties. The following is an attempt to untangle some of these complex relationships.

5.2 Experimental methods

Samples of $CePd_3M_x$ (M = Na, Mg, Ca, B, Al, Si, Ga, Ge, In, Sn, Te; $0 < x < 0.25$) were prepared through the standard arc melting procedure described above. Some additional processing steps were necessary for M elements with high vapor pressures and/or low boiling points, such as sodium, magnesium, calcium, and tellurium.

For samples containing these volatile elements, initial attempts were made to synthesize binary M-Pd precursors in order to facilitate stoichiometry control during arc melting. The basic requirement of any solid state precursor is that the volatile element be present in a ratio greater than or equal to its concentration in the final compound. It is also desirable for the precursor to be a line compound that melts congruently in order to ensure stoichiometry control during intermediate processing steps. Although precursor compounds with higher melting points tend to be more stable when arc melted, they are also generally more difficult to form through solid state reactions at low temperatures. The optimal reaction temperature is thus determined by the properties of the precursor phase as well as the volatile element, which can vary with the absolute pressure inside of the reaction chamber.

No stable binary phases exist between palladium and the Group I elements [98]. Synthesis of the binary compounds of palladium and Group II elements was generally difficult to control, as there are a relatively large number of possible binary phases close in stoichiometry, and the alkali earth elements have a strong tendency to react with quartz and other types of reaction vessels [99, 100].

Instead of using this precursor approach, samples containing sodium, magnesium, and calcium were successfully synthesized by simply re-melting pieces of pre-made $CePd_3$ on top of pieces of the filler element inside the arc melter. Although mass losses as a result of this process were relatively small, and although the transport properties of these samples deviate substantially from the control sample in ways consistent with the successful substitution of the M elements into the interstitial site, significant vaporization during melting may have occurred in some or all of the samples produced this way.

The M-Pd binary precursor approach was successful in the preparation of samples containing tellurium. Te_7Pd_{20} samples were prepared by combining pure tellurium and palladium in the appropriate ratio in an evacuated quartz ampoule, which was then heated above the melting point of the desired phase. This was combined with additional palladium and cerium pieces and arc melted in the standard way to produce the desired stoichiometry. Overall mass losses in the arc melter were less than 1%, suggesting that this precursor approach is effective for the implementation of tellurium into the interstitial site.

An attempt was also made to synthesize samples containing sulfur in hopes of introducing an electron acceptor into the interstitial site. To do so, PdS powder was purchased commercially (Sigma Aldrich), sealed in an evacuated quartz ampoule, then melted and recrystallized in order to produce larger pieces suitable for arc melting. Although mass losses from this process were less than 1%, the resulting XRD patterns showed what appear to be a combination of Ce_2S_3, $CePd_5$, and $CePd_{3+x}$. The presence of these impurity phases is only subtly apparent in the XRD patterns and becomes more prominent as the sulfur content is increased.

Additional compositions were also attempted with M = Sr, Ba, and Ag for $x = 0.05$, but the resulting ingots appeared to have obvious impurity phases coating their surfaces. In addition to this apparent phase separation, XRD and transport property analysis of the interior portions of these ingots closely resembled the behavior expected of unmodified $\mathrm{CePd_3}$. Thus it appears that these M elements are not easily incorporated into the interstitial site through this synthesis approach, if they can be at all. One interesting consequence of this is that although $\mathrm{CePd_3}$ can reportedly tolerate non-stoichiometry variations from approximately 74.6 at.% palladium to 76.2 at.% palladium (corresponding with compositions of $\mathrm{CePd_{2.94}}$ to $\mathrm{CePd_{3.27}}$) [101], and although silver has been repeatedly shown to substitute successfully into the palladium site in $\mathrm{CePd_{3-x}Ag_x}$ [43, 89], stoichiometric $\mathrm{CePd_3}$ appears to completely reject excess silver. This suggests that the defect mechanism(s) that enable the structure to tolerate such a wide range of Ce:Pd ratios do not arise from an extension of the palladium sublattice and introduction of cerium vacancies, but instead likely correspond with Pd_{Ce} anti-site defects that are not energetically favorable when silver is involved.

5.3 Results and Discussion

5.3.1 Structural Properties

Two distinct trends emerged in the XRD patterns obtained for the $\mathrm{CePd_3}M_x$ samples. The first of these trends is in relation to the onset of the ordered phase. A gradual shift in the lattice parameter was observed for all M elements from rows two through four of the periodic table, as seen in the XRD patterns obtained for a representative series of samples included in Figure 5.1. This behavior suggests that these elements are all continuously soluble into the interstitial site, consistent with the trends reported for samples containing aluminum, gallium, and germanium that were not annealed [55, 97]. The patterns for sulfur filled

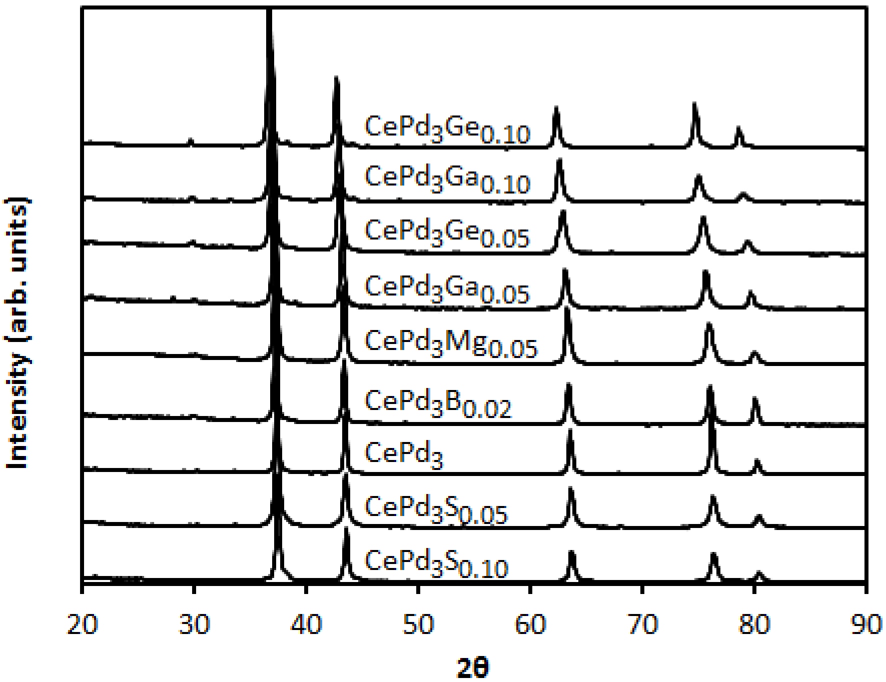

Figure 5.1: XRD plots for a representative series of $CePd_3M_x$ with M from rows two to four of the periodic table. The gradual shift in lattice parameter suggests a continuous solubility of these M into the structure.

samples have been included as well, with the subtle impurity peak at ~38° visible in the $CePd_3S_{0.10}$ sample.

In contrast to this trend, Figure 5.2 shows XRD patterns collected for samples containing M elements from row five of the periodic table. No reports exist of gradual solubility for these M elements. The results in Figure 5.2 are consistent with this idea, as they appear to show a mixture of two Cu_3Au-type phases with slightly different lattice parameters. The locations of the first sets of peaks are consistent with the spacings expected for the respective $Ce_8Pd_{24}M$ superstructures, while the second set matches the original locations of the $CePd_3$ pattern. The lack of any substantial shift in the $CePd_3$ peaks suggests that there is essentially no solubility of these M elements into the central interstitial site except through the formation of the ordered phase, which appears to form immediately from the melt with no additional

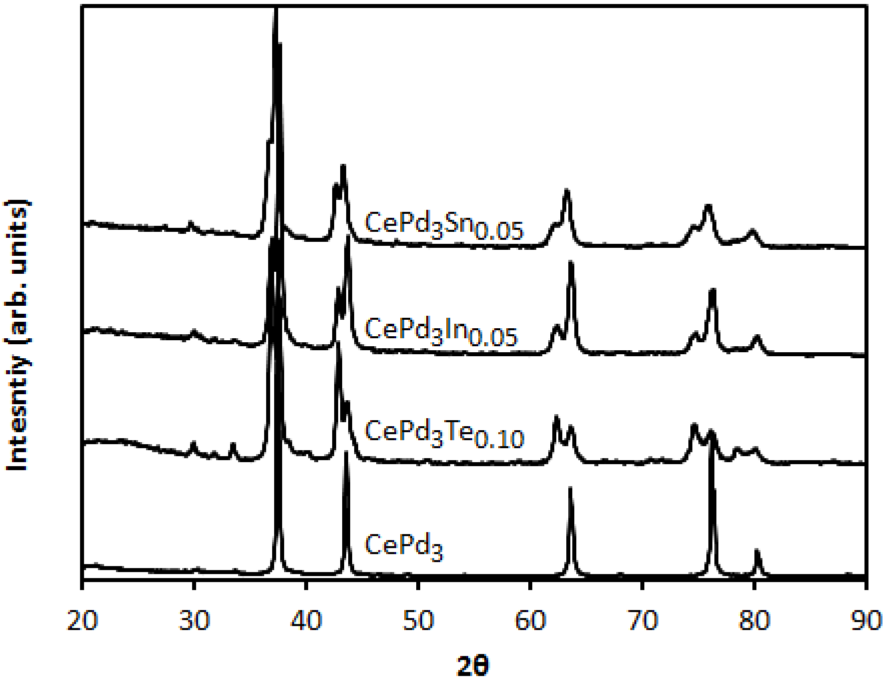

Figure 5.2: Some XRD plots for the $CePd_3M_x$ series for M from row five of the periodic table. The split peaks indicate a mixture of $CePd_3$ and $Ce_8Pd_{24}M$ phases.

heat treatment required.

Careful examination of the XRD patterns in Figure 5.1 reveals what appear to be small superlattice reflections in the samples containing gallium and germanium between $30 < 2\theta < 50$. These minor peaks appear to grow in relative intensity from the $x = 0.05$ to $x = 0.10$ samples for both gallium and germanium. The presence of these peaks, combined with the reported effects of annealing on similar samples, suggests that the palladium atoms are only slightly displaced from their nominal position on the face centers of the unit cell in these compounds. This displacement appears to be sufficiently small that it is still possible to place the filler atoms randomly throughout the structure, and ordering is not strictly necessary to accommodate their presence in the lattice. Although it appears that the solubility of these atoms can thus be described as continuous, the subtle perturbation they introduce to the structure may have a non-negligible effect on the electronic and/or thermal properties beyond what occurs as a result of purely randomly distributed defects such as boron and silicon, especially as the composition approaches $x = 0.125$.

The second trend that emerges in the structural properties is unique to the M elements from rows two through four of the periodic table. The large variety of M elements included in this study allows for a direct comparison of the CePd_3M_x lattice parameters with the properties of the M elements, which in turn allows for a clarification regarding the origin of the unit cell expansion in these compounds

To determine if the expansion of the unit cell is dependent at all on the negative chemical pressure of the M atoms in the interstitial site, Figure 5.3 has been included to show the refined lattice parameters for these samples as a function of the nominal atomic radii of the M elements. No apparent trend is visible in the data; if anything, the lattice parameter appears to decrease as the nominal size of the M atoms becomes larger.

This suggests that the unit cell expansion is electronic in origin. Based on this idea, it is useful then to define the "effective valence" V_{eff} of the interstitial site, which describes the average number of valence electrons per unit cell introduced by the M atoms. This parameter is defined as

$$V_{eff} = (x)(N_V), \tag{5.1}$$

where x is the filling fraction and N_V is the number of valence electrons of M. Figure 5.4 shows the lattice parameter data plotted as a function V_{eff}.

A linear trend can be seen in the data, as indicated by the fit line included in the plot. This establishes a clear correlation between the size of the unit cell and the electronic properties of the filler atoms.

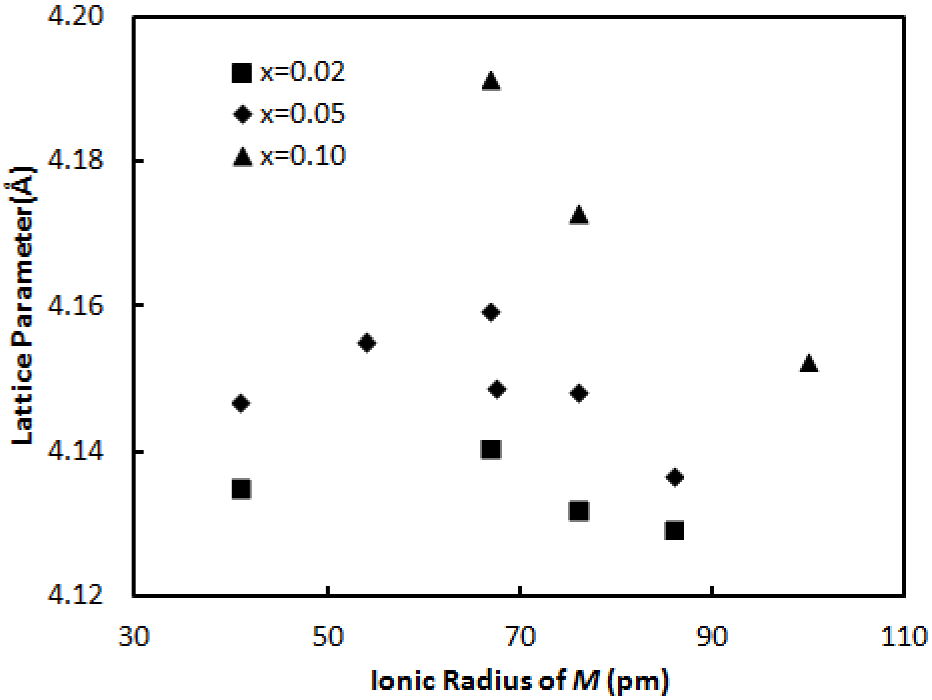

Figure 5.3: Lattice parameters of CePd_3M_x as a function of nominal M ionic radii. No clear correlation can be seen between these two variables.

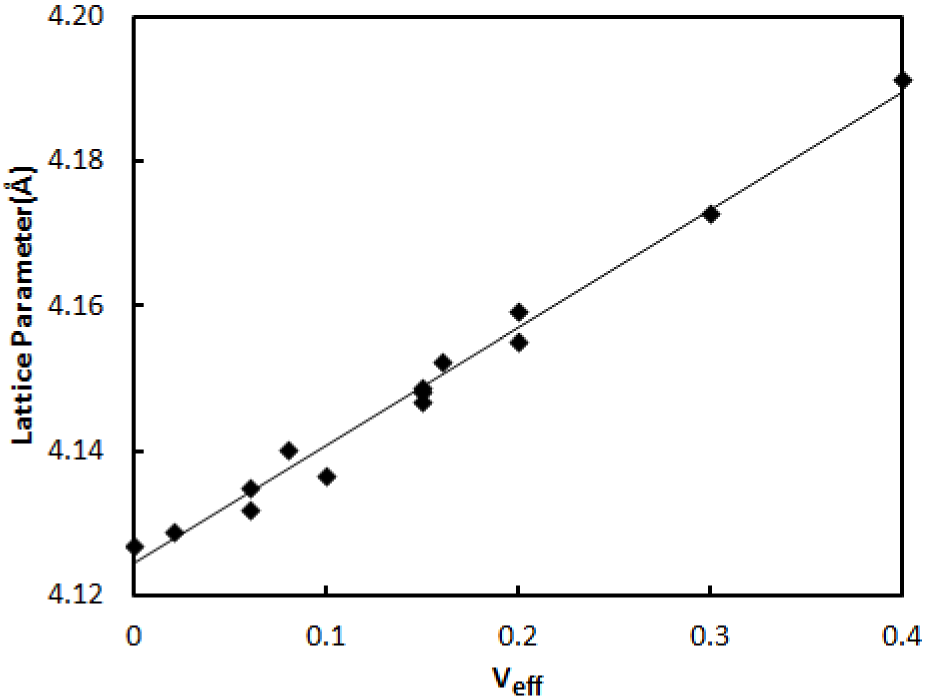

Figure 5.4: Lattice parameters of CePd_3M_x as a function of V_{eff}. These variables appear to be linearly dependent to first order.

5.3.2 Electronic Properties

Figure 5.5 shows the electrical resistivity of a representative group of samples normalized to their values at 350 K. A small amount of variation was observed in the absolute magnitude of ρ at 350 K among these samples, although they all fell within a relatively narrow range from approximately 0.9 $\mu\Omega$-m to 1.3 $\mu\Omega$-m. These changes in the absolute magnitude are necessarily related to variations in the coefficients of Equation 1.11. It is difficult to explicitly determine these parameters, however, as there is no clearly dominant mechanism contributing to the overall behavior. For example, the residual resistivity of $CePd_3$ has been shown to vary by over an order of magnitude from 0.14 $\mu\Omega$-m up to 2.9 $\mu\Omega$-m among samples with only slight variations in their nominal stoichiometry [102]. Thus the changes seen here may simply be attributable to variations in the Ce:Pd ratio. Regardless of this, the variations in magnitude are relatively small, and as such there does not appear to be any useful way of controlling the transport properties through these considerations.

It is possible, however, to determine systematic trends in the temperature dependence of ρ by comparing the trend in Figure 5.5 to the behavior reported for samples partially filled with boron [42, 46], silicon [45], aluminum [55, 97], gallium [55], and germanium [55] where only x was varied. In those reports, the peak in the resistivity is seen to simultaneously increase in magnitude and shift to lower temperatures, indicating a drop in T_K. For high enough filling levels, the Kondo term vanishes and $\rho(T)$ is dominated by the linear temperature dependence common for metals. This latter behavior can be seen for $CePd_3B_{0.25}$ in Figure 5.5.

It is difficult to determine the location of the resistivity peaks for these samples due to the limited temperature range over which these data were collected. A qualitative description

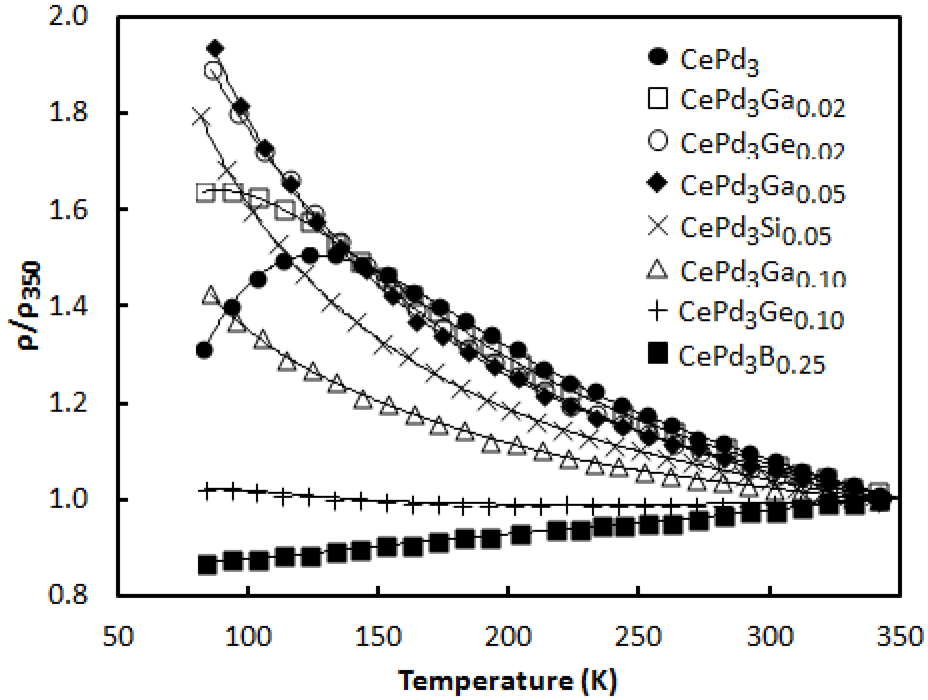

Figure 5.5: Normalized electrical resistivity of representative samples from the $CePd_3M_x$ series.

of the temperature dependence can still be used to show that these samples follow the same overall trends as those in the literature, in that the resistivity peak shifts to lower temperatures before it eventually saturates, decreases in magnitude, and approaches linear behavior. The novelty of the current work lies in the demonstration that these changes in $\rho(T)$ are can be generally described as functions of V_{eff}, regardless of the chemical identity of the specific filler atom. This trend is in agreement with the changes in the lattice parameter seen in Figure 5.4.

Figure 5.6 shows $\alpha(T)$ for a representative series of samples filled with various p-block elements. The identities of the specific filler elements have been removed to emphasize the primary dependence of the results on V_{eff} only. The temperature variation is approximately linear for all of the samples with a slope that decreases gradually as V_{eff} is increased. The magnitude of the Seebeck coefficient systematically decreases until eventually becoming *n*-

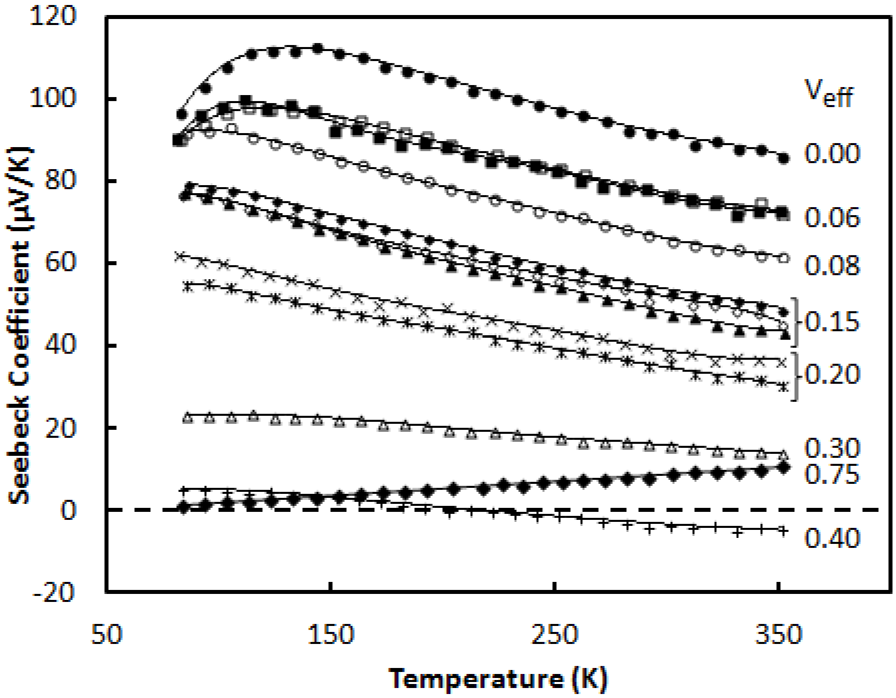

Figure 5.6: Seebeck coefficient of representative samples from the CePd$_3M_x$ series. Solid lines are a guide for the eye.

type for $V_{eff} = 0.4$ and $T > 200$ K.

A substantial change in $\alpha(T)$ is seen in the sample with $V_{eff} = 0.75$. In this sample, the Seebeck coefficient is small, positive, and has a linear temperature dependence over the entire range examined. This behavior indicates a complete collapse of the IV state and is similar to that previously reported for samples with $V_{eff} \geq 0.6$ [42, 45, 46]. For smaller values of x, however, a nearly linear variation in α at 295 K occurs as a function of V_{eff}. Figure 5.7 has been included to demonstrate this trend.

5.3.3 Thermal Properties

Consistent with the trends reported for CePd$_3$B$_x$ [42], a substantial decrease on the order of 50% was observed in the lattice thermal conductivity of these partially filled samples. Figure

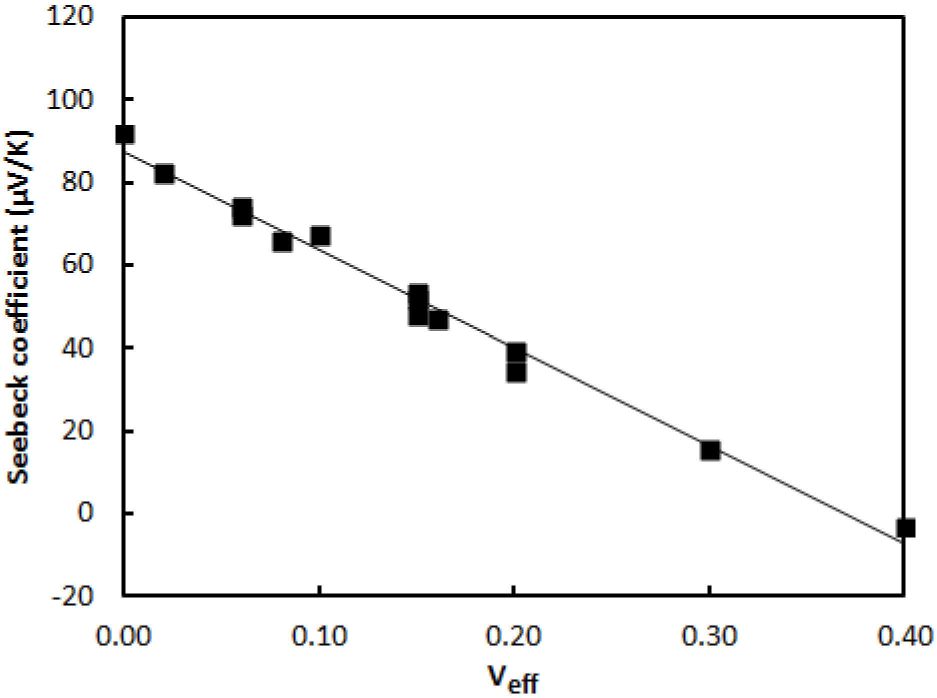

Figure 5.7: Seebeck coefficient at 295 K versus V_{eff} for representative samples from the CePd$_3M_x$ series. Solid line is a linear fit to the data.

5.8 has been included to show a cross section of κ_l values for various samples at 100 K. The values have been plotted as a function of the atomic mass of the corresponding filler element and grouped by the filling level x.

Two trends are apparent in the data. The first is that for fixed x, κ_l decreases as the mass of M is increased up to the saturation point of approximately 30 amu, above which no further reduction in κ_l is observed. The second trend is that for fixed M mass, κ_l decreases as x is increased up to 0.05, above which a similar saturation effect is observed.

The two dominant parameters that emerge for reducing the thermal conductivity are thus the filling fraction and the mass of M. Additional parameters such as lattice strain and the onset of ordering may also have an effect on κ_l, but the data in Figure 5.8 suggest that these effects have a relatively insignificant impact on the overall lattice dynamics of these materials.

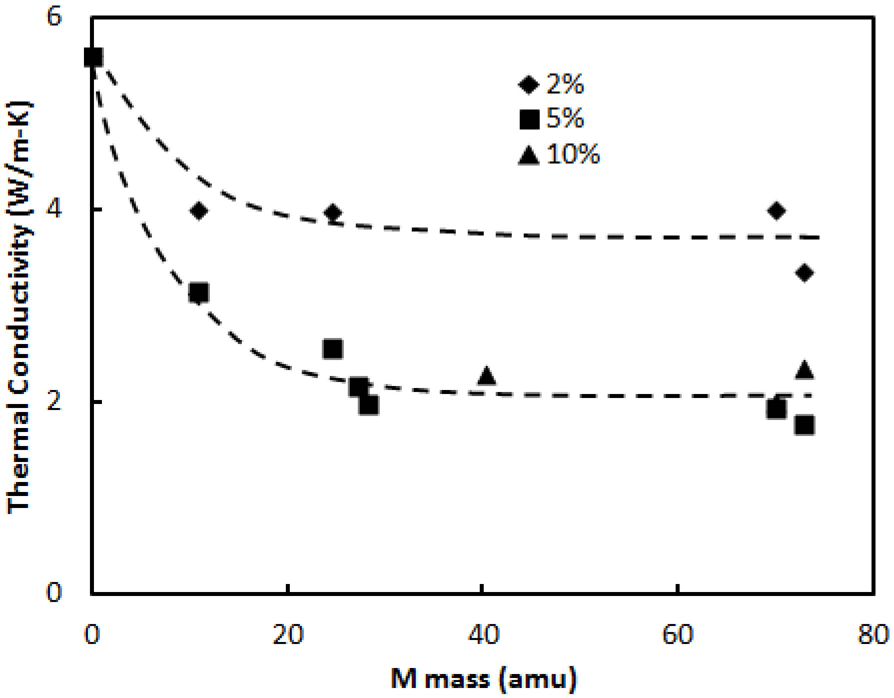

Figure 5.8: Lattice thermal conductivity at 100K of representative samples from the $\mathrm{CePd_3}M_x$ series. A saturation in the thermal conductivity reduction is observed as a function of M atomic weight as well as the filling fraction x.

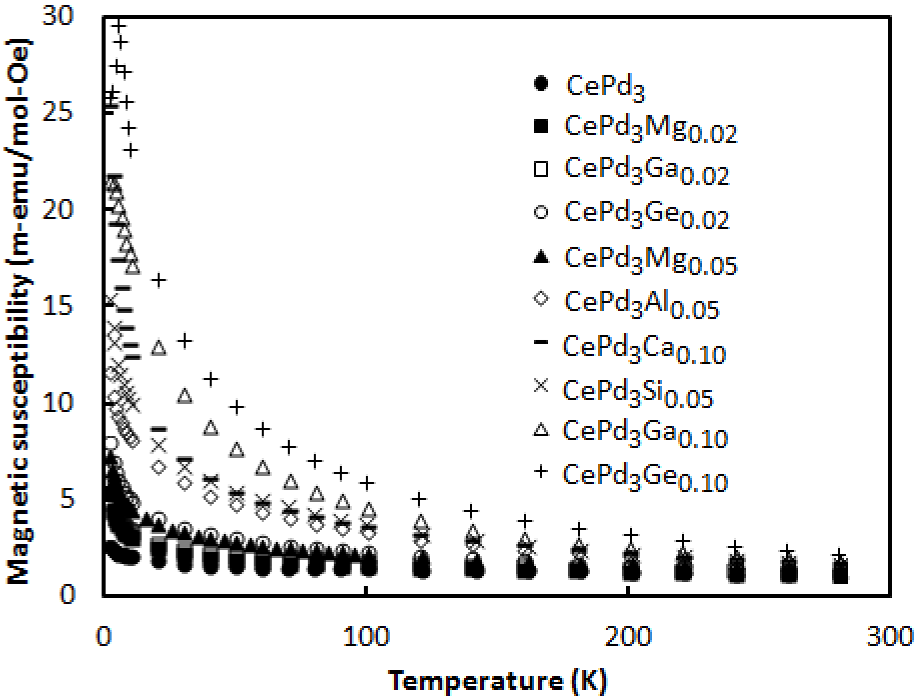

Figure 5.9: Magnetic susceptibility of representative samples from the CePd_3M_x series.

5.3.4 Magnetic Properties

The temperature dependence of the magnetic susceptibility for several samples in this series has been plotted in Figure 5.9. The changes observed in these data are again qualitatively similar to the changes seen for samples filled with boron [42, 46], silicon [45], aluminum [55, 97], gallium [55], and germanium [55] where only x was varied. The increasing magnitude at low temperatures that occurs as V_{eff} is increased indicates a shift toward trivalent cerium in these materials.

The magnitude of C extracted from plots of χ versus $1/T$ (200 K $\leq T \leq$ 300 K) have been included in Figure 5.10. An approximately linear relationship is observed between these parameters, again linking the electronic properties of the M atoms to the overall properties of the material.

The Hall coefficient of the $\mathrm{CePd}_3\mathrm{Ga}_x$ series was also measured. The results of these

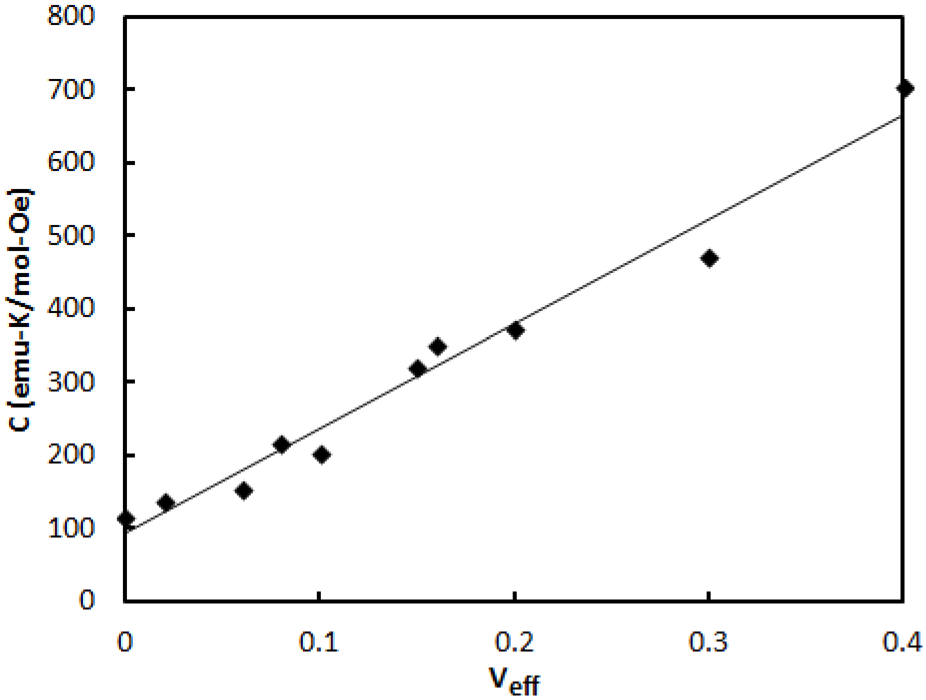

Figure 5.10: Curie constant versus V_{eff} for representative samples from the CePd$_3M_x$ series. Solid line is a linear fit to the data.

experiments are included in Figure 5.11 and show a general decrease in R_H as x is increased.

Although the Hall coefficient in CePd$_3$ is not necessarily a reliable or direct measure of the free carrier density, it is still possible to utilize R_H as a tool for probing changes in transport properties. Based on conventional interpretations of R_H, there are two simple explanations for why a decrease would be observed as the material is doped. If the material has only one type of carrier, then a decrease in $R_H = 1/ne$ is an indication that the carrier density has increased.

A decrease in R_H is also expected, however, for a system into which a second type of mobile carrier has been introduced. R_H for such a material can be expressed as

$$R_H = \frac{p\mu_h^2 - n\mu_e^2}{e(p\mu_h + n\mu_e)^2}, \tag{5.2}$$

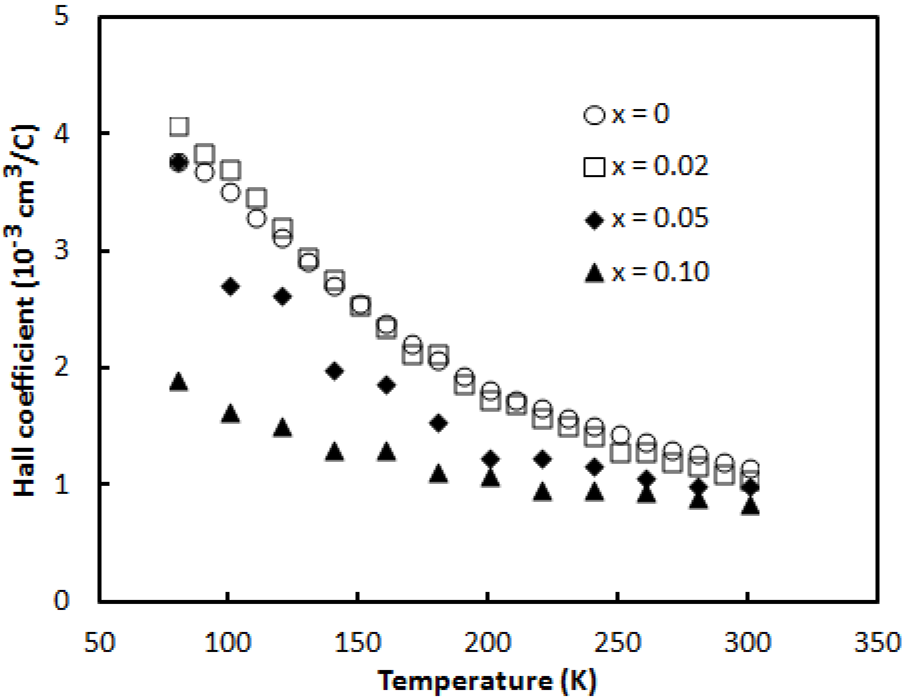

Figure 5.11: Hall coefficient for the CePd$_3$Ga$_x$ series.

where n (p) is the electron (hole) density and μ_e (μ_p) is the electron (hole) mobility [17].

This interpretation offers a more suitable explanation for the change in R_H apparent in Figure 5.11, as the addition of gallium into the structure increases the number of free electrons that act to compensate the intrinsic p-type behavior of the material. It is also useful then to consider the form of the electrical resistivity for a two carrier system, which can be expressed as [17]

$$\rho = \frac{1}{\sigma} = \frac{1}{e(p\mu_p + n\mu_n)}. \tag{5.3}$$

With these considerations in mind, the behavior of the CePd$_3$Ge$_{0.10}$ sample further supports the idea of charge carrier compensation in these materials. This sample displays a broad minimum in ρ in Figure 5.5 at approximately 200 K that coincides with a change in the sign of α visible in Figure 5.6, which together indicate that the majority carriers switch from holes to electrons at this temperature.

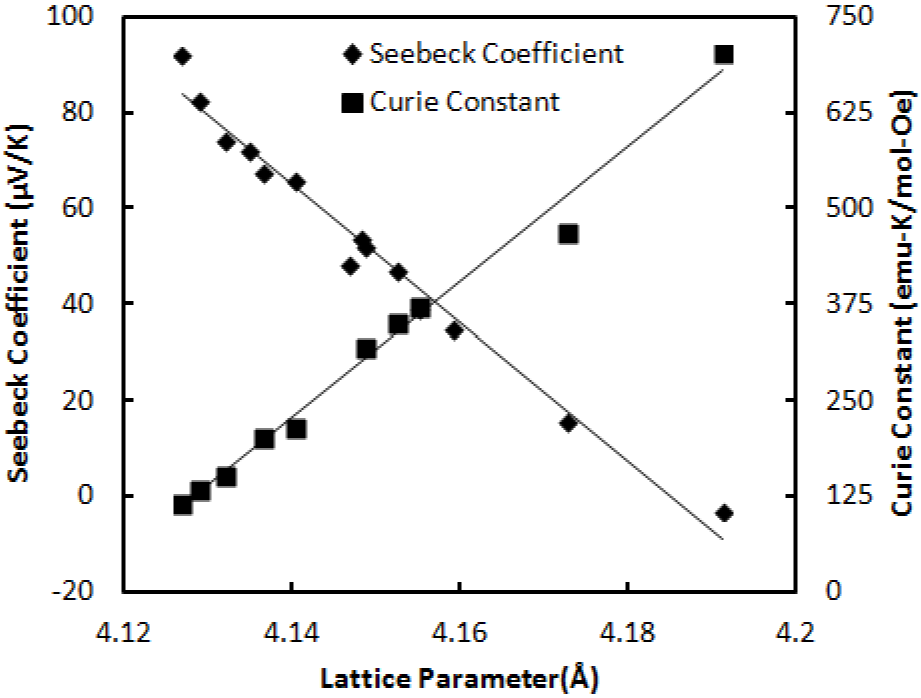

Figure 5.12: 295 K Seebeck coefficient (left ordinate) and high temperature Curie constant (right ordinate) of CePd$_3M_x$ vs 295 K lattice parameter. Solid lines are linear fits to the data.

5.3.5 General conclusions and ZT

The results of this study have demonstrated that the Seebeck coefficient, lattice parameter, and Curie constant of CePd$_3M_x$ can all be simultaneously tuned through adjusting a single parameter, V_{eff}. To emphasize this shared dependence, the room temperature Seebeck coefficient and high temperature (200 K $< T <$ 300 K) Curie constant have been plotted against the corresponding room temperature lattice parameter for these samples in Figure 5.12.

Furthermore, it has been demonstrated here that although both V_{eff} and κ_l are dependent on the filling fraction x, their separate dependence on the valence configuration of M and the mass of M, respectively, allow for these transport parameters to be decoupled to a limited extent. As a result, it is possible to achieve modest enhancements in ZT through

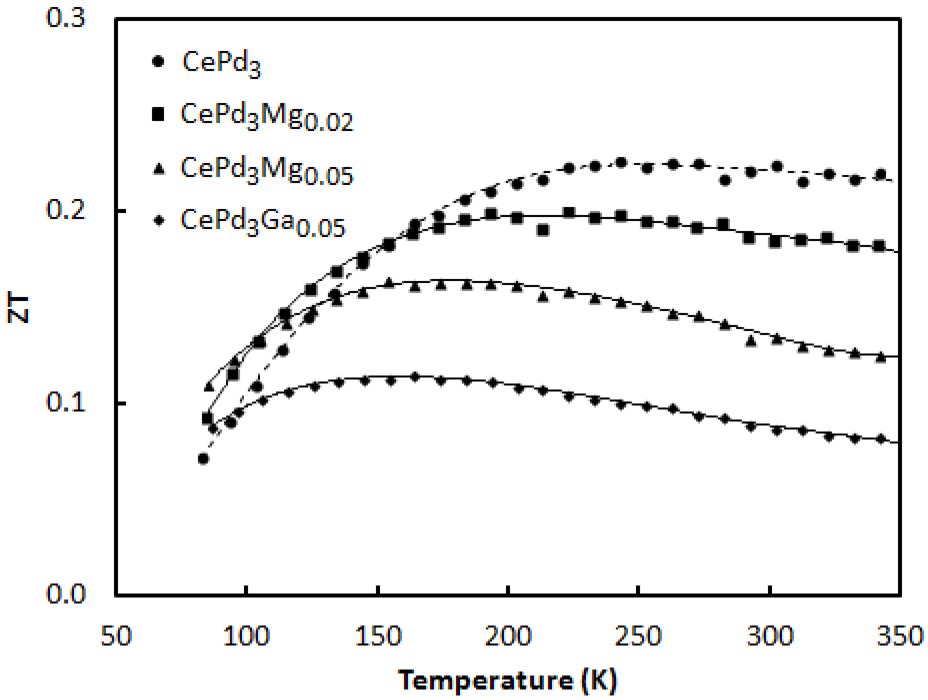

Figure 5.13: ZT of representative samples from the $CePd_3M_x$ series.

interstitial filling, as illustrated in Figure 5.13. The insertion of elements such as magnesium, which has a low number of valence electrons and a relatively large atomic mass, can be used to produce modest increases in ZT at 80 K from 0.07 in $CePd_3$ to 0.11 in $CePd_3Mg_{0.05}$.

Based on these overall results, it does not appear that interstitial site filling by itself will lead to any substantial improvements in the thermoelectric performance of the material. If a suitable mechanism can be found for increasing the hole concentration in the material, however, it may be possible to combine this mechanism with interstitial site filling in order to cancel out the competing doping effects, potentially leading to a material with a low lattice thermal conductivity but favorable electronic properties..

Chapter 6

Nanostructured $CePd_3$

6.1 Background and motivation

In the region $T < \Theta_D$, thermal conductivity tends to be dominated by longer wavelength phonons with relatively long mean free paths that are scattered primarily by grain boundaries [18]. Nanostructuring is therefore often an especially effective thermal conductivity reduction strategy at cryogenic temperatures. Since $\Theta_D = 292$ K for $CePd_3$ [73], reducing the grain size of the material should be an effective way to decrease κ_l below room temperature.

Two previous reports exist concerning nanostructured $CePd_3$ that suggest nanostructuring may also alter the electronic properties of the material. The first is a series of spectroscopic and diffraction experiments performed by Lin, et al. on 5 nm – 10 nm particles created through laser ablation [103]. Two primary results emerged from the data included in that report. The first is from the magnetic susceptibility of the nanoparticles, in which a systematic increase in the low temperature susceptibility is observed as the particle size is reduced. This increase is one of the signatures of a valence shift in the cerium atoms towards the 3+ state, and Lin, et al. estimate this change to correlate with approximately 25% of the cerium atoms in the trivalent configuration. In contrast to this, they also report x-ray absorption data that show a shift in the average valence of the cerium atoms toward the 4+ configuration. These results together strongly suggest that size effects have important consequences for the cerium valence state in nano-scale $CePd_3$ particles.

The second report is a study of magnetization, nuclear magnetic resonance (NMR), and computational analysis of 30 nm, 60 nm, and 150 nm $CePd_3$ particles created through high speed ball milling in toluene. These samples also show systematic increases in the magnetic susceptibility, in addition to a change in the NMR Knight shift that indicates an increase in the average $4f$ occupancy as the particle size is reduced. The authors of this study caution that defects and/or surface oxidation introduced by mechanical grain size reduction techniques may be at least partially responsible for the observed changes, but overall their results appear consistent with the idea that particle size reduction can have a direct impact on the IV state [104].

From a broader perspective, several reports exist describing the impact of surface effects on the valence state of rare earth elements and compounds that further support this idea. One example is that of samarium metal, for which angle resolved x-ray photoelectron spectroscopy (ARXPS) experiments have shown that a relatively large concentration of Sm^{2+} ions are found at the sample surface, while the bulk consists of predominantly Sm^{3+} [105, 106]. These ARXPS results are supported by compelling calculations of surface energy differences between Sm^{2+} and Sm^{3+} ions that reveal the former to exist in a lower energy state when exposed at a surface [105]. The authors of these studies also acknowledge that the ARXPS observations may simply be a result of oxide or hydride formation, but either way, these studies support the idea that exposure at an interface may have important consequences for the valence state of rare earth elements in certain alloys and compounds.

The behavior of several other rare-earth compounds has been studied as a function of grain size. Size-induced changes in electronic and magnetic properties have been widely reported through various experimental techniques in $CeAl_2$ [107, 108, 109], Ce_3Al [107], Ce_3Al_{11} [107], $CePt_2$ [108, 110], Ce_2Pt_5 [108], $TbAl_2$ [111], $TbCu_2$ [111], $GdAl_2$ [111, 112],

$YbAl_3$ [113], $Ce(Ru_{0.4}Rh_{0.6})_2Si_2$ [114, 115], $CeRu_2Si_2$ [115], $CeAu_2Si_2$ [109], and $CePd_2Si_2$ [109]. The samples studied in these other works were produced through a variety of techniques including ball milling, laser ablation, and flash evaporation, demonstrating the apparent universality of the size-dependent trends regardless of the specific processing technique used to create the nanoparticles.

These considerations suggest that nanostructuring $CePd_3$ may introduce a new mechanism for tuning the cerium valence, in addition to substantially decreasing the lattice thermal conductivity. This combination has provided significant motivation for the work described in this chapter, which explores the transport properties of several series of bulk nanostructured $CePd_3$ samples. This study appears to be the first time that the bulk transport properties of a nanostructured correlated metal have been explored.

6.2 Experimental methods

Samples of $CePd_3$ were prepared through arc melting in the standard way described above. The resulting ingots were transferred into an argon-filled glove box then placed inside of a 65 mL stainless steel milling jar. Two stainless steel balls 0.5" in diameter and four stainless steel balls 0.25" in diameter were added to the jar, which was then sealed with paraffin tape and removed from the glove box. The samples were milled for various lengths of time in a SPEX 8000M vibratory mill, and the resulting powders were removed in air. No obvious signs of spontaneous or gradual oxidation were present during any of these steps.

These powders were sintered into pellets through Pulsed Electric Current Sintering (PECS) (also known as Spark Plasma Sintering, or SPS) by pressing them at 56 MPa of uniaxial pressure at 820°C for one hour. A one hour hold was initially selected in an attempt to regrow the grains and search for signs of contamination from the ball milling and PECS processes. Even after a one hour hold, however, examination of the samples through XRD and SEM indicated that the samples were composed of nano-scale grains. As such, the same processing conditions were selected for all subsequent experiments in order to maintain consistency.

6.3 Results and discussion

6.3.1 Structural and morphological properties

No shift was observed in the lattice parameter for any of the ball milled samples, as seen in the XRD patterns included in Figure 6.1. The patterns are consistent with the expected Cu_3Au-type structure. Significant broadening of the peaks is observed that increases with milling time, indicative of the presence of nano-scale features. The lack of a peak shift is consistent with the results of Ref. [103] but disagree with those of Ref. [104], in which a shift to lower angles was observed as the grain size was reduced. Although no obvious second phases are apparent, the substantial broadening of the peaks severely restricts the overall effectiveness of XRD for detecting any impurity phases.

The results of SEM and EDS analysis are consistent with the results of the XRD data. For reference, Figure 6.2 has been included to show a representative SEM micrograph of arc melted $CePd_3$ collected at a magnification of 1,300x. The scale bar represents 10 μm, and relatively large grains on the order of several microns are clearly visible in the image. Analysis of this sample at higher magnifications (not included) did not indicate any fine structure to these grains.

In contrast to this, Figure 6.3 and Figure 6.4 have been included to show representative

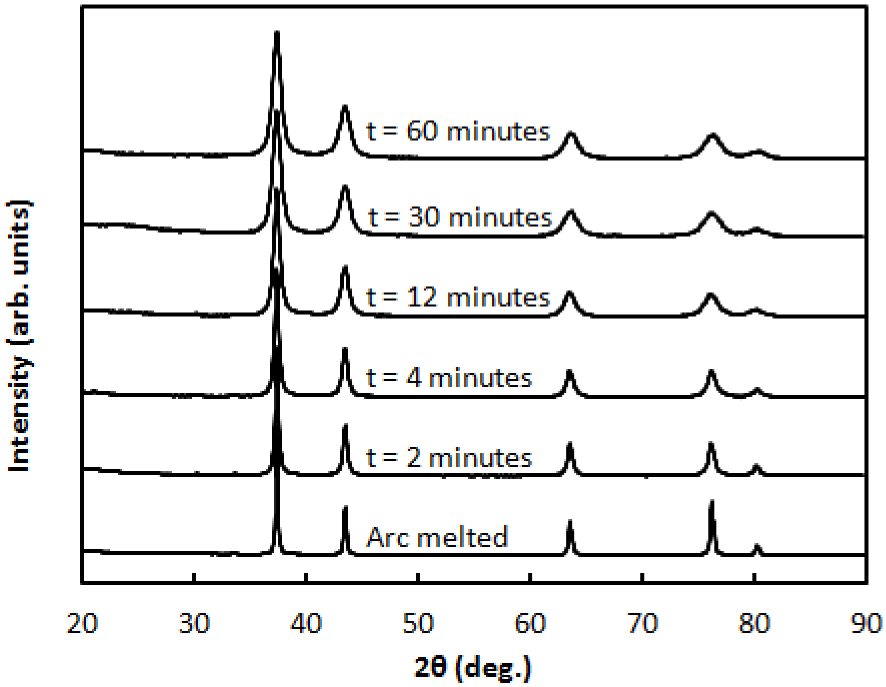

Figure 6.1: XRD patterns of $CePd_3$ samples ball milled for various times t, as labeled.

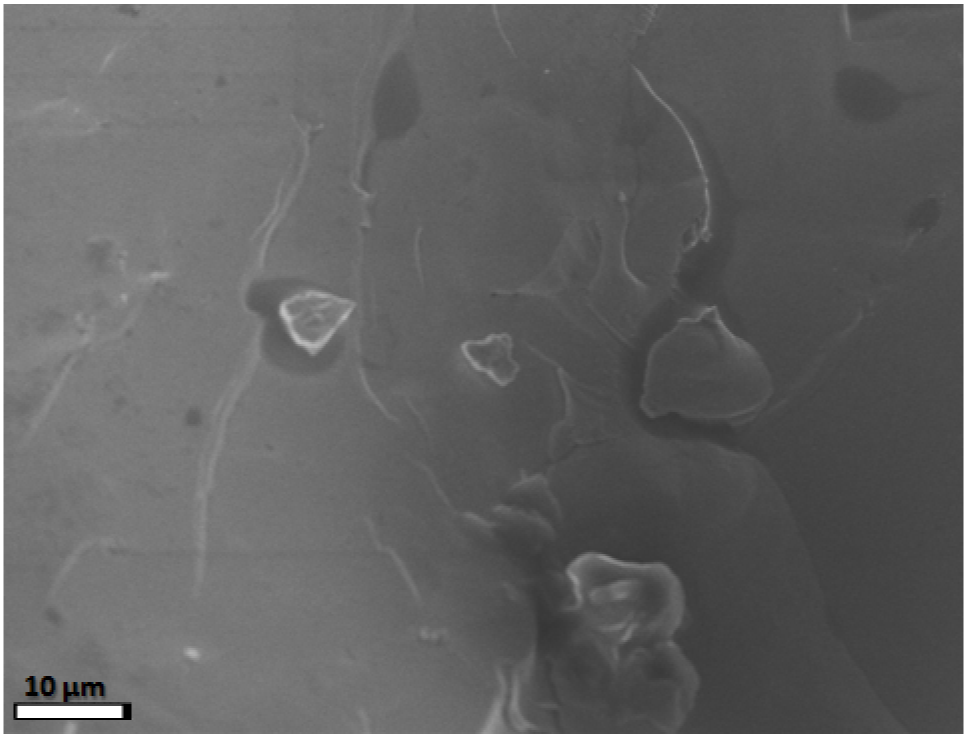

Figure 6.2: SEM micrograph of an arc melted $CePd_3$ control sample recorded at a magnification of 1,300x.

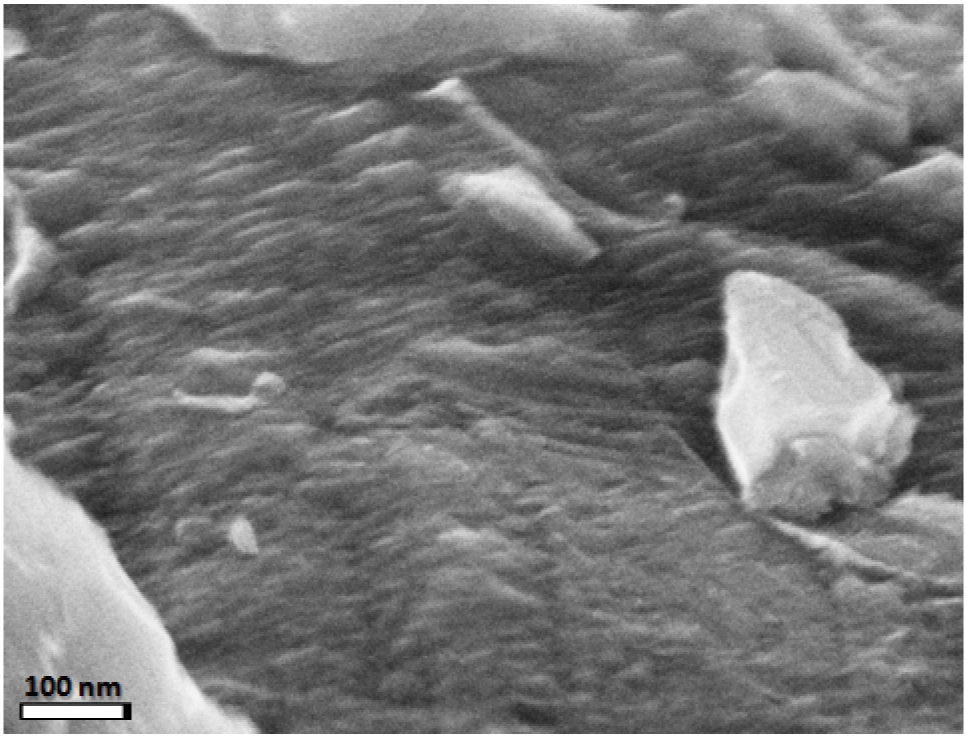

Figure 6.3: Contrast enhanced SEM micrograph magnified 100,000x of a $CePd_3$ sample ball milled for two minutes and sintered through PECS.

micrographs of the fracture surfaces of ball milled samples after sintering through PECS. The magnification of both images is 100,000x and the included scale bars represent 100 nm. Although relatively large agglomerates on the order of 100 nm and larger can be seen in both images, these agglomerates appear to be composed of smaller individual grains on the order of 10 nm to 20 nm. EDS analysis showed the presence of a small peak corresponding to oxygen in the samples, but a comparison of these spectra with those obtained for microstructured $CePd_3$ did not reveal any significant differences between the relative intensity of this peak as a function of processing conditions.

The size of these nano-scale grains was estimated by applying the Williamson Hall (W-H) method to the XRD patterns of the powders after ball milling. This analysis is based on the

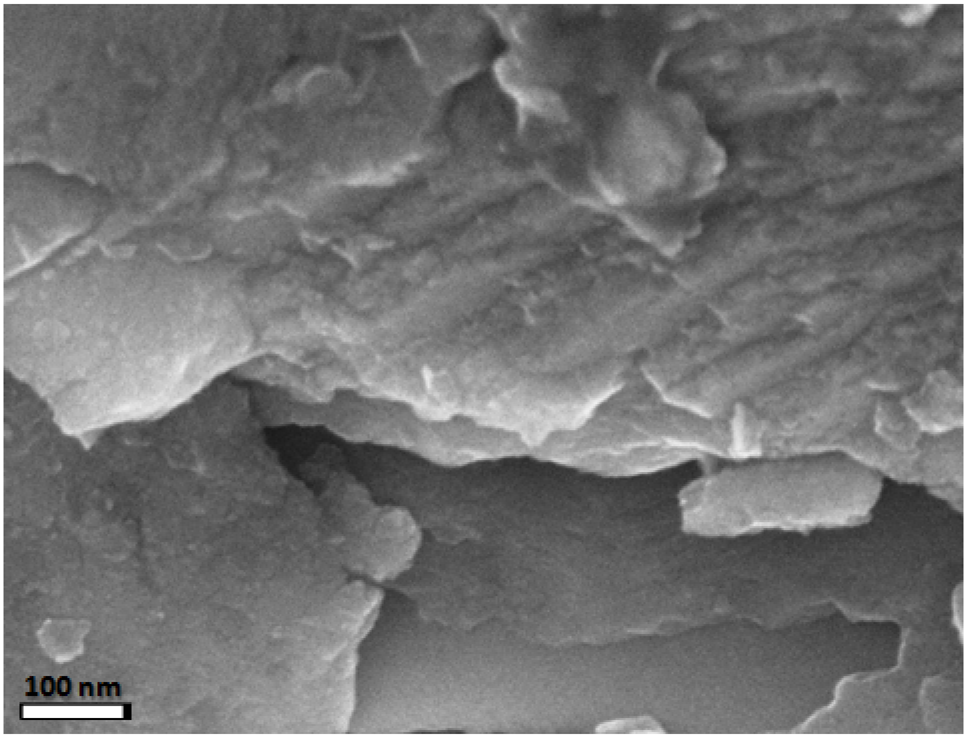

Figure 6.4: Contrast enhanced SEM micrograph magnified 100,000x of a $\mathrm{CePd_3}$ sample ball milled for 12 minutes and sintered through PECS.

relationship

$$\beta^2 = \beta_0^2 + \left(\frac{0.9\lambda}{D\cos\theta_B}\right)^2 + (4\epsilon\tan\theta_B)^2, \tag{6.1}$$

where β is the full width at half maximum (FWHM) of the XRD peak located at Bragg angle θ_B, β_0 is the contribution to the FWHM from instrument broadening, 0.9 is a geometric form factor, λ is the wavelength of radiation used in the experiment, D is the particle size, and ϵ is the strain [116].

This equation was used to analyze the patterns in Figure 6.1. The results of this analysis are included in Figure 6.5, where D and ϵ have been plotted as functions of the milling time. The estimated uncertainty in the calculations of D and ϵ are ± 2 nm and $\pm 0.05\%$, respectively. A saturation in both the grain size reduction and strain increase is observed as the milling time is increased. This effect is common for ball milled samples and results

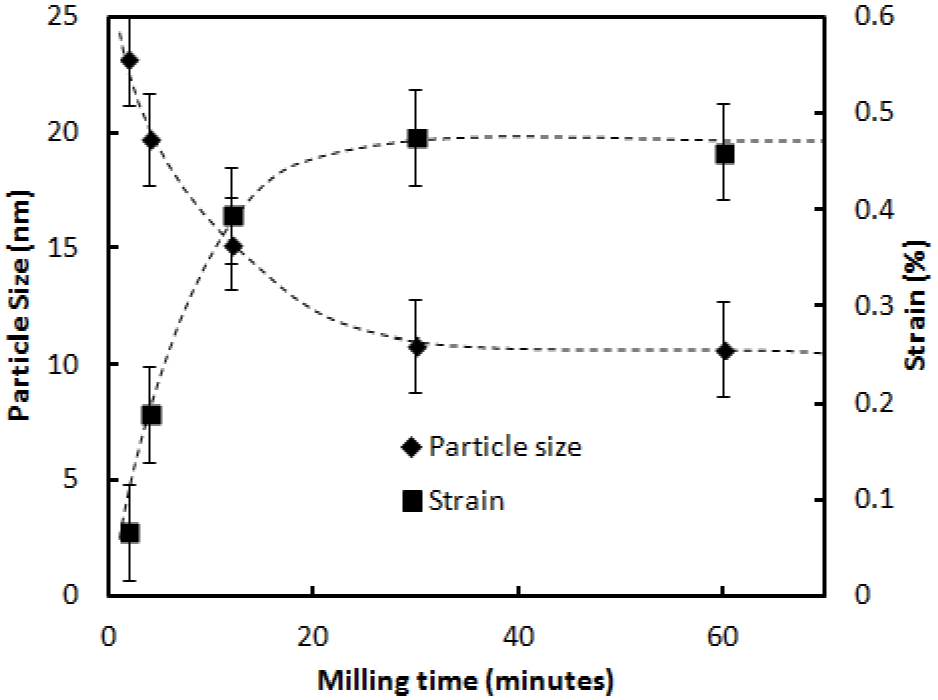

Figure 6.5: Particle size and strain of ball milled $CePd_3$ samples as determined by Williamson-Hall analysis (Equation 6.1). Dashed lines are a guide for the eye.

from a combination of the finite frequency and maximum kinetic energy of the collisions in the jar, combined with the mechanical properties of the samples and milling media. A slight decrease in the calculated strain is observed as the milling time is increased from 30 minutes to 60 minutes. This variation is within the estimated error of the calculation, but it may also be a real result of the rearrangement and annihilation of dislocations with increased milling time [117].

Although SEM analysis on the sintered pellets indicates the presence of nano-scale features that appear to be consistent with the results of Figure 6.5, this W-H analysis was performed on the powders directly after ball milling and not after sintering. This was done due to the presence of agglomerates in the sintered samples, which seem to limit the accuracy of the W-H method for determining the crystallite size. Thus the actual grain size

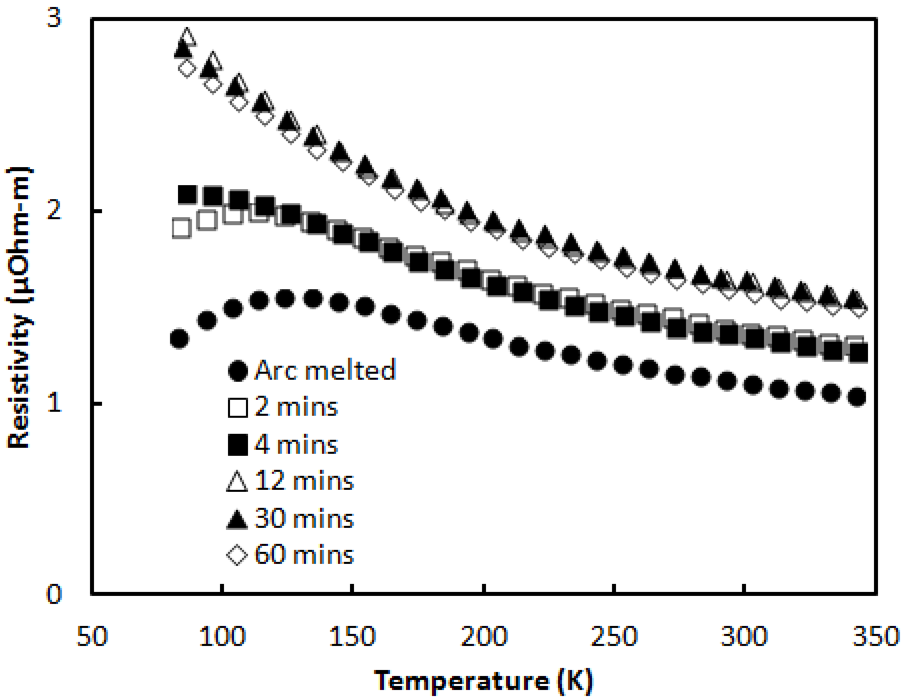

Figure 6.6: Electrical resistivity of nanostructured $CePd_3$.

and strain present in the sintered pellets used for transport property measurements may be slightly different from the values indicated in Figure 6.5, but these values can at least be used as a self consistent way of interpreting any changes observed in the thermoelectric properties.

6.3.2 Electronic properties

A general increase in the magnitude of the electrical resistivity of the ball milled samples can be seen in Figure 6.6. The changes in ρ appear to saturate in the samples milled for time $t \geq 12$ minutes, mimicking the saturation in the grain size reduction seen in Figure 6.5. A systematic change in the temperature dependence is also observed for $T < 150$ K, indicative of a change in the Kondo temperature T_K.

A monotonic decrease in the magnitude of the Seebeck coefficient as a function of milling

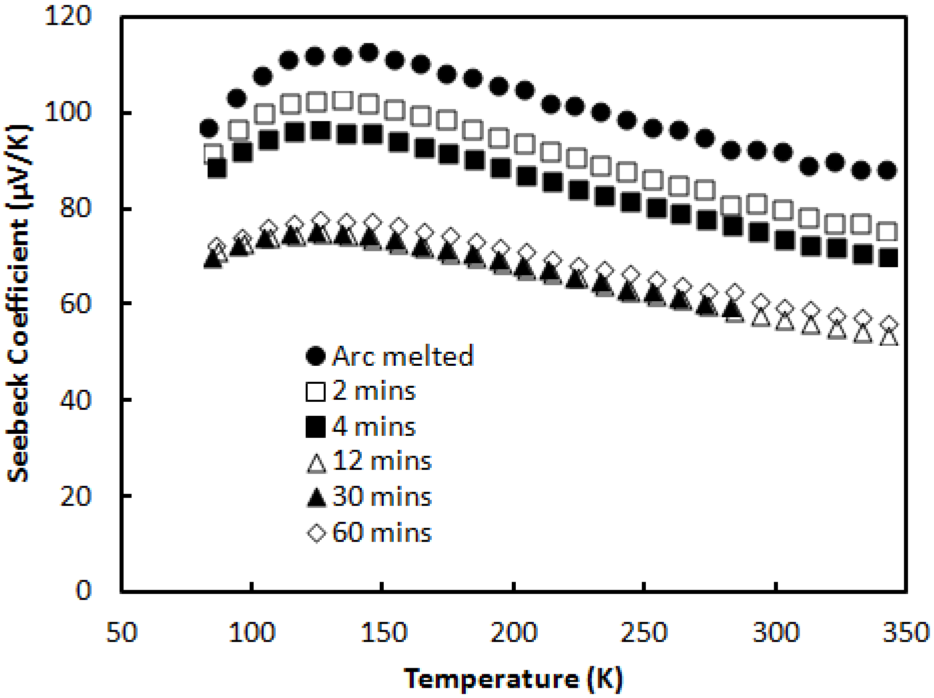

Figure 6.7: Seebeck coefficient of nanostructured $CePd_3$.

time is apparent in Figure 6.7. This reduction in the magnitude of α also appears to saturate in a fashion similar to the W-H results in Figure 6.5.

6.3.3 Thermal properties

The total and lattice thermal conductivity of the samples are included in Figure 6.8 and Figure 6.9, respectively. A reduction of $\sim$50% is achieved for the samples milled for $t \geq 12$ minutes, emphasizing the effectiveness of this approach in scattering phonons. In both of these plots, the same saturation effect is observed as a function of milling time, further supporting the notion that these changes are closely tied with the grain size reduction achieved as a result of ball milling.

Although this approach is particularly effective for reducing the absolute magnitude of the lattice thermal conductivity, it is important to also consider changes in the thermal

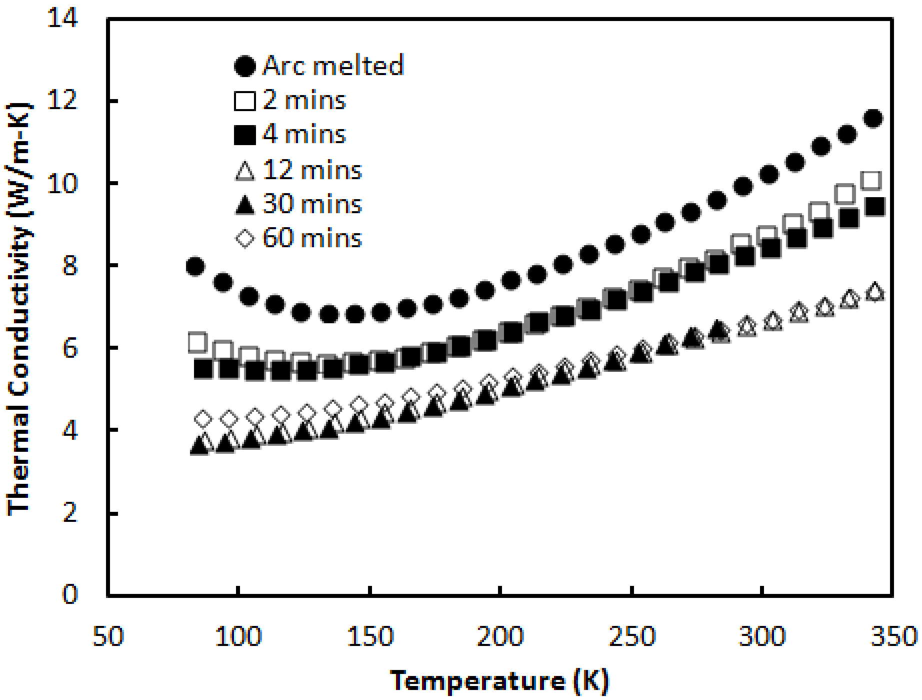

Figure 6.8: Total thermal conductivity of nanostructured $CePd_3$.

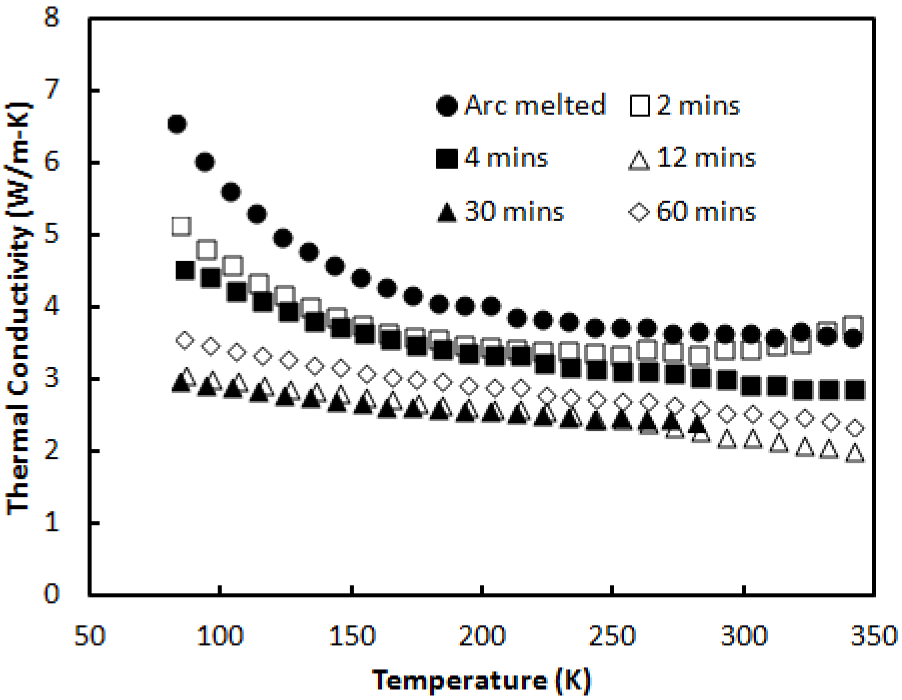

Figure 6.9: Lattice thermal conductivity of nanostructured $CePd_3$.

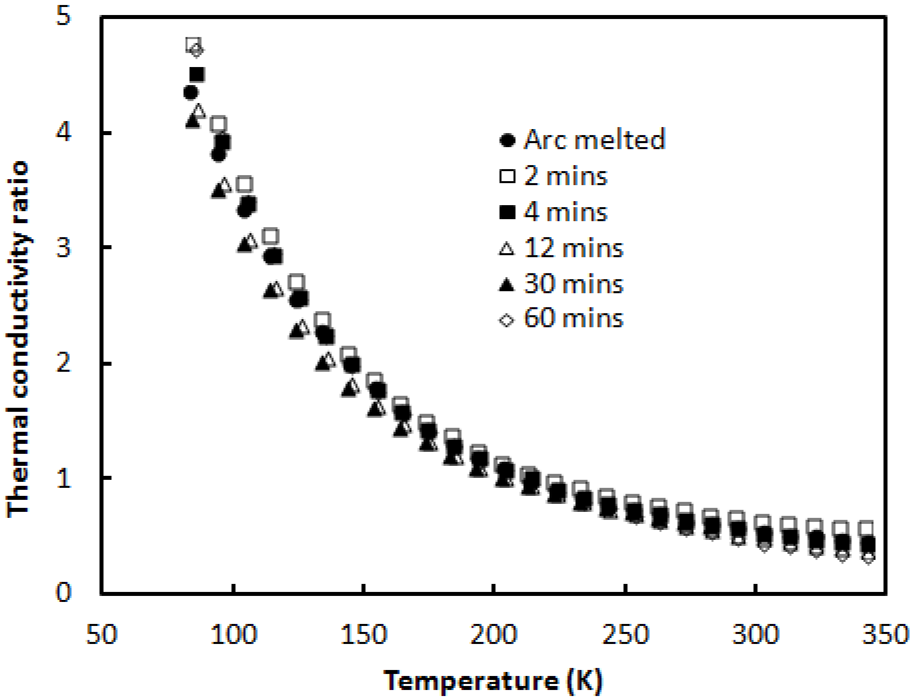

Figure 6.10: Thermal conductivity ratio of nanostructured $CePd_3$.

conductivity ratio κ'. The relatively large increase in ρ that occurs as the grain size is reduced results in a decrease in κ_e that closely mirrors the reduction in κ_l, resulting in no significant improvement in κ' for any of the nanostructured materials. These results are summarized in Figure 6.10.

6.3.4 Magnetic properties

Measurements of the Hall coefficient were performed on these samples in order to search for evidence of changes in the free carrier density. The results of these measurements are included in Figure 6.11. A monotonic reduction in R_H occurs as the milling time is increased, which suggests that the density of p-type carriers is systematically increasing as the grain size is reduced. These results are qualitatively different from those of the $CePd_3Ga_x$ samples described by Figure 5.11, which show a much larger decrease in R_H at low temperatures.

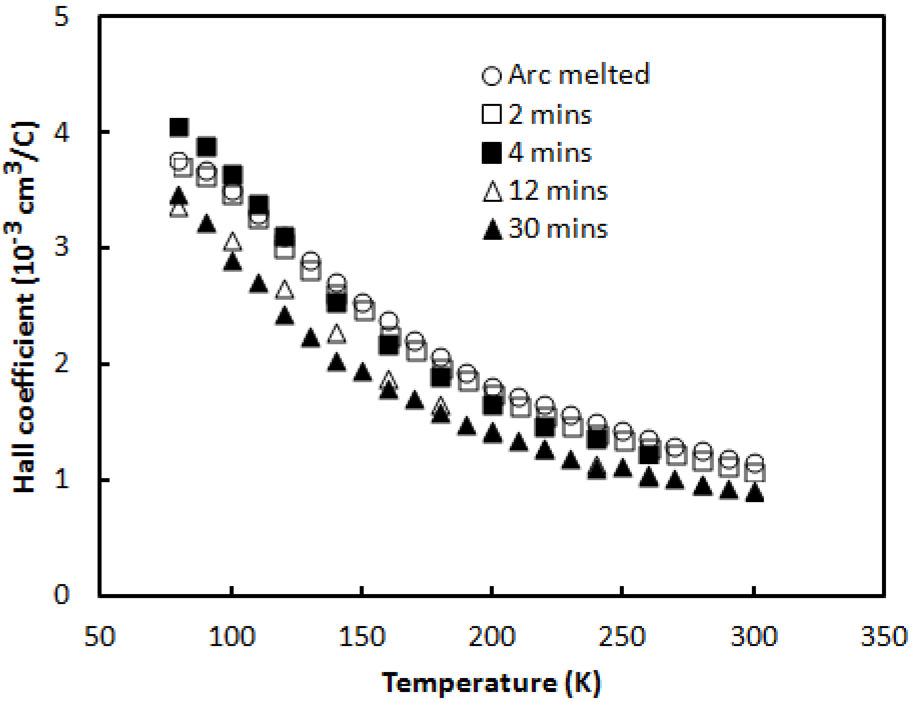

Figure 6.11: Hall coefficient of nanostructured $CePd_3$.

Thus although the magnitude of α and T_K appear to change in both of these series in similar ways, the mechanisms that drive these changes appear to be fundamentally different.

Since the ball milled samples do not appear to be chemically modified in any way, it is reasonable to assume that a one carrier model can be used to interpret the changes in R_H. From R_H and ρ it is possible to determine the Hall mobility μ through the relationship $\mu = 1/(\rho en) = R_H/\rho$. The results of this analysis are included in Figure 6.12 and show that a significant decrease in the Hall mobility of the carriers occurs as the grain size of the samples is reduced, likely a direct result of increased interfacial scattering.

This apparent change in the free carrier density is somewhat surprising, as no compositional modifications have been made, and contamination effects would not be expected to saturate with milling time. In order to help explain these changes within the context of grain size reduction effects, the following "size-doping" model is proposed.

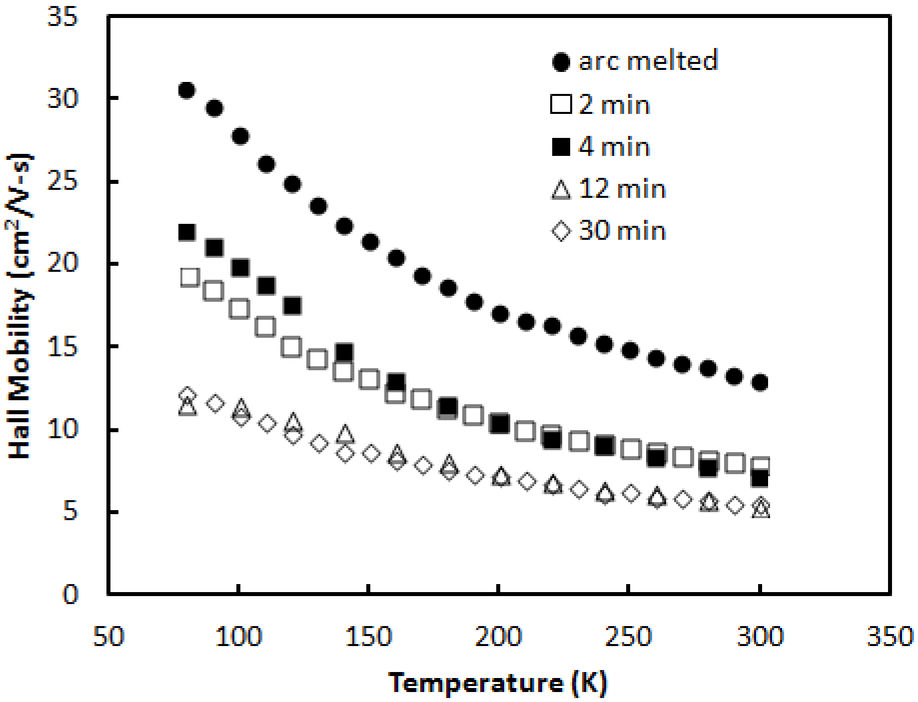

Figure 6.12: Hall mobility of nanostructured $CePd_3$.

6.4 “Size-doping” model

It is convenient to consider a ”size-doping” model to directly connect the observed grain size reduction with the corresponding changes in the transport properties. Inspired by the observed surface effects in other materials as described above [107], this model begins with the assumption that incomplete atomic coordination at the grain boundary collapses the IV effect and converts these $4f$ electron levels into highly localized states.

Filling these $4f$ levels at the surface requires some electrons to be pulled from the bulk. Since the average cerium valence in $CePd_3$ is approximately +3.45 at room temperature [58, 59], each unique unit cell exposed at the grain surface thus requires on average approximately 0.45 additional electrons to fill the cerium $4f$ shell. The effective hole concentration of the bulk should be expected to increase as a result of these electrons being pulled from the conduction band and localized at the surface.

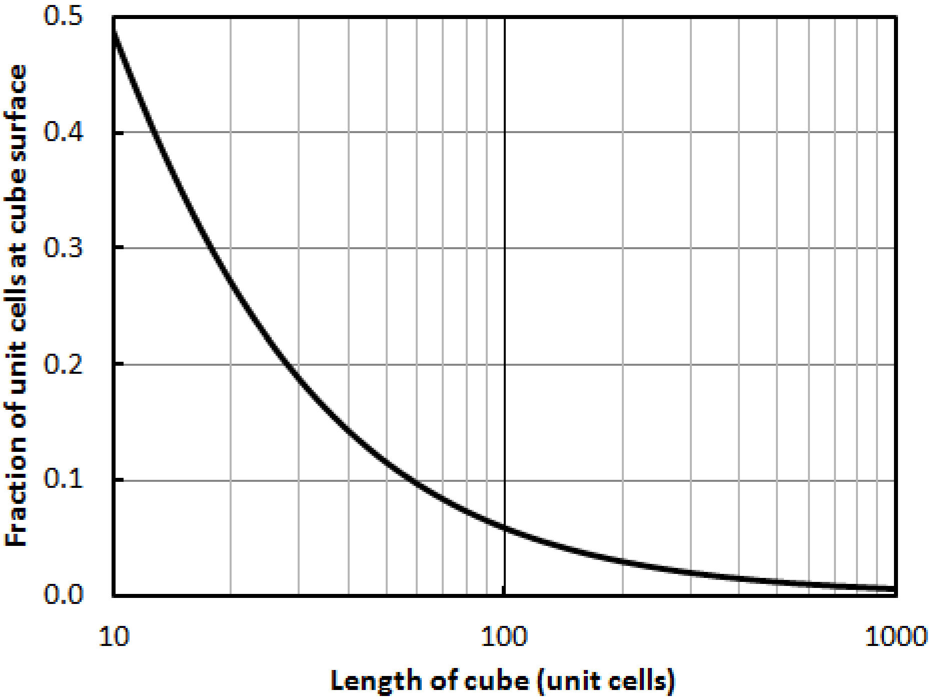

Figure 6.13: Simple geometric model for the fraction of unique unit cells at a cube surface.

A basic geometric argument can be invoked to estimate the proportion of unit cells at the surface of a nano-scale grain. Since $\mathrm{CePd_3}$ forms in a cubic structure, it is appropriate to consider a perfect cubic crystal composed of l cubic unit cells. The total number of unique unit cells N exposed at the surface of such a cube is equal to

$$N = l^3 - (l-2)^3. \tag{6.2}$$

The fraction of total unit cells in the material exposed at the surface is then given by

$$\frac{N}{l^3} = \frac{\left(l^3 - (l-2)^3\right)}{l^3} = 1 - \left(1 - \frac{2}{l}\right)^3. \tag{6.3}$$

A plot of N/l^3 versus l has been included in Figure 6.13 to demonstrate the significant change in surface area-to-volume ratio that occurs for a cubic crystal as the cube size is reduced.

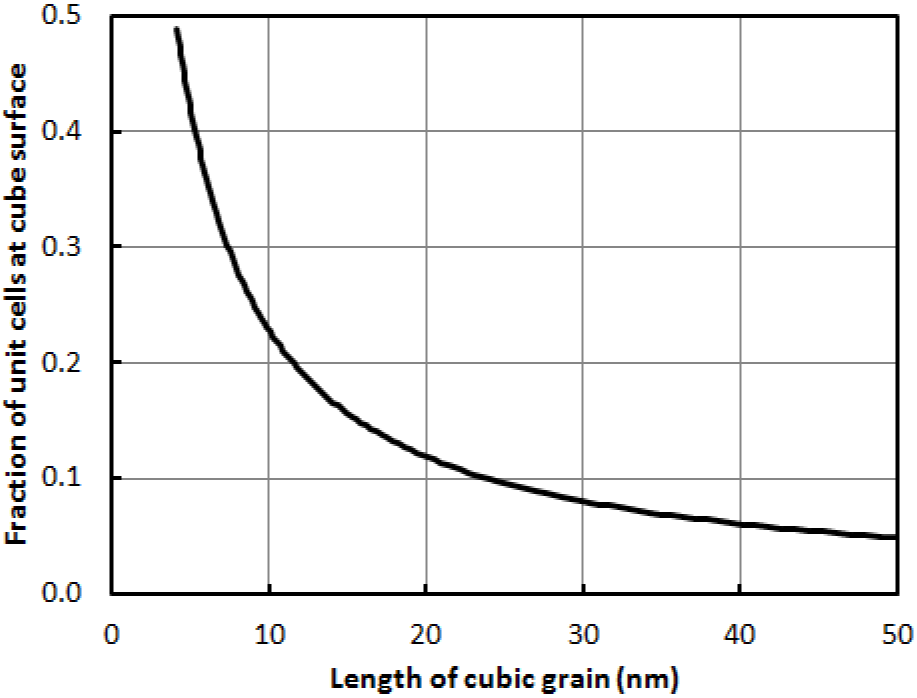

Figure 6.14: Estimated fraction of unique unit cells at the surface of a $CePd_3$ grain.

For a grain approximately 1,000 unit cells across, less than 1% of the cells are located at the surface. As the grain shrinks in size, however, more cells become exposed; about 6% of the cells are at the surface in a 100^3 cell cube, and nearly 50% are exposed for a cube 10 cells across. Thus surface effects may be negligible for grains composed of $1{,}000^3$ cells, but they may become significant in grains that are only tens or hundreds of unit cells in length.

This geometric model can be extended to a physical system by multiplying l by the lattice parameter of the material. The results of this analysis are included in Figure 6.14 for $CePd_3$. Based on the results of this simple analysis, 20 nm grains of $CePd_3$ will contain approximately 12% trivalent cerium, while this ratio nearly doubles to 23% for 10 nm grains.

This model agrees with Lin's study on laser ablated samples, which showed that approximately 25% of the cerium atoms in a 9 nm particle were in the 3+ configuration [103]. This falls precisely within the range of values expected based on the results of Figure 6.14.

In spite of this success, this model should be considered only a basic approximation of the expected behavior of the material, as real materials are made of grains with spanning a range of sizes that are often faceted and full of defects. This variation can make the actual surface area-to-volume ratio difficult to accurately predict and measure. The presence of point and line defects introduced through the milling process may also have a significant impact on the IV state [110]. Full consideration of these other possibilities would improve the accuracy and utility of this model for interpreting and predicting the behavior of the material.

6.4.1 Further study

Further grain size reduction may be possible through the use of different milling media, such as tungsten carbide instead of stainless steel. Other techniques for producing nanoparticles in sufficient quantities for powder processing, such as wet chemistry, may also be possible. It would be worthwhile to compare the results of such studies to the current work in order to examine the universality of these results, although the sensitivity of the $CePd_3$ system to even small amounts of chemical contamination may make isolation of size effects difficult.

More generally, the results of this study appear to support the idea that grain size reduction can alter the electronic properties of strongly correlated materials. Since correlated electron effects are central to the behavior of many interesting and useful materials, it may be possible to modulate these effects simply by reducing the grain size to the nano-scale, thus tailoring the materials' properties without modifying their composition or structure. Further study of this idea in other rare earth and transition metal compounds may yield interesting results in this regard.

Chapter 7

Universal trends and combined approaches

A careful comparison of the properties observed in the different series discussed above leads to additional insights regarding the apparently universal nature of some of these trends.

The first universal trend that emerges is in regards to the relationship among Seebeck coefficient, lattice parameter, and Curie constant in the CePd_3M_x and $\mathrm{CePd}_{3-x}\mathrm{Pt}_x$ series. In both cases it was observed that an approximately linear correlation exists among all three of these properties that results from their shared dependence on the average valence configuration of the cerium atoms. Extending this analysis further, it is also possible to compare the temperature dependence of the lattice parameter in stoichiometric CePd_3 with the Seebeck coefficient at the same temperatures [118]. The results of this combined analysis are included in Figure 7.1, and show that a very similar relationship appears to exist among all three properties in all three series.

This universality is surprising when considering the different mechanisms that dominate the behavior of each series. The properties of the CePd_3M_x system have a strong dependence on the "effective valence" of the interstitial site, indicating that the changes in this system are entirely electronic in origin. In $\mathrm{CePd}_{3-x}\mathrm{Pt}_x$, however, the observed changes appear to be predominantly a result of chemical pressure introduced by the slightly smaller platinum

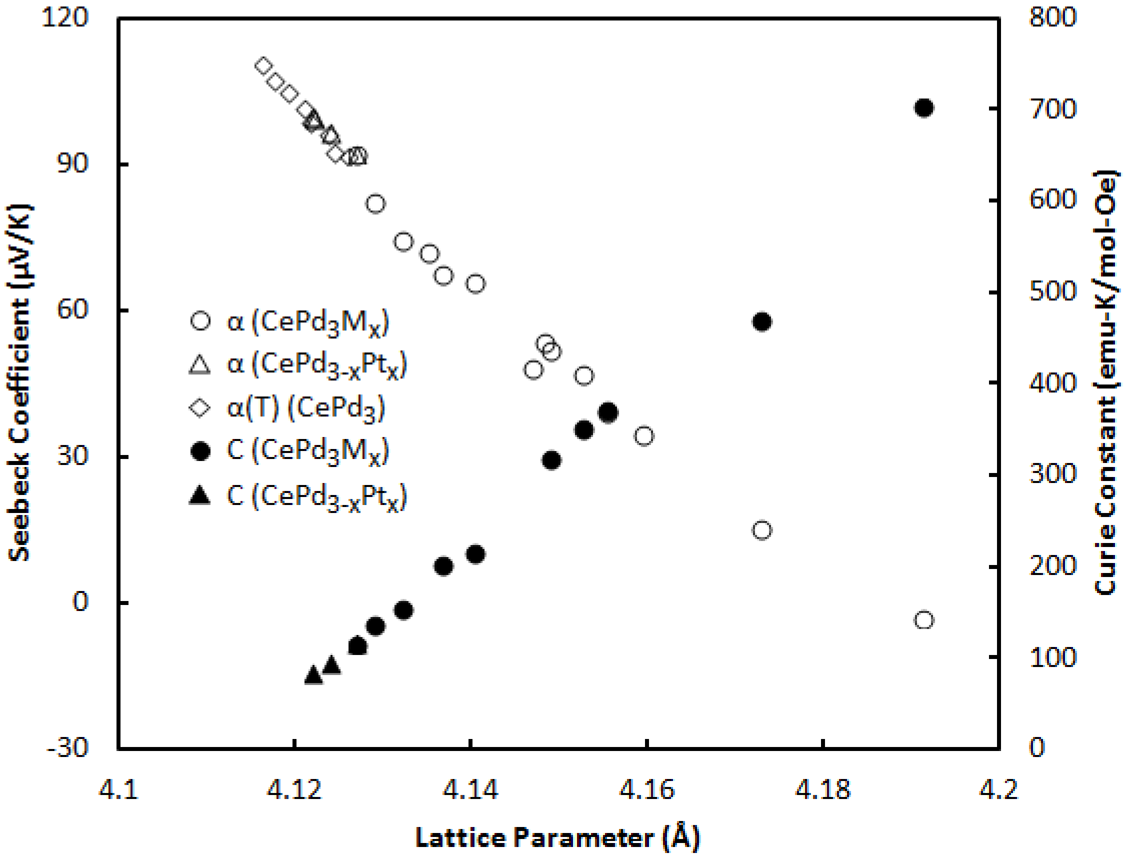

Figure 7.1: Seebeck coefficient (left ordinate) and Curie constant (right ordinate) as a function of lattice parameter for various $CePd_3$ series. Temperature dependent lattice parameter data are from [81].

atoms occupying the palladium sites. The extension of this trend to the temperature dependence of stoichiometric CePd_3 shows that similar behavior can be observed as a function of thermal expansion as well.

This type of broad perspective may be useful for determining additional ways of increasing ZT. Although each of the mechanisms discussed in the preceding chapters has on its own at best a limited effectiveness for improving the thermoelectric performance of the material, it may be possible to combine them together in such a way that the properties are improved beyond what each approach can achieve separately. This basic idea has been attempted before in studies inspired by the general correlation between the Seebeck coefficient and the lattice parameter of CePd_3 often observed as the material is modified in various ways, as seen in Figure 7.1. These efforts have typically focused on combining mechanisms that shift the lattice parameter in opposing directions, such that κ_l can be reduced while the lattice parameter (and thus α) may remain unchanged.

The first such attempt was reported by Ijiri and DiSalvo [83], who explored the effects of dual substitutions on the cerium site. In their study, they examined a series of samples where cerium was partially replaced in equal parts by large lanthanum and small yttrium atoms, as well as regular solid solutions of $\mathrm{Ce}_{1-x}\mathrm{Y}_x\mathrm{Pd}_3$ and $\mathrm{Ce}_{1-x}\mathrm{Nd}_x\mathrm{Pd}_3$. Their results very clearly indicated that even if the average interatomic spacing was held constant, the thermoelectric properties of the material were substantially changed in ways not expected based on the simple combination of Mattheissen and Nordheim-Gorter rules for solid solutions.

The neodymium substituted samples do follow the expected trends reasonably well up to approximately 40% doping. The incoherence of the cerium sublattice above this doping level appears to dramatically affect the properties of the material, which the authors suggest may be a result of the differences in the d and f levels of the two elements. This may also be correlated with a change in the spatial distribution of magnetic and non-magnetic atoms that alters the nature of the Kondo interaction.

The $\mathrm{Ce}_{1-x}(\mathrm{La}_{0.5}\mathrm{Y}_{0.5})_x\mathrm{Pd}_3$ samples showed even larger changes in the transport properties relative to those seen in $\mathrm{Ce}_{1-x}\mathrm{Nd}_x\mathrm{Pd}_3$, even though these samples also had a very similar average lattice parameter to CePd_3. This suggests that in addition to doping effects, local strains and distortions in the lattice can have significant effects on the IV state. Based on these results, it is not valid to assume that simply maintaining the average lattice parameter at a constant value is sufficient to maintain the desired thermoelectric properties as well [83].

The second attempt at combining approaches was reported by Lackner, et al. [43], who tried to balance the lattice parameter reduction of rhodium substitution with the corresponding expansion observed with boron filling and/or silver substitution. Although this approach did result in a Seebeck coefficient increase in some $\mathrm{Ce}(\mathrm{Pd}_{1-x}\mathrm{Rh}_x)_3\mathrm{B}_{0.05}$ samples relative to their singly modified parent compounds, none of these combinations resulted in ZT values above 0.2. The results of this study nonetheless serve as proof of principle that it may be possible to combine thermal conductivity reduction mechanisms together in such a way that the Seebeck coefficient can be at least partially restored to its original value, which may result in ZT values not otherwise attainable through each approach alone.

7.1 Nanostructured CePd_3M_x

7.1.1 Background and motivation

The combined results of the CePd_3M_x and nanostructured CePd_3 series described above indicate that these approaches may alter the material in opposite ways. In particular, it appears that partially filling the interstitial site adds electrons to the conduction band, while nanostructuring pulls electrons from the conduction band to fill the $4f$ shells of cerium atoms at the grain surfaces. This suggests that combining these approaches may result in a material with low lattice thermal conductivity and no overall change in the charge carrier density within the bulk of the grains.

If successful, the cancellation of these effects should be readily apparent in the Seebeck and Hall coefficients. Furthermore, the strong linear dependence of the lattice parameter on V_{eff} implies that a nanostructured sample partially filled with M atoms should exhibit a smaller lattice parameter shift compared to a sample of the same composition without nano-scale features if the doping effects do in fact cancel out.

This combination of approaches may not completely restore the electronic properties of the material to those of the unmodified compound, however, as a substantial fraction of unit cells containing metallic trivalent cerium should still be present at the grain boundaries. This may result in a mixture of behaviors expected for a composite of metallic $R\mathrm{Pd}_3$ and IV CePd_3. In order to explore these possibilities directly, several samples of nanostructured $\mathrm{CePd}_3\mathrm{Ga}_x$ were prepared and examined for this study.

7.1.2 Experimental methods

Samples of $\mathrm{CePd}_3\mathrm{Ga}_x$ ($0 < x < 0.05$) were synthesized by arc melting the constituent elements in the typical manner. Gallium was chosen as the filler element for these studies primarily due to its large mass and high boiling point, both of which enable easier stoichiometry control during arc melting. The arc melted samples were ball milled and subsequently sintered at 820°C under 56 MPa of uniaxial pressure. The milling and sintering times were varied in an attempt to study the effects of processing variations on the transport properties and phase purity of the material.

7.1.3 Results and discussion

Initial experiments were performed on a sample of $CePd_3Ga_{0.05}$ ball milled for 30 minutes and sintered at 820°C for one hour under 56 MPa of uniaxial pressure in a manner identical to the procedures followed for the original $CePd_3$ nanostructured series. The results of XRD experiments on this sample before ball milling showed a characteristic shift of the peaks to lower angles, indicating an expansion of the unit cell consistent with the general trend for all $CePd_3M_x$ samples. After ball milling, XRD peak broadening was observed that closely resembled that of the other ball milled $CePd_3$ samples. A slight shift in the location of the diffraction peaks back toward the positions expected for unmodified $CePd_3$ was also observed after milling. This shift became even more prominent after sintering, wherein the peaks appeared to almost completely return to the nominal positions. These initial results were consistent with the lattice parameter shift expected for a sample in which the two competing doping effects were balanced. Analysis of the transport properties of this sample revealed that the magnitude and temperature dependence of the Seebeck coefficient, electrical resistivity, and thermal conductivity were consistent with a mixture of behaviors seen separately in the ball milled and $CePd_3M_x$ series, further suggesting that dopant compensation had occurred.

SEM and EDS analysis was performed on this sample in order to more thoroughly examine its phase purity, and the results of this analysis are included in Figure 7.2. These images show that although the gallium appears to be well distributed throughout the entire sample, a large cluster can be seen in the circled area that corresponds with a decrease in cerium content within the same region. The shape of this gallium-rich region appears to match the general outline of the grains in that area. This apparent segregation of the gallium into a

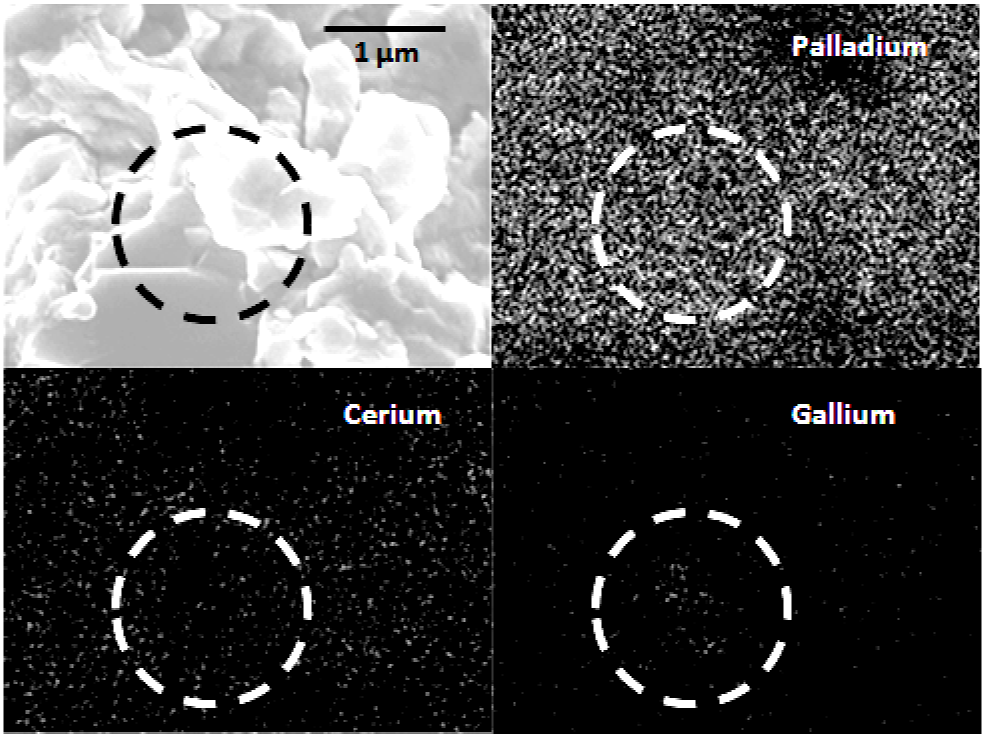

Figure 7.2: SEM and EDS results for $CePd_3Ga_{0.05}$ after ball milling and one hour of sintering through PECS. Dashed lines have been added to highlight the primary area of interest where segregation of gallium into an impurity phase is apparent in the elemental mapping results.

secondary phase suggests that only a fraction of the gallium initially added to the compound remained dissolved in the bulk after the mechanical nanostructuring process. The composition of this secondary phase was identified through EDS point and area spectra collected from the circled region in Figure 7.2 to be within the range $GaPd_{1.8}$ (64 at.% palladium) to $GaPd_{2.1}$ (67.7 at.% palladium). Analysis of the Ga-Pd binary phase diagram indicates that this phase is likely $GaPd_2$ [119].

The presence of this secondary phase indicated that the initial processing conditions were suboptimal. In order to explore whether this segregation occurred during ball milling, sintering, or both, another sample of $CePd_3Ga_{0.05}$ was synthesized and ball milled for 12 minutes instead of 30. As seen in Figure 7.3, XRD analysis of this sample shows an approximately identical shift in the lattice parameter between the two samples after milling, as indicated by

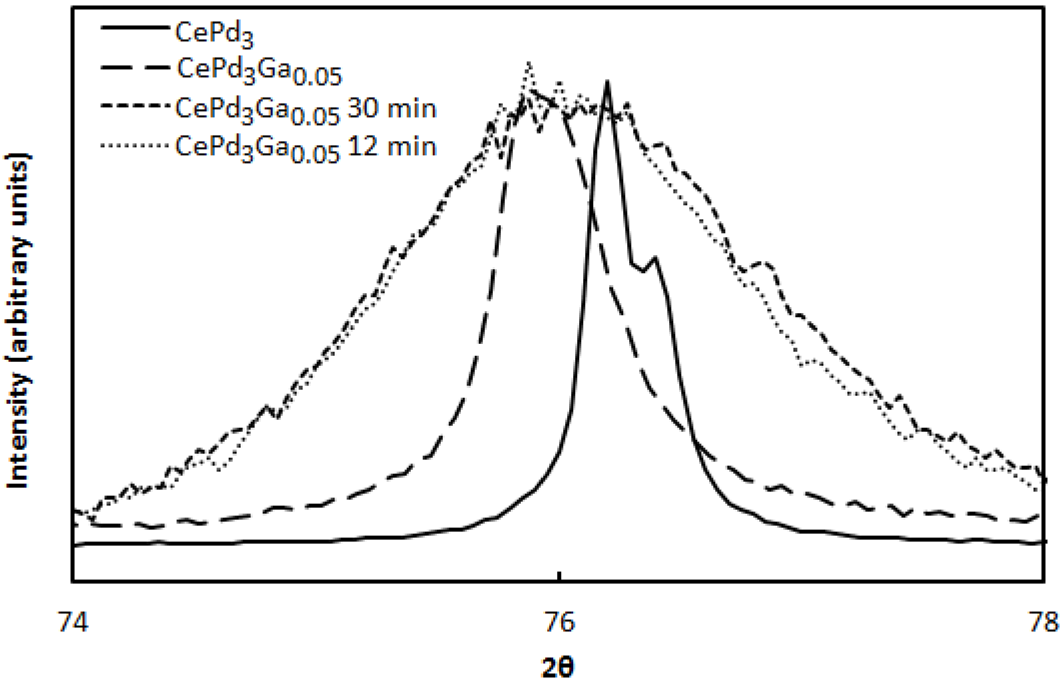

Figure 7.3: Location of normalized (311) peak in $CePd_3Ga_{0.05}$ after ball milling for various times. The peak shifts to lower angles after gallium is added to the interstitial site, but it begins to shift back toward its original position after ball milling.

the approximate overlap of the (311) diffraction peaks included in the figure. The positions of the original $CePd_3$ and $CePd_3Ga_{0.05}$ peaks have also been included for comparison, and the relative peak intensities have been scaled to emphasize the broadening that occurs as a result of ball milling.

The similarities in these patterns suggest that this shift arises primarily from dopant compensation and not from dopant segregation, as it does not appear to have any significant dependence on the milling time. The sample milled for 30 minutes has a slightly broader peak width and is shifted to a slightly higher angle, which can both be explained as likely arising from minor variations in the average grain size between the two samples.

A comparison was next made between samples sintered for one minute and one hour. These results can be seen in Figure 7.4, which shows the diffraction pattern of the (311)

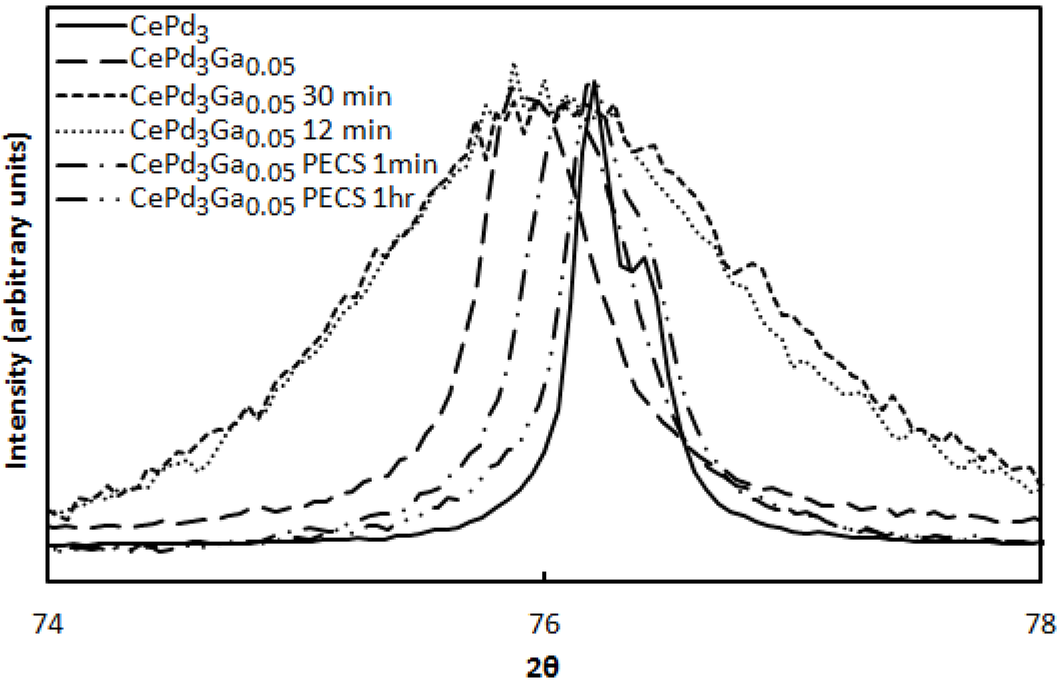

Figure 7.4: Location of normalized (311) peak in $CePd_3Ga_{0.05}$ after ball milling and PECS. While the peak shifts back almost to its original position in unmodified $CePd_3$ after one hour of sintering, only a small peak shift is observed in the sample sintered for one minute.

peak for these $CePd_3Ga_{0.05}$ samples before and after ball milling and PECS. From this figure it is apparent that the sample sintered for one minute has a substantially smaller peak shift than the sample sintered for one hour. This result suggests that the dopant segregation occurs primarily during the sintering stage, and as such, a one minute hold was utilized for all further samples studied in this series.

An additional sample of $CePd_3Ga_{0.02}$ was arc melted, ball milled for 12 minutes, and sintered for one minute to compare with the properties of the $CePd_3Ga_{0.05}$ sample. The results of transport property measurements for these two materials are consistent with the expected trends for dopant compensation. In particular, the plot of the Seebeck coefficient in Figure 7.5 shows that both of these samples display α values approximately 10 μV/K to 25 μV/K larger than those of the nanostructured samples without gallium. The data for the

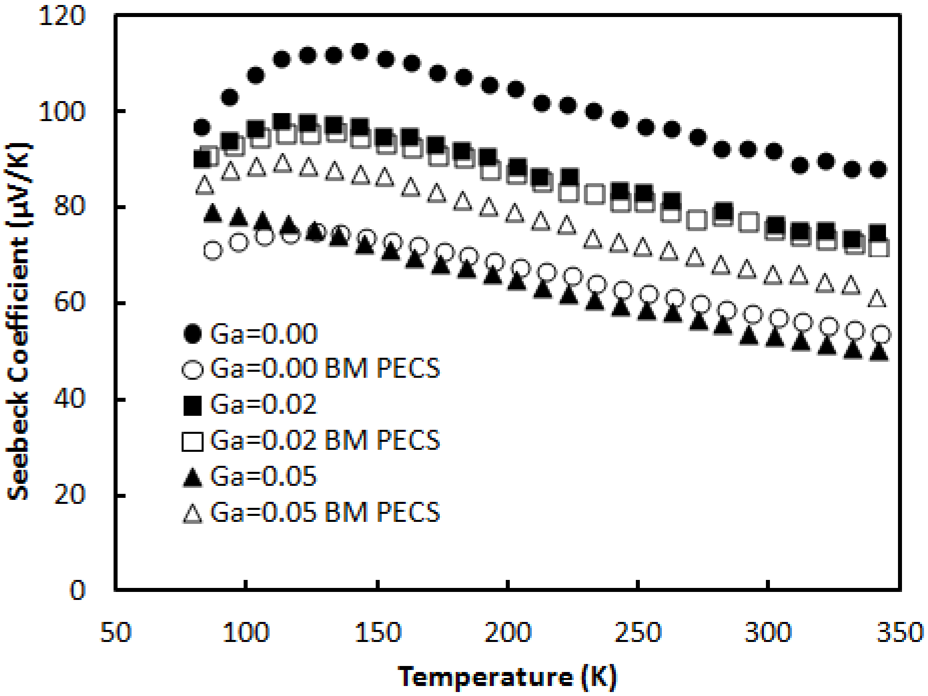

Figure 7.5: Seebeck coefficient of $CePd_3Ga_x$ before and after ball milling and PECS.

corresponding gallium-filled microstructured samples have also been included for comparison.

From these data, two trends are apparent. The first is that the temperature dependence of α near 100 K in the gallium filled nanostructured samples more closely resembles that of the unfilled nanostructured samples than it does the gallium-filled microstructured samples, although a shift in the peak temperature can still be seen relative to the $CePd_3$ control sample. In addition to this, the magnitude of α is larger in the nanostructured sample containing 2 at.% gallium than it is in the 5 at.% sample. These results together suggest that the gallium content is the dominant doping mechanism controlling the Seebeck coefficient in these materials, although comparison with the microstructured gallium-filled samples shows that the grain size reduction also has an important effect on the overall behavior.

The Hall coefficient of the nanostructured $CePd_3Ga_{0.02}$ sample was measured in order to further explore the effects of combining these approaches. The results of this measurement

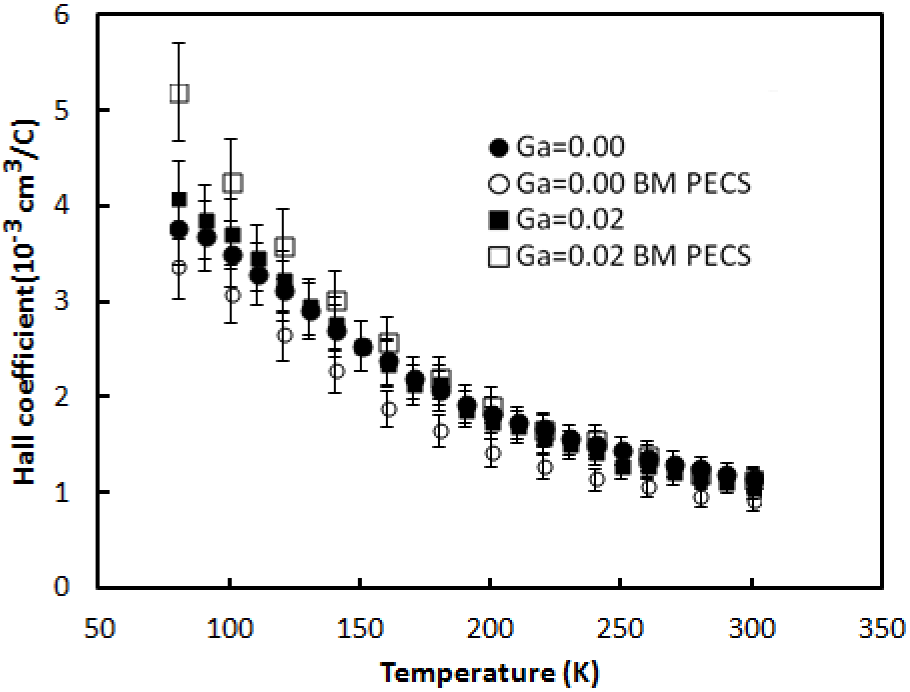

Figure 7.6: Hall coefficient of $CePd_3Ga_x$ before and after ball milling and PECS. The included error bars represent an estimated uncertainty of 10%.

are included in Figure 7.6 and match reasonably well with the results of the $CePd_3$ and $CePd_3Ga_{0.02}$ samples, especially for $T \geq 200$ K, where R_H is a more accurate probe of the carrier density. The included error bars represent an estimated uncertainty of 10% arising from the limited precision of the sample thickness measurement and the typical errors associated with the linear fit of the resistance versus field plots. All three of these samples display Hall coefficients slightly larger than the unfilled nanostructured sample, further suggesting that the gallium partial filling dominates the overall behavior of the free carriers in these materials.

The lattice thermal conductivity was also significantly reduced and matched well with the expected behavior for nanostructured $CePd_3$ to within experimental error. The magnitude of the resistivity for the nanostructured samples decreased slightly as the gallium content was increased. The combination of these trends resulted in a marginal but favorable decrease in κ'. Even when combined with the relative improvement in α, however, these results failed to produce any increase in ZT relative to the microstructured $CePd_3$ control sample.

In spite of this failure, this study demonstrates that combining these approaches appears to result in a partial cancellation of their negative effects on the thermoelectric performance of the material. Given the large number of possible choices for composition and processing conditions, there may still be a specific combination that will result in an increase in ZT, and the results included here thus establish a useful basis for further study.

7.2 Nanostructured $CePd_2Pt$

Although thermal resistivities are not strictly additive [18], it is possible to introduce multiple phonon scattering mechanisms into the same material in order to maximize the thermal conductivity reduction. In order to explore the possibility of combining point defect and grain boundary scattering, a sample of $CePd_2Pt$ was arc melted in the manner previously described. The sample was milled for 12 minutes and sintered through PECS for one minute at 820°C under 56 MPa of uniaxial pressure.

Measurements of the transport properties of this sample indicate a mixture of effects observed in the separate series. Most notably, the results of the lattice thermal conductivity reduction are included in Figure 7.7, which shows that κ_l is lower in this material than it is in either the nanostructured and platinum substituted samples are on their own.

In addition to these data, the results of the thermal conductivity ratio are included in Figure 7.8. From this figure it can be seen that the combined effects of these approaches on the lattice thermal conductivity are sufficiently large to enable a reduction in κ' that neither approach can achieve on its own.

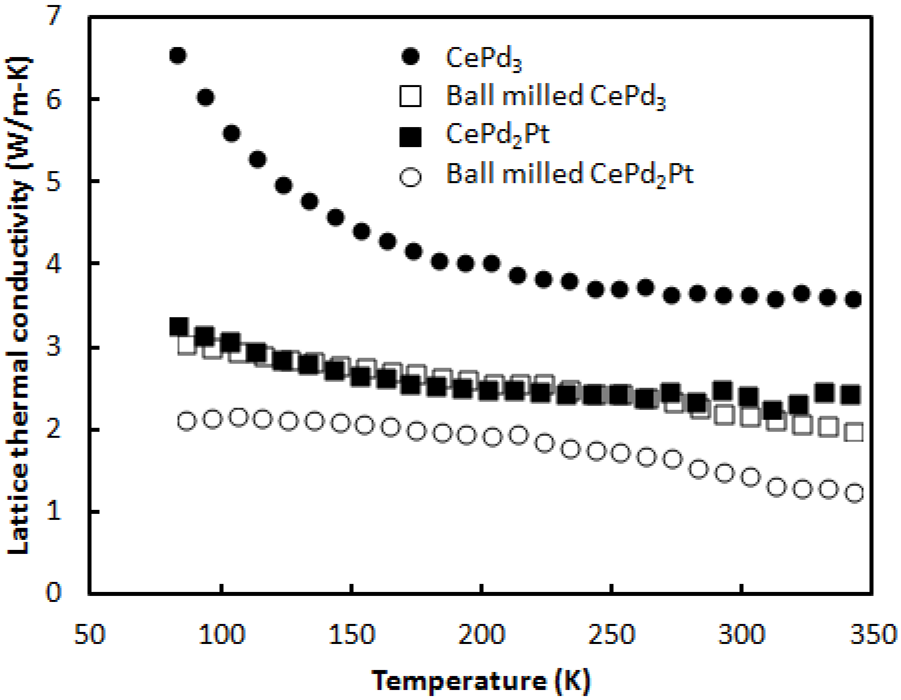

Figure 7.7: Comparison of lattice thermal conductivity of $CePd_3$ modified in various ways.

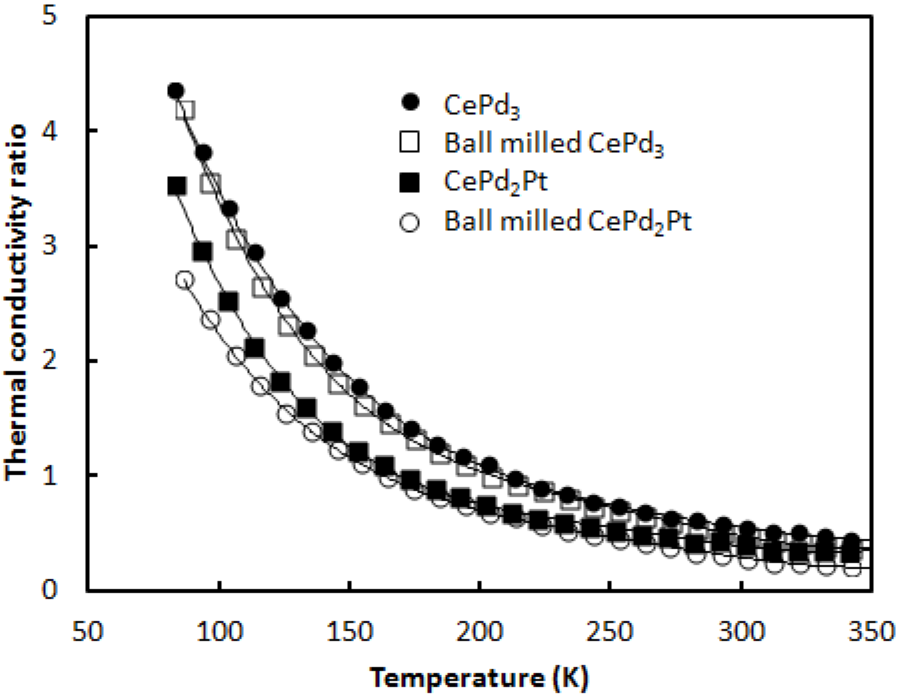

Figure 7.8: Thermal conductivity ratio of $CePd_3$ modified in various ways. Solid lines are a guide for the eye.

7.3 Nanostructured $\mathbf{CePd_2Pt}M_x$

In the final series of $CePd_3$-based compounds examined in the course of this study, three different modification strategies were combined in an attempt to further enhance ZT. Samples of $CePd_2PtGa_x$ were arc melted, ball milled, and sintered through PECS in the manner described above. The behavior of the Seebeck coefficient closely resembled that of the nanostructured $CePd_3Ga_{0.02}$ samples in Figure 7.5, with the only difference being a slight change in the temperature dependence of the linear portion ($T > 150$ K) that mimicks the behavior of $CePd_2Pt$ seen in Figure 4.4. The change in thermal conductivity was also very similar to that of the nanostructured $CePd_2Pt$ samples seen in Figure 7.7 and Figure 7.8.

Although a favorable reduction in κ' can be achieved by combining these mechanisms, the value of α remained too low for any improvement in ZT to be observed. Nonetheless, this study has demonstrated that combining chemical substitutions and/or processing methods in novel ways may enable net enhancements in the thermoelectric properties of materials such as $CePd_3$ that may not be otherwise achieved through each approach separately. The limited number of combinations attempted in this work leaves a substantial range of joint composition and processing conditions available for further study.

Chapter 8

Related compounds

Given the sensitivity of the IV state in $CePd_3$ to even small changes in composition and structure, it is generally very difficult to find ways of decreasing the thermal conductivity without also affecting the electronic properties. For this reason, it is desirable to identify other base compounds that are not already optimally doped so that the thermoelectric properties may be simultaneously optimized.

Several other strongly correlated materials are known to display intermediate valence, mixed valence, and/or Kondo-type behavior that may give rise to favorable thermoelectric properties. These compounds exist within a wide range of stoichiometry ratios that can be described by the general chemical formula $R_xT_yM_z$, where R is a lanthanide or actinide element with $1 < x < 3$, T is a transition metal or noble metal element with $1 < y < 3$, and M is a p-block element with $0 < z < 4$.

These compounds form in various crystal structures that also span a wide range of complexity, including the relatively simple perovskite-like RT_3M_z (Cu_3Au-type; e.g. $CePd_3B_x$ [39]), the hexagonal RT_2M_3 ($PrNi_2Al_3$-type; e.g. $CeNi_2Al_3$ [120]), and the complex cubic $R_3T_3M_4$ ($Y_3Au_3Sb_4$-type; e.g. $Ce_3Pt_3Sb_4$ [121]). The available data on thermoelectric properties of these compounds suggest that some of them may be close to the ranges necessary for high ZT. In order to explore these possibilities, a few of these materials were synthesized and analyzed as part of this study.

8.1 $\mathbf{EuPd_3}M_x$

8.1.1 Background and motivation

All of the lanthanide elements crystallize into the Cu_3Au structure when combined with palladium in a 1:3 ratio, and all of these compounds have been reported to combined with boron in a 1:3:1 ratio to form a perovskite analog phase [39]. $EuPd_3B$ displays a lattice parameter significantly larger than the value that would be expected based on the trends for $R$$Pd_3B$, and this anomaly is a strong indication of IV/MV behavior in this material.

Examination of lattice parameter, magnetic susceptibility, and XANES data for the $EuPd_3B_x$ series combined with density functional theory (DFT)-based calculations have confirmed that the europium atoms exist in both the 2+ and 3+ configuration for $0.2 \leq x \leq 0.5$. Only Eu^{3+} seems to be present for $x \leq 0.2$, while the solubility of boron into the interstitial site saturates for $x > 0.5$ [122]. Although the temperature dependence of these spectroscopic analyses suggest that the europium atoms exist in the MV and not IV state, it appears from these studies that boron doping nonetheless allows for precise control of the $4f$ peak relative to the Fermi level. For this reason, it is worth examining this series to search for signs of enhanced Seebeck coefficient.

8.1.2 Experimental methods

Samples of $EuPd_3B_x$ were prepared by arc melting pieces of europium, palladium, and boron in the appropriate stoichiometric ratios. Mass losses as a result of arc melting were on the order of 1 %. Europium has a lower vapor pressure and a higher oxygen affinity than cerium, which introduces additional concerns regarding phase purity and sample stoichiometry. In order to address these concerns, SEM and EDS experiments were performed on these samples

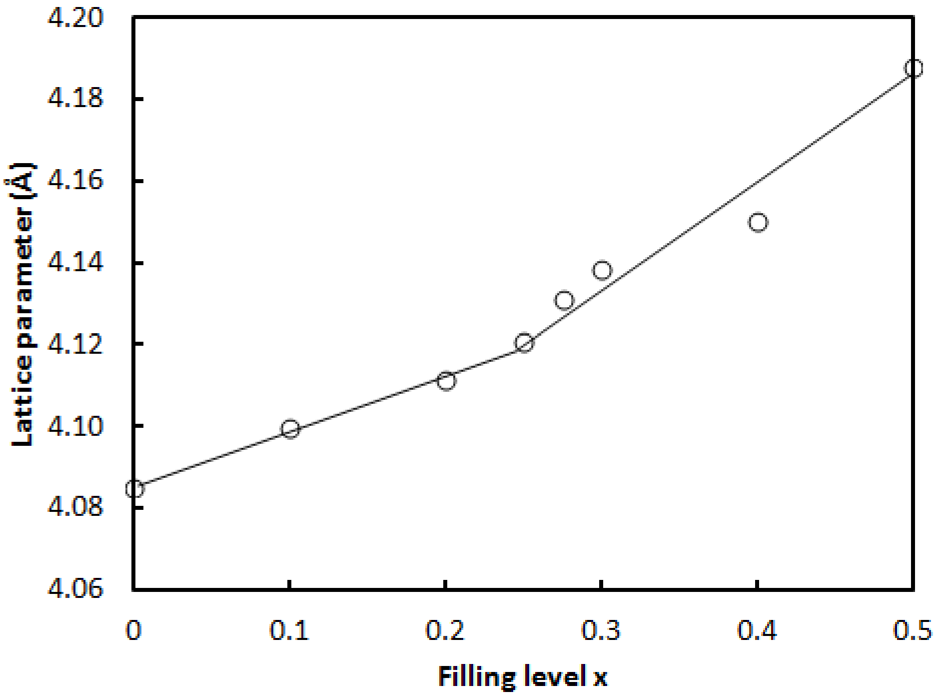

Figure 8.1: Lattice parameter of $EuPd_3B_x$. Solid lines are a guide for the eye.

after arc melting.

8.1.3 Results and discussion

XRD analysis of the samples after arc melting indicated single phase materials in the Cu_3Au-type structure with no obvious impurity phases present. Results of lattice parameter refinements are included in Figure 8.1 and show a systematic increase with increasing boron content. Consistent with previous reports [122], a kink is observed for $x \approx 0.25$.

Although the XRD results suggest these materials are single phase, SEM and EDS analysis (not included) show what appear to be small amounts of an unidentified oxide impurity phase not detected through XRD. These samples tended to be porous and brittle, which may be at least partially a result of the presence of this secondary phase. For this reason, it is difficult to attribute the absolute magnitudes of the electrical resistivity and thermal conductivity to the intrinsic properties of the materials. The Seebeck coefficient and temperature dependence of the resistivity may, however, still be reliably determined, as they depend predominantly on the electronic structure and are mostly insensitive to porosity and small volume fractions of impurity phases.

The measured Seebeck coefficient as a function of temperature for each sample has been included in Figure 8.2. A general trend emerges in these data that is consistent with the lattice parameter results as well as the DOS calculations in the literature [122]. For samples with $0 < x < 0.25$, the Seebeck coefficient is small, negative, and increases in magnitude linearly with increasing temperature, consistent with typical metallic behavior. For $x = 0.25$, the temperature dependence of the Seebeck coefficient is linear but with a positive slope, and it crosses over from n-type to p-type at $\sim$275 K. The sample with $x = 0.275$ also shows linear temperature dependence with a positive slope and larger positive values. A change in behavior is observed for $x \geq 0.3$, wherein the temperature dependence is no longer linear, and a maximum as a function of composition occurs at approximately $\alpha = 25$ μV/K for $x = 0.3$. This behavior is overall consistent with a crossover from a simple metallic system to one in which magnetic and/or other types of scattering processes dominant to the electronic properties.

The temperature dependence of the electrical resistivity also shows variations consistent with the transition in the lattice parameter and Seebeck coefficient mentioned above. The results of these measurements are included in Figure 8.3. A systematic change in behavior is observed as the temperature dependence gradually shifts from the $\rho \approx \rho_0 + a_0 T$ behavior expected for a conventional metal to the $\rho \approx \rho_0 + d_0 \ln T$ behavior expected for a system in which spin-flip scattering dominates.

It is interesting to note that the sign of d_0 is positive in this system, while it is negative

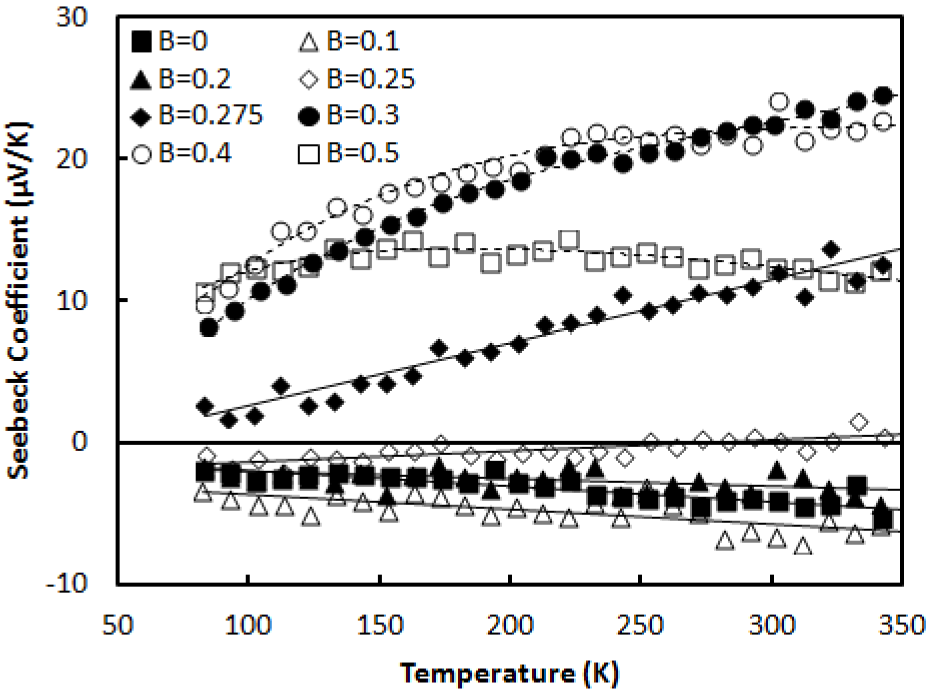

Figure 8.2: Seebeck coefficient of EuPd$_3$B$_x$. Solid lines are linear fits to the data, while dashed lines are a guide for the eye.

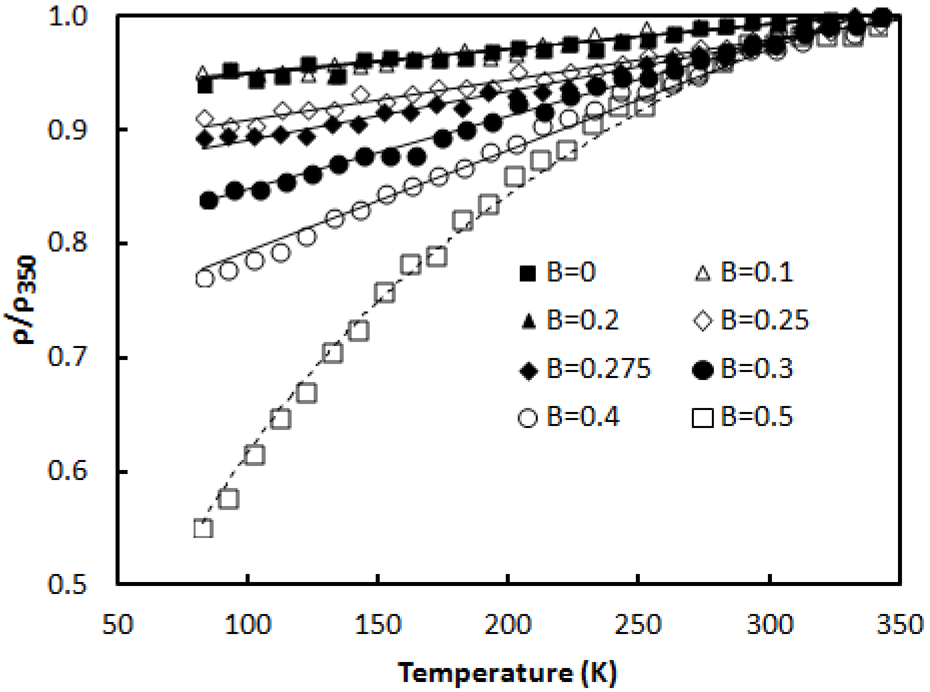

Figure 8.3: Normalized electrical resistivity of EuPd$_3$B$_x$. Solid lines are linear fits to the data, while the dashed line is fit to $\rho/\rho_{350} = \rho_0/\rho_{350} + (d_0/\rho_{350}) \ln T$.

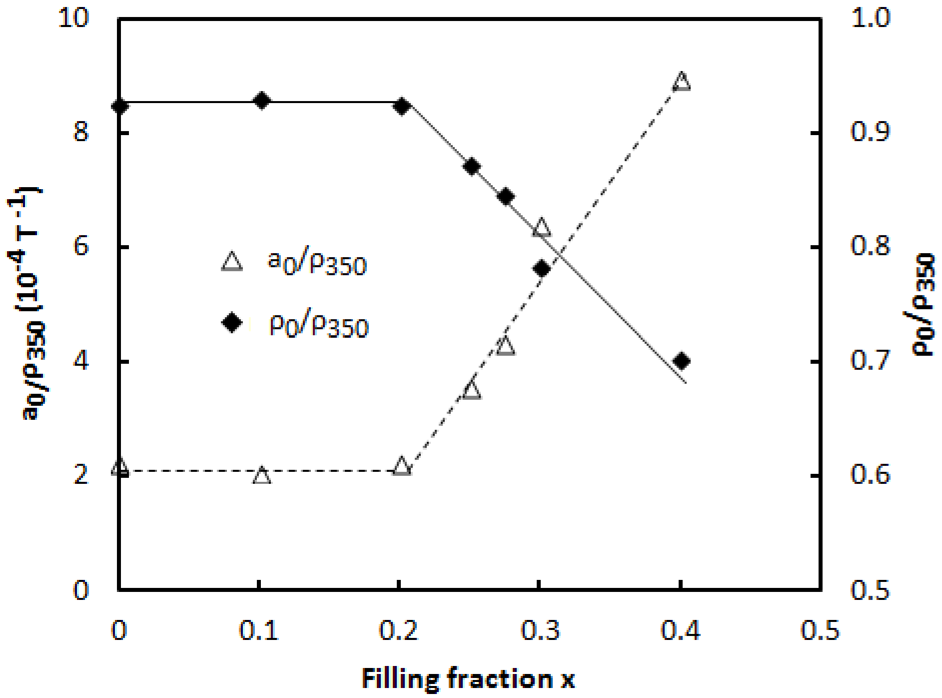

Figure 8.4: Linear fit parameters for the normalized electrical resistivity of EuPd$_3$B$_x$. Solid and dashed lines are a guide for the eye.

in CePd$_3$B$_x$. This indicates that the exchange energy between the local and conduction electrons is positive in this material.

These changes in the coefficients of $\rho(T)$ can be quantified by analyzing the slope and intercept of the linear fit lines in Figure 8.3. Figure 8.4 has been included to show the trends in these parameters as a function of x. No significant change is observed until the composition reaches $x \geq 0.25$, at which point a linear increase in a_0/ρ_{350} and decrease in ρ_0/ρ_{350} are seen as x is further increased. Since the behavior of the system appears to evolve gradually from $\rho(T) \approx \rho_0 + a_0 T$ to $\rho(T) \approx \rho_0 + d_0 \ln T$, it is possible that these changes in the fit parameters are simply indicative of an increasing contribution from the $d_0 \ln T$ term that does not become significant until $x > 0.4$.

Although reliable thermal conductivity data could not be obtained from the samples examined in this study, the measured values were on the order of 1 W/m-K to 10 W/m-K, and a decrease in magnitude was generally observed as x was increased. These results are consistent with the trends for CePd_3M_x. The Seebeck coefficient of the doped samples did not reach the range of 100 μV/K necessary for high ZT, which suggests that this system is not suitable for thermoelectric cooling. A systematic change in the transport properties was observed that is consistent with a change in the dominant scattering mechanism between the metallic and mixed valence regions. Additional studies with other M filler elements may yield further insights into the general behavior of the material.

8.2 $\mathbf{Ce_3Pt_3Sb_4}$

8.2.1 Background and motivation

$\text{Ce}_3\text{Pt}_3\text{Sb}_4$ belongs to a larger family of $R_3T_3M_4$ compounds that crystallize in the $\text{Y}_3\text{Au}_3\text{Sb}_4$-type structure [121], as pictured in Figure 8.5. These materials are interesting for thermoelectric applications for a number of reasons. The most immediate of these is that the size and complexity of the unit cell are favorable for intrinsically low lattice thermal conductivity. Typical κ_l values for these materials are relatively low and on the order of a few W/m-K, including as low as 1.5 W/m-K in $\text{Sm}_3\text{Au}_3\text{Sb}_4$ [123]. This matches the lowest value observed in the CePd_3 compounds studied here, which was obtained only after carefully combining multiple thermal conductivity reduction mechanisms.

The other main reason these materials are interesting for thermoelectric applications is that they can be loosely classified as narrow-gap semiconductors, and as such they tend to display relatively large Seebeck coefficient and low resistivity values typical for such compounds. In addition to this, $\text{Ce}_3T_3M_4$ materials often display Kondo-type behavior. The mixture of the Kondo effect and semiconductor-like properties in some of these compounds

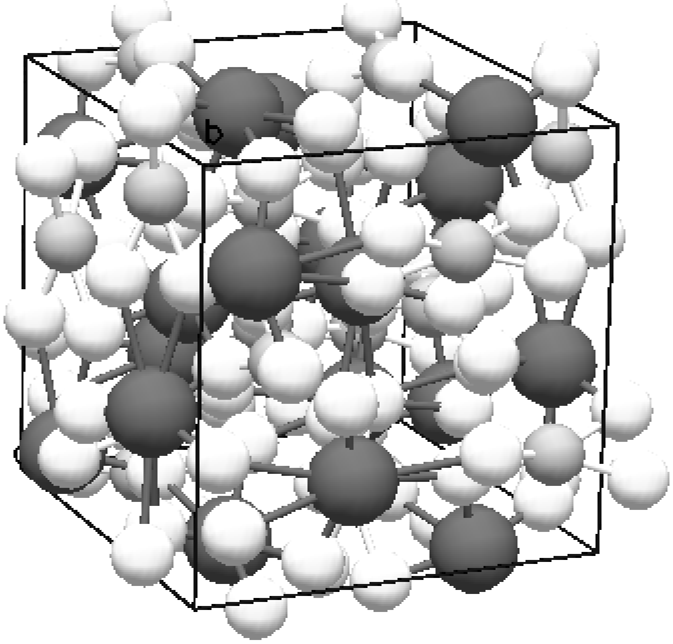

Figure 8.5: Crystal structure diagram of $Ce_3Pt_3Sb_4$. Cerium atoms (dark gray) are in a distorted dodecahedral coordination with the antimony atoms (light gray), while the platinum atoms (medium gray) are in a distorted tetragonal configuration. Edge and face sharing cerium polyhedra are both present.

leads to their description as "Kondo insulators" [124], while other compounds in this family behave like Kondo metals, similar to $CePd_3$. It is thus possible to observe a wide variety of behavior in these systems depending on composition.

A demonstration of this variety can be seen in the resistivity of $R\mathrm{Cu_3Sb_{4-x}Sn_x}$ compounds with R = La, Ce, Pr, Nd, Sm, and $x = 0.05$ and 0.10 [125]. While all of the compounds without cerium show what appears to be a nearly linear temperature dependence in the resistivity with magnitudes on the order of 10^{-5} Ω-m, the samples containing cerium show a dramatically different dependence that appears to correspond with the $\ln(T)$ behavior typical for Kondo metals.

Given the large number of isostructural compounds with similar lattice parameters in this family, an enormous number of possible variations exist that can be formed through single or double substitutions on the R, T, and/or M sites. Such solid solution mixing can be expected to result in a robust range of electronic properties while simultaneously inducing a reduction in the lattice thermal conductivity.

Two of the few complete thermoelectric studies available on this compound explore the properties of $\mathrm{Ce_3Pt_{3-x}Cu_xSb_4}$ [124] and $\mathrm{Ce_{3-x}Nd_xPt_3Sb_4}$ [126]. In these studies, the authors show that the material can be systematically doped through substitutions on both the cerium and platinum sites. Copper substitutions on the platinum site, for example, can reduce the electrical resistivity at 100 K by three orders of magnitude, from 10^{-2} Ω-m in $\mathrm{Ce_3Pt_3Sb_4}$ to 10^{-5} Ω-m in $\mathrm{Ce_3Cu_3Sb_4}$. The Seebeck coefficient also changes dramatically in this system, from a peak value at 100 K of 300 μV/K in $\mathrm{Ce_3Pt_3Sb_4}$, to -175 μV/K in $\mathrm{Ce_3Pt_{2.5}Cu_{0.5}Sb_4}$, to approximately zero in $\mathrm{Ce_3Cu_3Sb_4}$.

This strong sensitivity to composition changes exposes one of the biggest problems related to this family of compounds, which is that stoichiometry can be very difficult to control during arc melting due to vaporization of M elements such as antimony and bismuth. The sensitivity of these systems to compositional variation is apparent even in the nominally stoichiometric $Ce_3Pt_3Sb_4$ control samples in Ref. [126]. As the authors show, the room temperature resistivity varies by an order of magnitude between two nominally identical samples, and the peak Seebeck coefficient ranges from approximately 230 μV/K to 350 μV/K. The only difference between the samples is that one was measured directly from arc melting and the other after powder processing, respectively. Since these changes in the transport properties are comparable to those resulting from compositional modifications, it is imperative to improve stoichiometry control in these materials in order to better distinguish between the effects of off-stoichiometry and intentional doping.

Two significant challenges arise that make phase purity difficult to obtain. The first is that these compounds tend to have relatively high melting points, which means that arc melting is generally necessary to form them. However, antimony and bismuth tend to vaporize readily when heated to these temperatures. Excess amounts of approximately 5 at.% of the volatile elements are commonly added to account for this vaporization [126], and although the resulting XRD patterns are reported to be single phase, the limited resolution of this technique for detecting secondary phases does not completely eliminate the concerns over stoichiometry control.

This problem is amplified by the second synthesis challenge common in these materials, which is that the RTM-type phase is very close in stoichiometry to $R_3T_3M_4$. Thus even if problems regarding M vaporization are resolved, any local deviations in stoichiometry may lead to the spontaneous formation of RTM.

There is an obvious need to develop more consistent synthesis techniques for this system if it is to be properly studied and explored as a candidate thermoelectric material. This has motivated the current brief study, which considers a precursor synthesis approach as a way of improving stoichiometry control, homogeneity, and overall sample quality.

Inspired by the success of the this approach in the synthesis of CePd$_3M_x$ compounds containing volatile elements such as tellurium, an analysis of the Ce-Sb [127] and Pt-Sb [128] binary phase diagrams revealed that only two congruently melting compounds exist between these systems. The first is CeSb, which melts at 1820°C (2093 K), and the other is PtSb$_2$, which melts at 1225°C (1498 K). The latter compound is coincidentally a narrow-gap semiconductor identified by Slack as a possible low temperature thermoelectric material [12]. Since CeSb has an insufficiently high antimony content to enable the appropriate atomic ratios in the final compound, PtSb$_2$ is the only suitable precursor phase in either of these systems.

8.2.2 Experimental methods

Platinum melts at 1769°C (2042 K), and antimony at 631°C (904 K). A eutectic point exists in the Pt-Sb system at 31.5 at.% antimony and 630°C (903 K), below which a mixture of Pt$_3$Sb and Pt$_3$Sb$_2$ forms [128]. In order to expedite the solid state reaction of the antimony with the platinum into the PtSb$_2$ phase, the Pt-Sb eutectic phase was first created by mixing 68.5 at.% platinum with 31.5 at.% antimony in an evacuated and sealed quartz ampoule. This ampoule was placed into a furnace pre-heated to 800°C (1073 K) for 90 seconds then removed and allowed to slowly cool to room temperature. A small metallic bead formed in the bottom of the ampoule that consisted of 98.6% of the starting mass, suggesting that this temperature was high enough to cause approximately 13% of the antimony to vaporize before reacting.

This bead was crushed with a mortar and pestle to increase its surface area, then placed into another quartz ampoule with an appropriate amount of antimony to produce a 1:2 atomic ratio of platinum and antimony. The mass loss in the eutectic sample was assumed to be entirely antimony, and the composition was thus normalized to the amount of platinum initially present. A slight excess of approximately 1 at.% antimony was further added to help drive the solid state reaction and compensate for any small amounts of additional vaporization.

The ampoule was evacuated, sealed, and placed back into a furnace at 900°C (1173 K) for 48 hours, then removed and allowed to slowly cool to room temperature. The resulting sample was brittle, highly porous, and displayed a dull gray color. This process resulted in a mass loss of 2.6%, again suggesting that some antimony vaporized before reacting. Examination under an optical microscope reveled the presence of many small and faceted crystallites approximately 1 mm in size. XRD analysis indicated the presence of only the expected $PtSb_2$ pyrite phase.

The stability of this $PtSb_2$ phase was examined by repeatedly melting it directly in the arc melter. Considerable vaporization was observed as a result of this process that corresponded with a mass loss of over 50%. XRD analysis after arc melting indicated the presence of PtSb, suggesting that a relatively large portion of antimony had vaporized. However, since $PtSb_2$ is only 23.7% antimony by mass, the magnitude of mass loss suggests that at least some of it was also $PtSb_2$. Either way, these results suggest that $PtSb_2$ is not an effective precursor for arc melting, as it does not appear to be any more stable upon melting than elemental antimony. This may be related to the relatively low melting point of the compound compared to the temperatures reached inside the arc melter.

A sample of $Ce_3Pt_3Sb_4$ was arc melted directly from the pure elements to compare the level of mass loss typical for this process, and the results of this experiment produced an overall loss of only 1.1% after melting. Assuming the mass lost to be entirely antimony, this result corresponded with a loss of approximately 13 at.% Sb. XRD patterns of this sample indicated the clear presence of both CePtSb and $Ce_3Pt_3Sb_4$. To encourage the formation of the $Ce_3Pt_3Sb_4$ phase, the sample was placed back in the arc melter with additional antimony and remelted until a sample with a final mass within 1% of the starting mass was obtained.

XRD results of this final sample still indicated a mixture of CePtSb and $Ce_3Pt_3Sb_4$. Based on the procedures described in Ref. [126], this ingot was annealed for one week at 900°C (1173 K). XRD analysis of the sample after annealing showed only the presence of $Ce_3Pt_3Sb_4$, suggesting that this approach is effective for producing single phase materials.

Upon cutting this sample to prepare it for transport property measurements, however, it was found to be porous and relatively brittle. These poor mechanical properties are likely a result of the substantial phase change that appears to have occurred during annealing.

In an attempt to produce a dense pellet suitable for measurements through powder processing, the material was ball milled in a way similar to the nanostructured $CePd_3$ samples mentioned above. The CePtSb phase reappeared in the XRD patterns after ball milling and was still present after the powder was sintered through PECS. Further annealing of the sample after PECS did not eliminate this phase. Because of these difficulties with producing dense, phase-pure samples, transport properties could not be reliably measured for this material.

8.2.3 Results and discussion

Based on the results of this study, it appears that precursor synthesis is not a viable option for improving the stoichiometry control of $Ce_3Pt_3Sb_4$-based compounds. $PtSb_2$ is the only suitable precursor for this system, but it does not appear to be stable during arc melting.

Melting at lower temperatures in an induction furnace may allow for improved stability, and this precursor approach may still be appropriate for other compositions in the $R_3T_3M_4$ family for which suitable R-M or T-M binary compounds exist.

Although single phase materials could be produced through the conventional approach of arc melting with excess antimony and then annealing, the poor mechanical properties of these samples made reliable measurements difficult to obtain. Powder processing and further annealing did not help to produce a dense, single phase material suitable for measurement.

In spite of these difficulties, this conventional approach still appears to be the most reliable way of producing these materials. This suggests that future studies focusing on optimization of the milling, sintering, and annealing conditions necessary for creating homogeneous, dense, single phase, powder processed samples may yield useful insights into improving stoichiometry control.

The results of this study have also shown that single phase $PtSb_2$ powder can be produced through solid state reactions. Although this system is unrelated to the cerium-based compounds on which the current work is focused, this insight may be useful for the synthesis of bulk samples of $PtSb_2$-based compounds suitable for further study as candidate materials for cryogenic thermoelectric cooling.

8.3 $CeNi_2Al_3$

8.3.1 Background and motivation

Based on results of Sun [120, 129], $CeNi_2Al_3$ has been identified as another candidate system for low temperature thermoelectric applications. The compound crystallizes in the hexagonal $PrNi_2Al_3$-type structure, as seen in the diagram in Figure 8.6. This system is an excellent

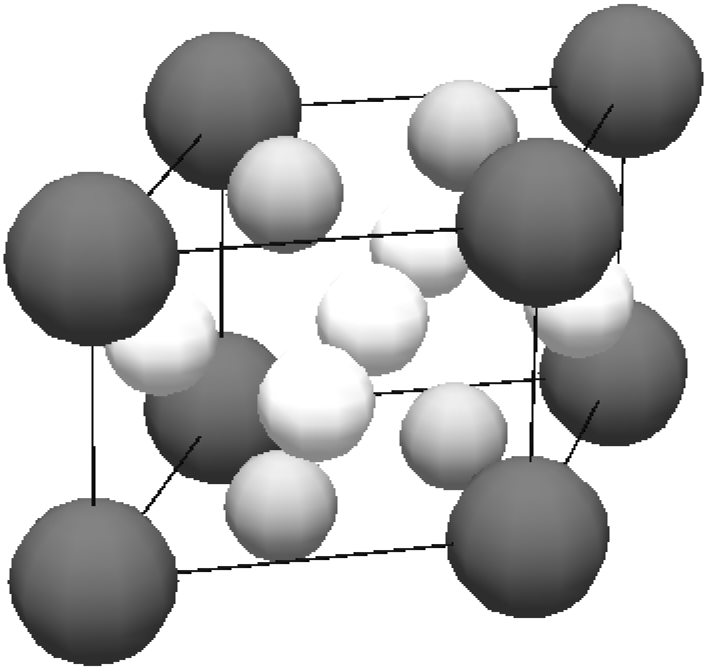

Figure 8.6: Crystal structure diagram of $CeNi_2Al_3$. Cerium atoms (dark gray) are at the corners of the rhomboid, the nickel atoms (medium gray) are on the top and bottom faces, and the aluminum atoms (light gray) are on the side faces and center.

example of one in which the base compound is not optimized, as the undoped material has a maximum Seebeck coefficient of only ~50 μV/K at 300 K that decreases with decreasing temperature. Sun reports that the substitution of copper onto the nickel site results in the simultaneous optimization all of three thermoelectric properties, increasing α up to approximately 90 μV/K, decreasing ρ to 10^{-6} Ω-m, and decreasing κ_l to under 5 W/m-K at 100 K for $x = 0.8$.

In an attempt to reproduce these results and better determine the range of optimal copper content, samples of $CeNi_{2-x}Cu_xAl_3$ were synthesized and measured as part of this work.

8.3.2 Experimental methods

Guided by the available reports in the literatures [120, 129], samples of $\mathrm{CeNi}_{2-x}\mathrm{Cu}_x\mathrm{Al}_3$ (0.6 $< x <$1) were prepared in the standard arc melting technique described in Chapter 2. Mass losses for these samples were less than 1%. Some of the samples were also crushed through vibratory milling in the same way as the nanostructured CePd_3 samples were prepared above, then sintered through PECS at 800°C for 1 minute under 60 MPa of uniaxial pressure in an attempt to produce bulk nanostructured samples. Although substantial peak broadening was observed in the XRD patterns of the ball milled powders, analysis of the XRD patterns and transport properties after PECS showed no apparent changes relative to the original arc melted samples, indicating that these PECS conditions are not appropriate for preservation of the nanoscale features.

8.3.3 Results and discussion

A substantial shift in the lattice parameter was observed based on the XRD patterns obtained after arc melting, indicating an increase in the lattice parameter as x increases. The results of lattice parameter calculations are included in Figure 8.7 and are consistent with the values previously reported for similar compounds [120, 129].

Results of Seebeck coefficient measurements are included in Figure 8.8 and are consistent with the results of Ref. [120]. Although Ref. [129] reported values as high as 90 μV/K in samples with $x = 0.8$ at 80 K, the largest value observed in this study was 65 μV/K at the same temperature for $x = 0.7$, essentially identical to the results of Ref. [120]. This value is substantially higher than would be expected for a conventional metal, but it is still approximately two to three times smaller than what is needed for $ZT > 0.1$.

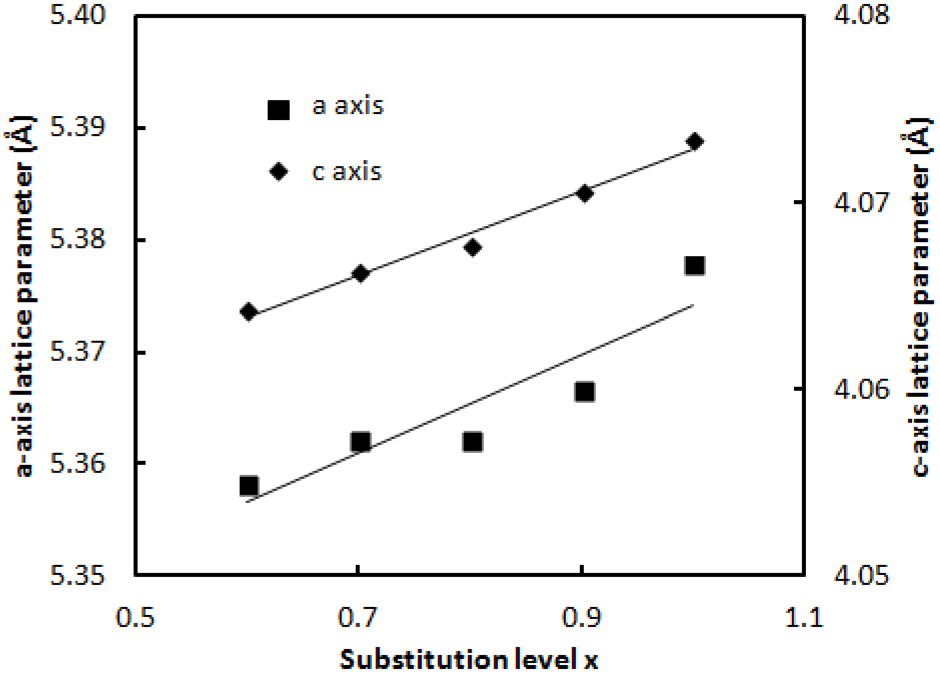

Figure 8.7: Lattice parameter of $CeNi_{2-x}Cu_xAl_3$. Solid lines are linear fits to the data.

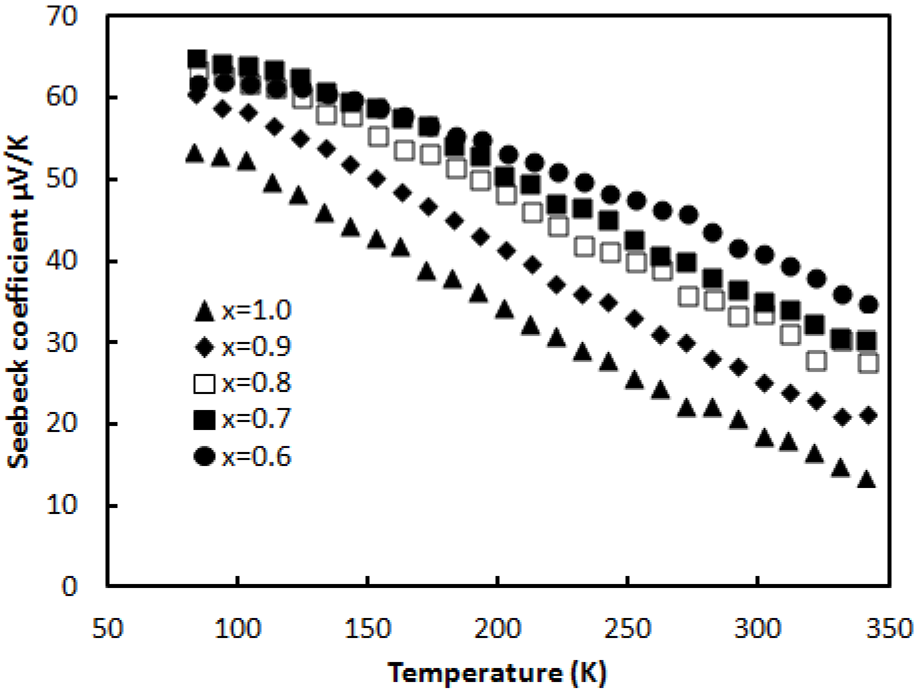

Figure 8.8: Seebeck coefficient of $CeNi_{2-x}Cu_xAl_3$.

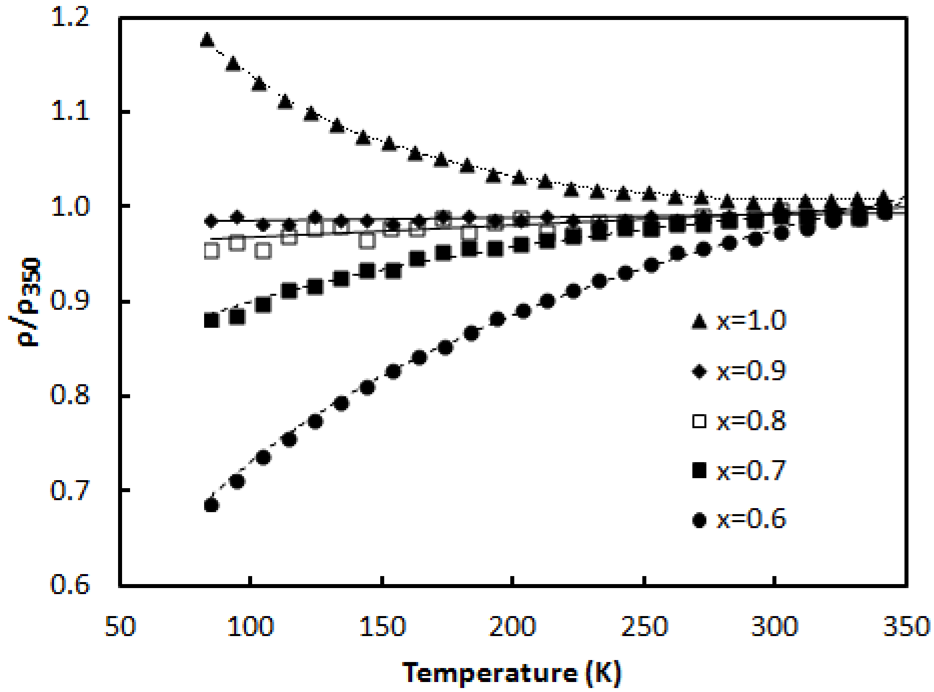

Figure 8.9: Normalized electrical resistivity of $\mathrm{CeNi}_{2-x}\mathrm{Cu}_x\mathrm{Al}_3$. A progression in behavior is observed as x is increased. Dashed lines are fits to $\rho/\rho_{350} = \rho_0/\rho_{350} + (d_0/\rho_{350}) \ln T$, solid lines are fits to $\rho/\rho_{350} = \rho_0/\rho_{350} + (a_0/\rho_{350})T$, and the dotted line is a fit to $\rho/\rho_{350} = \rho_0/\rho_{350} - (d_0/\rho_{350}) \ln T + (a_0/\rho_{350})T$. This evolution indicates a gradual transition in the nature of the electronic scattering mechanisms with composition.

The electrical resistivity data are included in Figure 8.9. Due to problems with sample porosity, data for each set have been divided by the corresponding value at 350 K in order to emphasize the temperature dependence. The values of ρ_{350} were on the order of approximately 10^{-6} Ω-m and identical to within a factor of two for all samples, indicating that no significant change in magnitude occurs as a function of composition.

A gradual change in the behavior of $\rho(T)$ can be seen as x is increased. For relatively small $x \leq 0.7$, $\rho(T) \approx \rho_0 + d_0 \ln T$, indicating the dominant contribution from magnetic scattering with a positive exchange energy. For $0.8 \leq x \leq 0.9$, the data can be fit sufficiently well with only the linear contribution from phonon scattering of the form $\rho(T) \approx \rho_0 + a_0 T$. For $x = 1$, both the linear and logarithmic terms must be considered in order to achieve an accurate fit to the data, and ρ is of the form $\rho(T) \approx \rho_0 + a_0 T + d_0 \ln T$, now with a negative sign of d_0 that indicates a change in the sign of the exchange energy. This change in sign of d_0 is consistent with the results of Ref. [129], in which it was established that antiferromagnetic ordering begins for $x \approx 1.0$. The increased importance of the linear term with increasing x may be a result of changes in the Debye temperature with composition. Overall, this change in behavior is similar to that seen in $\mathrm{EuPd_3B}_x$, in which the magnitude of the magnetic scattering contribution to the resistivity can also be controlled through composition.

Based on the results of this work, this specific solid solution does not appear to be a viable candidate for high ZT at low temperatures. Although the resistivity and lattice thermal conductivity are both within the range necessary for achieving reasonably strong thermoelectric performance, the maximum Seebeck coefficient of 65 μV/K corresponds with a maximum theoretical ZT of only $\sim$0.17 at 80 K. Further study of the effects of substitutions on the cerium and aluminum sites may yield additional insights into how the electronic and thermal properties of the material can be controlled. Since it does not appear that this type of compositional modification causes any appreciable change in the magnitude of the electrical resistivity, emphasis should be placed on exploring the appropriate combination of chemical pressure and doping for maximizing the Seebeck coefficient. If this can be done to achieve $\alpha \sim 100$ μV/K, this material has potential as a more cost effective alternative to the palladium and platinum based compositions discussed above.

Chapter 9

Results and Conclusions

This work has presented a systematic study of structure-processing-property relationships and thermoelectricity in several series of rare earth intermetallic compounds. The primary emphasis has been placed on $CePd_3$, as this material has one of the largest known power factors of all *p*-type bulk materials at low temperatures. A thorough combination of composition and processing modifications has been used to explore the available mechanisms for enhancing the thermoelectric properties of $CePd_3$, and some of the insights gained from these studies have been extended to brief examinations of the related compounds $EuPd_3B_x$, $CeNi_{2-x}Cu_xAl_3$, and $Ce_3Pt_3Sb_4$.

The broad goal of this study was to determine what, if any, mechanisms are available for decreasing the thermal conductivity ratio while increasing or at least maintaining the large Seebeck coefficient. Three series of chemically modified $CePd_3$ have been used to explore this possibility based on the available lattice sites on which atoms can be added or substituted. The elements chosen for these modifications were carefully selected so as to optimize their impact and/or exhaustively explore their effects, thus establishing upper and/or lower limits for the maximum possible improvements that can be made to the material through each approach.

The study of scandium substitutions on the cerium site has definitively demonstrated that no significant thermal conductivity reduction can be achieved through this route, as scandium has the maximum possible size and mass mismatch with cerium and would thus be expected to have a maximal effect on the thermal conductivity.

Platinum was chosen for substitutions on the palladium site due to the large mass mismatch and chemical similarities of the two elements, and the results of this study confirm that this approach is effective for reducing κ' while slightly increasing α. This combination has led to the highest ZT values reported to date for any bulk polycrystalline p-type material at low temperatures.

The wide variety of elements chosen for partially filling the central interstitial site, including multiple elements that had never been used in this approach before, has demonstrated that the electronic and thermal properties of the material can be separately controlled to a limited extent. As long as no structural ordering occurs, the impact of this partial filling approach on the electronic and magnetic properties is determined primarily by the filling fraction and valence electron count of M, while the effects on the lattice thermal conductivity depend primarily on the filling fraction and mass of M. Although no appreciable gains in ZT could be made through this approach, it nonetheless demonstrates a generally useful way of separately tuning the thermoelectric properties of a material.

In addition to these chemical modifications, this study reports for the first time the transport properties of a nanostructured correlated metal. The reduction in size of the $CePd_3$ grains to the nanoscale appears to significantly reduce the lattice thermal conductivity while simultaneously resulting in what may be described as morphologically-driven doping. The combination of this approach with interstitial site filling has been demonstrated as a possible way of double-doping the material such that no significant change in the electronic properties occurs. Examination of nanostructured $CePd_2Pt$ has also demonstrated that grain size reduction may be combined with other thermal conductivity reduction strategies to further reduce κ' below values that either approach can achieve on its own.

Studies of $EuPd_3B_x$ have shown for the first time that the nature of the electronic properties in this material can be carefully tuned through adjusting the boron content, although the Seebeck coefficient does not appear to be large enough to facilitate high ZT. Based on the results of the $CePd_3M_x$ series studied here, however, it may be interesting to examine the the effect of introducing other M elements into the interstitial site to see if larger α can be found.

Attempts at improving stoichiometry control in $Ce_3Pt_3Cu_4$ via solid precursor synthesis failed to produce a more stable compound suitable for arc melting. The importance of annealing in obtaining single phase materials synthesized through the conventional approach was demonstrated, and an attempt at producing this compound through powder processing approaches was also discussed. The challenge of improving stoichiometry control in this series remains. The insights gained from $CePd_{3-x}Pt_x$ regarding the importance of substituting chemically similar elements to preserve the electronic properties may be utilized in this system to further reduce its thermal conductivity after its electronic properties have been properly tuned.

Finally, $CeNi_{2-x}Cu_xAl_3$ was also examined as a possible high ZT intermetallic compound. Although copper substitution on the nickel site does appear to simultaneously improve all three thermoelectric properties, the maximum α observed is again insufficiently large to enable high ZT. Nano-scale powders of this material were successfully produced by ball milling, but the nanoscale features were not preserved after PECS. This study has thus established an upper limit on the processing conditions appropriate for producing nanostructured samples of $CeNi_{2-x}Cu_xAl_3$. Additional substitutions on the nickel and/or aluminum sites, guided by the basic trends observed in the several $CePd_3$ series studied here, may lead to further improvements in the thermoelectric properties of this material.

From a broad perspective, this work has thoroughly explored the best available ways of modifying some of the best known p-type materials for cryogenic thermoelectric applications. Although this study has produced record high ZT values for bulk polycrystalline p-type materials at low temperatures, these values are likely still too low to make solid state cryocooler device construction practical. The results of this work may nonetheless be generally useful for providing empirical feedback to theoretical models of the structural, magnetic, and transport properties of correlated metals, as well as guide future studies of other correlated systems identified as potential high ZT materials.

If such materials can be found and engineered to achieve sufficiently high ZT, the development of efficient solid state cooling technologies may finally be realized. This development would open up potentially enormous markets in commercial, industrial, military, and research cooling technologies, and extend even further mankind's ability to harness the power of nature.

REFERENCES

REFERENCES

[1] T. J. Seebeck. Magnetische Polarisation der Metalle und Erze durch Temperatur-Differenz. *Abhandlungen Akademie Wissenschaften Berlin*, 70:289–346, 1821.

[2] J. C. Peltier. Nouvelles experiences sur la caloricite des courans electrique. *Annales de chimie et de physique*, 56(1834):371, 1834.

[3] W. Thomson. Account of Researches in Thermo-Electricity. *Proceedings of the Royal Society of London*, 7:49–58, 1854.

[4] G. J. Snyder and E. S. Toberer. Complex thermoelectric materials. *Nature Materials*, 7(2):105–114, 2008.

[5] G. L. Bennett, J. J. Lombardo, R. J. Hemler, G. Silverman, C. W. Whitmore, W. R. Amos, E. W. Johnson, A. Schock, R. W. Zocher, T. K. Keenan, J. Hagan, and R. Englehart. Mission of daring: the general-purpose heat source radioisotope thermoelectric generator. In *Proceedings of the 4th International Energy Conversion and Engineering Conference, San Diego, CA*, 2006.

[6] R. Saidur, M. Rezaei, W. K. Muzammil, M. H. Hassan, S. Paria, and M. Hasanuzzaman. Technologies to recover exhaust heat from internal combustion engines. *Renewable and Sustainable Energy Reviews*, 16(8):5649–5659, 2012.

[7] F. J. DiSalvo. Thermoelectric cooling and power generation. *Science*, 285(5428):703–706, 1999.

[8] J. Yang. Potential applications of thermoelectric waste heat recovery in the automotive industry. In *Thermoelectrics, 2005. ICT 2005. 24th International Conference on*, pages 170–174. IEEE, 2005.

[9] S. B. Riffat and X. Ma. Thermoelectrics: a review of present and potential applications. *Applied Thermal Engineering*, 23(8):913–935, 2003.

[10] D. M. Rowe. *Thermoelectrics Handbook: Macro to Nano.* CRC Press, 2006.

[11] K. Biswas, J. He, I. D. Blum, C.-I. Wu, T. P. Hogan, D. N. Seidman, V. P. Dravid, and M. G. Kanatzidis. High-performance bulk thermoelectrics with all-scale hierarchical architectures. *Nature*, pages 414–418, 2012.

[12] G. Slack. *New Materials and Performance Limits for Thermoelectric Cooling, in CRC Handbook of Thermoelectrics*. CRC Press, 1995.

[13] E. S. Rittner and G. F. Neumark. Theoretical bound on the thermoelectric figure of merit of two band semiconductors. *Journal of Applied Physics*, 34(7):2071 –2077, 1963.

[14] A. Eucken and G. Kuhn. *Zeitschrift für Physikalische Chemie*, 134:193, 1928.

[15] A. F. Ioffe. *Semiconductor Thermoelements and Thermoelectric Cooling*. Infosearch, New York, 1957.

[16] H. J. Goldsmid and R. W. Douglas. The use of semiconductors in thermoelectric refrigeration. *British Journal of Applied Physics*, 5(11):386, 1954.

[17] C. Kittel. *Introduction to Solid State Physics, 8th Edition*. Wiley, New York, 2005.

[18] R. Berman. *Defects and Geometry in Condensed Matter Physics*. Cambridge University Press, New York, 2002.

[19] E. S. Toberer, A. Zevalkink, and G. J. Snyder. Phonon engineering through crystal chemistry. *Journal of Materials Chemistry*, 21(40):15843–15852, 2011.

[20] N. P. Padture and P. G. Klemens. Low thermal conductivity in garnets. *Journal of the American Ceramic Society*, 80(4):1018–1020, 1997.

[21] G. A. Slack. *Solid State Physics*. Academic Press, New York, 1979.

[22] D. T. Morelli and G. P. Meisner. Low temperature properties of the filled skutterudite $CeFe_4Sb_{12}$. *Journal of Applied Physics*, 77(8):3777–3781, 1995.

[23] D. R. Nelson. *Thermal Conduction in Solids*. Oxford University Press, New York, 1978.

[24] C. Rincón. Debye Temperature and Melting Point in AIBIIIC2VI and AIIBIVC2V Chalcopyrite Compounds. *Physica Status Solidi (A)*, 134(2):383–389, 1992.

[25] R. R. Heikes and R. W. Ure. *Thermoelectricity: Science and Engineering.* Interscience Publishers, New York, 1961.

[26] N. F. Mott. *Sir Nevill Mott: 65 Years in Physics.* World Scientific, 1995.

[27] Y. Pei, A. D. LaLonde, H. Wang, and G. J. Snyder. Low effective mass leading to high thermoelectric performance. *Energy & Environmental Science*, 2012.

[28] N. Wakeham, A. F. Bangura, X. Xu, J.-F. Mercure, M. Greenblatt, and N. E. Hussey. Gross violation of the Wiedemann-Franz law in a quasi-one-dimensional conductor. *Nature Communications*, 2:396, 2011.

[29] G. Pernot, M. Stoffel, I. Savic, F. Pezzoli, P. Chen, G. Savelli, A. Jacquot, J. Schumann, U. Denker, I. Mönch, Ch. Deneke, O. G. Scmidt, J. M. Rampnoux, S. Wang, M. Plissonnier, A. Rastelli, S. Dilhaire, and N. Mingo. Precise control of thermal conductivity at the nanoscale through individual phonon-scattering barriers. *Nature Materials*, 9(6):491–495, 2010.

[30] A. H. Carter. *Classical and Statistical Thermodynamics.* Prentice-Hall, 2001.

[31] G. D. Mahan and J. O. Sofo. The best thermoelectric. *Proceedings of the National Academy of Sciences*, 93(15):7436–7439, 1996.

[32] Y. Pei, X. Shi, A. LaLonde, H. Wang, L. Chen, and G. J. Snyder. Convergence of electronic bands for high performance bulk thermoelectrics. *Nature*, 473(7345):66–69, 2011.

[33] W. Koshibae, K. Tsutsui, and S. Maekawa. Thermopower in cobalt oxides. *Physical Review B*, 62:6869–6872, 2000.

[34] J. P. Heremans, V. Jovovic, E. S. Toberer, A. Saramat, K. Kurosaki, A. Charoenphakdee, S. Yamanaka, and G. J. Snyder. Enhancement of thermoelectric efficiency in PbTe by distortion of the electronic density of states. *Science*, 321(5888):554–557, 2008.

[35] J. P. Heremans, B. Wiendlocha, and A. M. Chamoire. Resonant levels in bulk thermoelectric semiconductors. *Energy & Environmental Science*, 5(2):5510–5530, 2012.

[36] H. Lusfeld and A. Bringer. Susceptibility, electronic specific heat and magnetization of mixed-valent rare earth compounds. *Solid State Communications*, 28(1):119–122, 1978.

[37] G. Mahan, B. Sales, and J. Sharp. Thermoelectric materials: New approaches to an old problem. *Physics Today*, 50:42, 1997.

[38] J. M. Lawrence, P. S. Riseborough, and R. D. Parks. Valence fluctuation phenomena. *Reports on Progress in Physics*, 44(1):1, 2000.

[39] S. K. Dhar, S. K. Malik, and R. Vijayaraghavan. Boron addition to RPd_3 compounds (R = rare earth). *Materials Research Bulletin*, 16(12):1557–1560, 1981.

[40] H. Lusfeld and A. Bringer. Susceptibility, electronic specific heat and magnetization of mixed-valent rare earth compounds. *Solid State Communications*, 28(1):119–122, 1978.

[41] S. R. Boona and D. T. Morelli. Relationship between structure, magnetism, and thermoelectricity in $CePd_3M_x$ alloys. *Journal of Applied Physics*, 112(6):063709–063709, 2012.

[42] R. Lackner, E. Bauer, and P. Rogl. Study of the thermoelectric properties of $CePd_3B_x$. *Physica B Condensed Matter*, 378:835–836, 2006.

[43] R. Lackner, E. Bauer, and P. Rogl. The influence of substitution and doping on the thermoelectric properties of $CePd_3$. *Proceedings of the 26th International Conference on Thermoelectrics*, pages 386–389, 2007.

[44] S.K. Malik, R. Vijayaraghavan, E.B. Boltich, R.S. Craig, W.E. Wallace, and S.K. Dhar. Effect of Si addition on the valence state of Ce in $CePd_3$. *Solid State Communications*, 43(4):243–245, 1982.

[45] D. T. Adroja, B. D. Rainford, and A. G. M. Jansen. Transport and magnetic studies of the Kondo alloys $CePd_3Si_x$. *Journal of Magnetism and Magnetic Materials*, 140:1217–1218, 1995.

[46] M. Houshiar, D. T. Adroja, and B. D. Rainford. Intermediate valence to single ion Kondo behaviour in $CePd_3B_x$ alloys. *Physica B Condensed Matter*, 223:268–270, 1996.

[47] S. K. Malik, S. K. Dhar, and R. Vijayaraghavan. Studies on the valence state of Ce and Eu in some new boron and silicon containing rare earth intermetallic compounds. *Pramana*, 22:329–344, 1984.

[48] S. K. Dhar, S. K. Malik, and R. Vijayaraghavan. Boron-induced valence change of cerium in $CePd_3$. *Physical Review B*, 24(10):6182, 1981.

[49] J. Sereni, G. Nieva, J. P. Kappler, M. J. Besnus, and A. Meyer. Low-temperature thermal properties in the $CePd_3B_x$ system. *Journal of Physics F: Metal Physics*, 16(4):435, 2000.

[50] S. K. Malik, R. Vijayaraghavan, E. B. Boltich, R. S. Craig, W. E. Wallace, and S. K. Dhar. Effect of Si addition on the valence state of Ce in $CePd_3$. *Solid State Communications*, 43(4):243–245, 1982.

[51] S. R. Culverhouse, B. D. Rainford, and D. Paul. Intermediate valence to local moment transition in $CePd_3B_x$ alloys. *Journal of Magnetism and Magnetic Materials*, 108(1):121–122, 1992.

[52] S. K. Malik, S. K. Dhar, and R. Vijayaraghavan. Structural and magnetic investigations of some new boron containing rare earth intermetallic compounds. *Bulletin of Materials Science*, 6(2):263–272, 1984.

[53] B. K. Cho, R. A. Gordon, C. D. W. Jones, F. J. DiSalvo, J. S. Kim, and G. R. Stewart. Specific heat and heavy-fermionic behavior in $Ce_8Pd_{24}M$ (M=Ga, In, Sn, Sb, Pb, and Bi). *Physical Review B*, 57:15191–15196, 1998.

[54] C. D. W. Jones, R. A. Gordon, B. K. Cho, F. J. DiSalvo, J. S. Kim, and G. R. Stewart. Comparisons of electrical, magnetic and low temperature specific heat properties in group 13 and group 14 $Ce_8Pd_{24}M$ compounds (M=B, Al, Ga, In and Si, Ge, Sn, Pb). *Physica B: Condensed Matter*, 262:284–295, 1999.

[55] M. B. Tchoula Tchokonté, P.D.V. Du Plessis, and D. Kaczorowski. Magnetic and electrical properties of $Ce_8Pd_{24}M_x$ alloys (M=Al, Ga, Ge). *Journal of Magnetism and Magnetic Materials, Proceedings of the International Conference on Magnetism (ICM 2003)*, 272-276, Supplement(0):E5–E6, 2004.

[56] C. Mitra, S. K. Dhar, and S. Ramakrishnan. Dense-Kondo antiferromagnetism in $(CePd_3)_8Ge$. *Solid State Communications*, 110(12):701–705, 1999.

[57] S. Singh and S.K. Dhar. Magnetic ordering of the Mn sublattice: Dense Kondo-lattice behavior of Ce in $(RPd_3)_8Mn$ (R=La,Ce). *Physical Review B*, 68(14):144433, 2003.

[58] E. Holland-Moritz, M. Loewenhaupt, W. Schmatz, and D. K. Wohlleben. Spontaneous Relaxation of the Local 4f Magnetization in $CePd_3$. *Physical Review Letters*, 38(17):983–986, 1977.

[59] I. R. Harris, M. Norman, and W. E. Gardner. The electronic state of cerium in some $CeRh_{3-x}Pd_x$ alloys. *Journal of the Less Common Metals*, 29(3):299–309, 1972.

[60] Jun Kondo. Resistance minimum in dilute magnetic alloys. *Progress of Theoretical Physics*, 32(1):37–49, 1964.

[61] B. Bucher, Z. Schlesinger, D. Mandrus, Z. Fisk, J. Sarrao, J. F. DiTusa, C. Oglesby, G. Aeppli, and E. Bucher. Charge dynamics of Ce-based compounds: Connection between the mixed valent and Kondo-insulator states. *Physical Review B*, 53:R2948–R2951, 1996.

[62] L. Kouwenhoven and L. Glazman. Revival of the Kondo effect. *Physics World*, 2001.

[63] M. D. Koterlyn, R. I. Yasnitskii, G. M. Koterlyn, and B. S. Morokhivskii. Thermoelectric power in compounds with an intermediate valence of Ce: phenomenological description. *Journal of Alloys and Compounds*, 348(1):52–56, 2003.

[64] D. Kaczorowski and K. Gofryk. Thermoelectric power of Ce-based intermediate valent systems. *Solid State Communications*, 138(7):337–340, 2006.

[65] T. A. Costi, A. C. Hewson, and V. Zlatic. Transport coefficients of the Anderson model via the numerical renormalization group. *Journal of Physics: Condensed Matter*, 6(13):2519, 1994.

[66] A. Matthiessen and C. Vogt. On the Influence of Temperature on the Electric Conducting-Power of Alloys. *Royal Society of London Philosophical Transactions Series I*, 154:167–200, 1864.

[67] E. Cattaneo. Hall effect of Ce intermetallic compounds. *Zeitschrift für Physik B Condensed Matter*, 64:305–316, 1986.

[68] P. Coleman, P. W. Anderson, and T. V. Ramakrishnan. Theory for the anomalous Hall constant of mixed-valence systems. *Physical Review Letters*, 55:414–417, 1985.

[69] W. P. Beyermann, G. Grüner, Y. Dalichaouch, and M. B. Maple. Relaxation-Time Enhancement in the Heavy-Fermion System $CePd_3$. *Physical Review Letters*, 60:216–219, 1988.

[70] B. C. Webb, A. J. Sievers, and T. Mihalisin. Observation of an Energy and Temperature Dependent Carrier Mass for Mixed Valence $CePd_3$. *Physical Review Letters*, 57:1951–1954, 1986.

[71] H. A. Mook and R. M. Nicklow. Neutron-scattering investigation of the phonons in intermediate-valence $Sm_{0.75}Y_{0.25}S$. *Physical Review B*, 20(4):1656, 1979.

[72] H. A. Mook, D. B. McWhan, and F. Holtzberg. Lattice dynamics of mixed-valent SmS. *Physical Review B*, 25:4321–4323, 1982.

[73] R. Takke, M. Niksch, W. Assmus, B. Luthi, R. Pott, R. Schefzyk, and D.K. Wohlleben. Grüneisen parameter of cerium compounds with unstable 4f shells. *Zeitschrift für Physik B Condensed Matter*, 44:33–39, 1981.

[74] E. Holland-Moritz, D. Wohlleben, and M. Loewenhaupt. Anomalous paramagnetic neutron spectra of some intermediate-valence compounds. *Physical Review B*, 25(12):7482, 1982.

[75] A. Severing, W. Reichardt, E. Holland-Moritz, D. Wohlleben, and W. Assmus. Observation of phonon anomalies in the intermediate-valence compound $CePd_3$. *Physical Review B*, 38:1773–1778, Jul 1988.

[76] F. E. Pinkerton, A. J. Sievers, M. B. Maple, and B. C. Sales. Enhanced far-infrared absorption in $CePd_3$ and $YbCuSi_2$. Experiment. *Physical Review B*, 29(2):609, 1984.

[77] H. M. Rietveld. A profile refinement method for nuclear and magnetic structures. *Journal of Applied Crystallography*, 2(2):65–71, 1969.

[78] A. C. Larson and R. B. Von Dreele. GSAS. *General Structure Analysis System. LANSCE, MS-H805, Los Alamos, New Mexico*, 1994.

[79] B. H. Toby. EXPGUI, a graphical user interface for GSAS. *Journal of Applied Crystallography*, 34(2):210–213, 2001.

[80] H. Schneider and D. Wohlleben. Electrical and thermal conductivity of $CePd_3$, YPd_3, $GdPd_3$ and some dilute alloys of $CePd_3$ with Y and Gd. *Zeitschrift für Physik B Condensed Matter*, 44:193–202, 1981.

[81] J. P. Kappler, G. Krill, M. J. Besnus, M. F. Ravet, N. Hamdaoui, and A. Meyer. Electronic structure of cerium in $Ce_{1-x}Y_xPd_3$ and $Ce_{1-x}M_xAl_2$ (M = Sc, Y). *Journal of Applied Physics*, 53(3):2152–2154, 1982.

[82] D. Jaccard, M. J. Besnus, and J. P. Kappler. Thermoelectric power investigation of the (Ce, Y)Pd_3 system. *Journal of Magnetism and Magnetic Materials*, 63:572–574, January 1987.

[83] Y. Ijiri and F. J. DiSalvo. Thermoelectric properties of $R_xCe_{1-x}Pd_3$ (R=Y, $La_{0.5}Y_{0.5}$, Nd). *Physical Review B*, 55:1283–1287, 1997.

[84] K. J. Proctor, C. D. W. Jones, and F. J. DiSalvo. Modification of the thermoelectric properties of $CePd_3$ by the substitution of neodymium and thorium. *Journal of Physics and Chemistry of Solids*, 60(5):663–671.

[85] P. Scoboria, J. E. Crow, and T. Mihalisin. Resistive behavior and intermediate valence effects in $La_{1-x}Ce_xPd_3$ and $CePd_{3-x}Rh_x$. *Journal of Applied Physics*, 50(B3):1895–1897, 1979.

[86] T. Gambke, B. Elschner, and J. Schaafhausen. Intermediate valence of Ce in $Ce_{1-x}Sc_xPd_3$. *Physics Letters A*, 78:413–415, 1980.

[87] S. N. Mishra. Local magnetism and kondo behaviour of Ce in U-substituted $CePd_3$. *Journal of Physics: Condensed Matter*, 15(30):5333, 2003.

[88] H. Schaeffer and B. Elschner. ESR and hyperfine structure of Mn impurities in the metallic host $CePd_3$. *Solid State Communications*, 53(7):611–614, 1985.

[89] J. P. Kappler, A. Herr, G. Schmerber, A. Derory, J. C. Parlebas, N. Jaouen, F. Wilhelm, and A. Rogalev. Low-temperature properties of the $Ce(Pd_{1-x}Ni_x)_3$ system. *The European Physical Journal B - Condensed Matter and Complex Systems*, 37:163–167, 2004.

[90] P. A. Veenhuizen, Y. Fu-Ming, H. van Nassou, and F. R. de Boer. Magnetic properties and electrical resistivity of $(Ce,Y)Pd_3$ and $Ce(Pd,Pt)_3$. *Journal of Magnetism and Magnetic Materials*, 63:567–571, 1987.

[91] L. Pauling. *The nature of the chemical bond and the structure of molecules and crystals: an introduction to modern structural chemistry*, volume 18. Cornell University Press, 1960.

[92] D. Rambabu, S. K. Dhar, S. K. Malik, and R. Vijayaraghavan. Crystal structure and valence state of cerium in $CePd_{3-x}Pt_x$ alloys. *Physics Letters A*, 87:294–296, January 1982.

[93] G. Oomi, Y. Onuki, and T. Komatsubara. Effect of pressure on the electrical resistivity and lattice constant of $CePd_3$. *Physica B Condensed Matter*, 163:405–408, 1990.

[94] N. V. Chandra Shekar, M. Rajagopalan, J. F. Meng, D. A. Polvani, and J. V. Badding. Electronic structure and thermoelectric power of cerium compounds at high pressure. *Journal of Alloys and Compounds*, 388(2):215–220, 2005.

[95] P. Pedrazzini, D. Jaccard, M. Deppe, C. Geibel, and J. G. Sereni. Multiprobe high-pressure experiments in $CePd_{0.6}Rh_{0.4}$ and $CePd_3$. *Physica B: Condensed Matter*, 404(19):2898–2903, 2009.

[96] E. Beaurepaire, P. Panissod, and J. P. Kappler. Local environment effects on the IV$\rightarrow$$3^+$ transition in $CePd_3B_x$. *Journal of Magnetism and Magnetic Materials*, 47:108–110, 1985.

[97] T. Tchokonté, P. D. V. Du Plessis, A. M. Strydom, and D. Kaczorowski. Magnetic and electrical transport studies of $Ce_8Pd_{24}Al_x$. *Physica B: Condensed Matter*, 378:849–850, 2006.

[98] O. Loebich and C. H. J. Raub. Reactions between some alkali and platinum group metals. *Platinum Met. Rev.*, 25(3):113–120, 1981.

[99] H. Okamoto. Mg-Pd (Magnesium-Palladium). *Journal of Phase Equilibria and Diffusion*, 31:407–408, 2010.

[100] H. Okamoto. Ca-Pd (Calcium-Palladium). *Journal of Phase Equilibria*, 13(1):99–100, 1992.

[101] H. Okamoto. Ce-Pd (Cerium-Palladium). *Journal of Phase Equilibria*, 12:700–701, 1991.

[102] M. J. Besnus, J. P. Kappler, and A. Meyer. Low-temperature heat capacity and resistivity of $CePd_{3+x}$ and MPd_3 (M= Lu, La, Y and Sc). *Journal of Physics F: Metal Physics*, 13(3):597, 2000.

[103] Y. H. Lin, C. R. Wang, C. L. Dong, M. N. Ou, and Y. Y. Chen. Size effects on mixed valence $CePd_3$. *Journal of Physics: Conference Series*, 273(1):012041, 2011.

[104] S. K. Mohanta, S. N. Mishra, K. K. Iyer, and E. V. Sampathkumaran. Microscopic evidence for $4f$ localization with reduced particle size in correlated electron system $CePd_3$. *Physical Review B*, 87(12):125125, 2013.

[105] B. Johansson. Valence state at the surface of rare-earth metals. *Physical Review B*, 19:6615–6619, 1979.

[106] A. Rosengren and B. Johansson. Valence instability of the samarium metal surface. *Physical Review B*, 26:3068–3078, 1982.

[107] Y. Y. Chen, Y. D. Yao, C. R. Wang, W. H. Li, C. L. Chang, T. K. Lee, T. M. Hong, J. C. Ho, and S. F. Pan. Size-induced transition from magnetic ordering to Kondo behavior in (Ce, Al) compounds. *Physical Review Letters*, 84(21):4990–4993, 2000.

[108] S. W. Han, C. H. Booth, E. D. Bauer, P. H. Huang, Y. Y. Chen, and J. M. Lawrence. Lattice Disorder and Size-Induced Kondo Behavior in ceal_2 and cept_{2+x}. *Physical Review Letters*, 97(9):097204, 2006.

[109] K. Mukherjee, K. K. Iyer, and E. V. Sampathkumaran. Contrasting magnetic behavior of fine particles of some Kondo lattices. *Solid State Communications*, 152(7):606–611, 2012.

[110] Y. Y. Chen, P. H. Huang, M. N. Ou, C. R. Wang, Y. D. Yao, T. K. Lee, M. Y. Ho, J. M. Lawrence, and C. H. Booth. Kondo Interactions and Magnetic Correlations in CePt_2 Nanocrystals. *Physical Review Letters*, 98(15):157206, 2007.

[111] D.P . Rojas, L. F. Barquín, J. R. Fernandez, J. I. Espeso, and J. C. G. Sal. Magnetization and specific heat of nanocrystalline rare-earth TbAl_2, TbCu_2 and GdAl_2 alloys. In *Journal of Physics: Conference Series*, volume 200, page 072080. IOP Publishing, 2010.

[112] G. F. Zhou and H. Bakker. Mechanically induced structural and magnetic changes in the GdAl_2 Laves phase. *Physical Review B*, 52(13):9437, 1995.

[113] D. P. Rojas, L. F. Barquín, J. I. Espeso, J. R. Fernández, and J. Chaboy. Reduction of the Yb valence in YbAl_3 nanoparticles. *Physical Review B*, 78(9):094412, 2008.

[114] J. S. Kim, G. R. Stewart, and K. Samwer. Evolution of physical properties with decreasing size in $\mathrm{Ce(Ru_{0.4}Rh_{0.6})_2Si_2}$. *Physical Review B*, 79(16):165119, 2009.

[115] E. V. Sampathkumaran, K. Mukherjee, K. K. Iyer, N. Mohapatra, and S. D. Das. Magnetism of fine particles of Kondo lattices, obtained by high-energy ball-milling. *Journal of Physics: Condensed Matter*, 23(9):094209, 2011.

[116] G. K. Williamson and W. H. Hall. X-ray line broadening from filed aluminium and wolfram. *Acta Metallurgica*, 1(1):22–31, 1953.

[117] C. Suryanarayana. *Mechanical Alloying and Milling*. CRC Press, 2004.

[118] H. A. Razafimandimby and P. Erdös. Intermediate valence theory of CePd_3 and $\mathrm{UNi}_{5-x}\mathrm{Cu}_x$. *Zeitschrift für Physik B Condensed Matter*, 46:193–197, 1982.

[119] H. Okamoto. Ga-Pd (Gallium-Palladium). *Journal of Phase Equilibria and Diffusion*, 29:466–467, 2008.

[120] Q. Lu, P. Sun, D. Huo, T. Mizushima, Y. Isikawa, and J. Sakurai. Magnetic, Thermal and Transport properties of Ce$(Ni_{1-x}Cu_x)_2Al_3$: The Dominant Role of Electronic Change. *Journal of the Physical Society of Japan*, 73:681–686, 2004.

[121] D. T. Adroja, B. D. Rainford, Z. Hossain, E. A. Goremychkin, R. Nagarajan, L. C. Gupta, and C. Godart. Magnetism and crystal field of $Ce_3Au_3Sb_4$. *Physica B: Condensed Matter*, 206:216–218, 1995.

[122] R. Gumeniuk, M. Schmitt, C. Loison, W. Carrillo-Cabrera, U. Burkhardt, G. Auffermann, M. Schmidt, W. Schnelle, C. Geibel, A. Leithe-Jasper, and H. Rosner. Boron induced change of the Eu valence state in $EuPd_3B_x$ $(0 < x < 0.53)$: A theoretical and experimental study. *Physical Review B*, 82:235113, 2010.

[123] D. Young, K. Mastronardi, P. Khalifah, C.-C. Wang, R. J. Cava, and A. P. Ramirez. $Ln_3Au_3Sb_4$: Thermoelectrics with low thermal conductivity. *Applied Physics Letters*, 74(26):3999–4001, 1999.

[124] C. D. W. Jones, K. A. Regan, and F. J. DiSalvo. $Ce_3Cu_xPt_{3-x}Sb_4$: Modifying the properties of a Kondo insulator by substitutional doping. *Physical Review B*, 60(8):5282, 1999.

[125] A. Horyn, Romaka B., and Y. Gorelenko. Crystal structure and electric transport properties of solid solutions of substitution $R_3Cu_3Sb_{4-x}Sn_x$ (R = La, Ce, Pr, Nd, Sm).

[126] C. D. W. Jones, K. A. Regan, and F. J. DiSalvo. Thermoelectric properties of the doped Kondo insulator: $Nd_xCe_{3-x}Pt_3Sb_4$. *Physical Review B*, 58(24):16057, 1998.

[127] H. Okamoto. Ce-Sb (Cerium-Antimony). *Journal of Phase Equilibria*, 22(1):88, 2001.

[128] H. Okamoto. Pt-Sb (Platinum-Antimony). *Journal of Phase Equilibria*, 13(5):580–581, 1992.

[129] P. Sun, T. Ikeno, T. Mizushima, and Y. Isikawa. Simultaneously optimizing the interdependent thermoelectric parameters in Ce$(Ni_{1-x}Cu_x)_2Al_3$. *Physical Review B*, 80(19):193105, 2009.